

THESIS FOR THE DEGREE OF DOCTOR OF PHILOSOPHY

Modeling and Analysis of PMSM with Turn-To-Turn Fault

JOACHIM HÄRSJÖ



Division of Electric Power Engineering
Department of Energy and Environment
CHALMERS UNIVERSITY OF TECHNOLOGY
Göteborg, Sweden 2016

Modeling and analysis of PMSM with turn-to-turn fault
JOACHIM HÄRSJÖ
ISBN: 978-91-7597-516-0

© Joachim Härsjö, 2016.

Doktorsavhandlingar vid Chalmers tekniska högskola
Ny serie nr 4197
ISSN 0346-718X

Department of Energy and Environment
Division of Electric Power Engineering
CHALMERS UNIVERSITY OF TECHNOLOGY
SE-412 96 Göteborg,
Sweden
Telephone + 46 (0)31-772 00 00

Chalmers Bibliotek, Reproservice
Göteborg, Sweden 2016

Abstract

Thanks to its high-torque density and high efficiency, the Permanent Magnet Synchronous Machine (PMSM) is today used in a vast range of applications, spanning from automotive to wind. Since in a PMSM the excitation field is provided by a permanent magnet instead of a coil, this machine does not have a rotor circuit and thereby the risk for electrical failures can be isolated on the stator circuit. These failures are mainly caused by the deterioration of the insulation of the winding due to, for example, thermal stress, electrical stress, mechanical stress, environmental issues or flaws from manufacturing. An insulation failure might lead to a short circuit between different parts of the machine; among these, the most common is the turn-to-turn short circuit. Even though the turn-to-turn fault typically only affects a small portion of the complete phase winding, the induced current in the faulted turns can exceed the rated one. This high current will produce excessive local heat, resulting in a rapid deterioration of the neighboring conductors' insulation and thereby a reduction in the lifetime of the winding or, in the worst case, in permanent damage of the machine and the nearby components. It is therefore important to have good understanding of how a PMSM with turn-to-turn fault behaves in order to develop effective detection methods to limit the damage caused by the fault. This knowledge can be gained through proper modeling of the PMSM with turn-to-turn fault. This thesis focuses on the modeling of the PMSM with a turn-to-turn fault. Analytical models of the machine are derived and validated using Finite Element Method (FEM) models. The analytical model of the faulted PMSM is compared with the non-faulted machine model in order to understand the main characteristics and differences between the two conditions. Different quantities are considered as possible candidates for monitoring and detection of turn-to-turn faults. As first, the focus is on electrical quantities, especially the stator current. It is shown that the presence of a fault condition leads to an unbalance in the machine current and a variation in its harmonic spectra. However, it is shown that this variation is typically very small, posing a detectability issue for actual applications. The machine's electrical power is a more effective signal for monitoring, as the signal incorporates variations in both voltage and current. If parallel windings are used, another possibility is to compare the different branch currents to detect the circulating current caused by the fault. Although it can be an effective detection method, it does require the availability of the branch current measurement in place of (or together with) the measurement of the phase current. An alternative way to identify a turn-to-turn fault is to monitor mechanical quantities. The impact of a turn-to-turn fault on the airgap flux density is limited to only a part of the airgap; as a result, the symmetrical distribution of the airgap flux density is lost in the event of a turn-to-turn fault. Thus, the fault will have an impact on both the electromagnetic tangential and radial force. For the non-faulted machine, the sum of the radial force in the airgap is zero; this does not apply for a faulted machine. The unbalance in radial force causes vibrations; the machine vibrations is the most effective quantity to monitor and used as a fault indication, as it is able to detect fault consisting of only a few short-circuited turns.

Index Terms: Permanent magnet synchronous machine (PMSM) modeling, fault, turn-to-turn fault, inter-turn, electromagnetic forces, fault detection, vibration.

Acknowledgement

This research work has been carried out within Swedish Wind Power Technology Centre (SWPTC). The financial support is gratefully appreciated. The input and feedback from the industry partners ABB and Göteborg Energi is also gratefully appreciated.

I would like to sincerely and wholeheartedly thank my supervisor Professor Massimo Bongiorno and my examiner Professor Ola Carlson for their guidance and support throughout the research work. A special thanks to Massimo for all the patience, support and effort he put into aiding me in completing this thesis.

I would also like to thank my colleagues Christian Du-Bar and Daniel Pehrman for all the fruitful discussions we have had during the years.

A special thanks to Sara Fogelström whose administrative support within SWPTC made it possible to carry out the project without any difficulties.

I am grateful to everyone in my office; Daniel, Nicolás, Pavan, Pinar and Pramod for making the time in the office more enjoyable. I would also like to thank all my colleagues at the division of Electrical Power Engineering and within SWPTC for providing such a fun and pleasant environment to work in.

Finally, but not least, I would like to thank my family, with a special thanks to my beloved wife Johanna, for all their patience, love and support.

Joachim,
Gothenburg, 2016

Preface

The Swedish Wind Power Technology Centre (SWPTC) is a research centre for design of wind turbines. The purpose of the Centre is to support Swedish industry with knowledge of design techniques as well as maintenance in the field of wind power. The research in the Centre is carried out in six theme groups that represent design and operation of wind turbines; Power and Control Systems, Turbine and Wind loads, Mechanical Systems and Structures, Offshore, Maintenance and Reliability as well as Cold Climate.

This project is part of Theme group 1, Power and Control Systems.

SWPTC's work is funded by the Swedish Energy Agency as well as academic and industrial partners. The Region Västra Götaland also contributes to the Centre through collaborating projects.

List of publications

Journal Papers

J. Härsjö, M. Bongiorno “Analytical and FEM Modeling of a PMSM with a turn-to-turn fault” Submitted to IET-Electric Power Applications.

J. Härsjö, M. Bongiorno “Impact of turn-to-turn faults on the electromagnetic forces in a Permanent Magnet Synchronous Machine (PMSM)” Submitted to IET-Electric Power Applications.

Conference Papers

J. Härsjö, M. Bongiorno, O. Carlson, “Dually Fed Permanent Magnet Synchronous Generator Condition Monitoring Using Generator Current”, EWEA 2013: Europe’s Premier Wind Energy Event, February 2013, Vienna, Austria

J. Härsjö, M. Bongiorno, S. Lundberg, O. Carlson, “Permanent Magnet Synchronous Generator Inter-turn Fault Identification Using Stator Current Analysis”, 9th PhD Seminar on Wind Energy in Europe, September 2013, Visby, Sweden

J. Härsjö, M. Bongiorno, ”Modeling and harmonic analysis of a permanent magnet synchronous machine with turn-to-turn fault”, 2015 17th European Conference on Power Electronics and Applications (EPE’15 ECCE-Europe), 8-10 Sept. 2015, Geneva, Switzerland

Content

Abstract	iii
Acknowledgement	v
Preface	vii
List of publications.....	ix
Content.....	xi
Chapter 1 Introduction	1
1.1 Background.....	1
1.2 Purpose of thesis and scientific contributions.....	2
1.3 Thesis outline.....	2
Chapter 2 Overview of faults in wind turbines	5
2.1 Introduction	5
2.2 Mechanical faults.....	7
2.3 Power electronic faults	9
2.4 Generator faults	10
2.5 Summary of available work on the turn-to-turn fault	12
2.6 Chapter summary.....	13
Chapter 3 Analytical Modeling of Permanent Magnet Synchronous Machine	15
3.1 Introduction	15
3.2 General PMSM model	16
3.2.1 State-space representation of linear model.....	18
3.2.2 Inductance calculations using the machine geometry	20
3.2.3 Buildup of back-EMF	25
3.3 PMSM model with a turn-to-turn fault	26
3.3.1 State-space representation of faulted model.....	29
3.4 PMSM model with a turn-to-turn fault in the synchronously rotating reference frame.....	30
3.5 Flexible analytical model.....	34
3.6 PMSM with parallel windings and turn-to-turn fault.....	36
3.7 Chapter summary.....	40
Chapter 4 FEM Modeling of Permanent Magnet Synchronous Machine	41

4.1 FEM model of non-faulted machine	41
4.1.1 Back-EMF of the non-faulted FEM model	44
4.2 FEM model with turn-to-turn fault	47
4.3 Impact of non-linear materials	51
4.4 FEM model with parallel windings	56
4.5 Chapter summery	59
Chapter 5 Model validation and simulation results	61
5.1 Comparison between analytical and FEM Models	61
5.2 Comparison of machine torque between FEM and analytical model	65
5.3 Comparison between faulted and non-faulted analytical models loaded with a pure resistive load	71
5.4 Impact of ideal converter on the electrical quantities of the faulted PMSM ..	75
5.5 Parallel windings and circulating currents	82
5.6 Chapter summary	86
Chapter 6 Electromagnetic forces in a PMSM with turn-to-turn fault	89
6.1 Summary of Maxwell stress tensor	89
6.2 Rotor and stator air-gap flux contribution for smaller modeled machine	93
6.3 Impact of a turn-to-turn fault on the electromagnetic forces	100
6.4 Parallel windings	109
6.5 Chapter summary	112
Chapter 7 Experimental setup of a PMSM with turn-to-turn fault	113
7.1 The experimental setup	113
7.2 Experimental results	116
7.3 Chapter summery	121
Chapter 8 Conclusion and future work	123
8.1 Conclusion	123
8.2 Future work	124
References	127
Appendix A	131
Appendix B	135
Appendix C	137

Chapter 1

Introduction

1.1 Background

The world's energy consumption keeps increasing and due to the climate issues and the cost of fossil fuels, renewable energy sources represent one of the most attractive solutions for meeting the increasing demand. For the last few decades, the wind has been utilized for electrical power production and actual trends clearly show that the number of wind farm installations will keep increasing in the coming years. Countries like U.S. and China (as well as the European Union) have stated that they aim to incorporate more renewables in their system, where up to 25 % of the energy production should be wind based [1]. To be able to reach this goal, both the number of turbines and their size needs to increase; larger turbines achieve better land exploitation, benefit from economies of scale, and have a reduced operation and maintenance costs [2]. However, for wind energy to become a competitive option as an energy source, the associated cost needs to be on par with other conventional energy sources. One method to reduce the overall cost of wind turbine is to use a permanent magnet synchronous machine (PMSM) as a generator in a direct-drive setup, as it is more superior in terms of reliability, energy yield, and have less maintenance problem compared to other setups [3]. Thanks to the high torque-density of this machine type, the overall nacelle weight is reduced which results in cost savings on the tower and the foundations. However, even though this topology provides higher energy yield and less maintenance problems, the operational and maintenance costs for wind turbines is still comparably high because of the hard-to-access structures and that the turbines are often placed at remote locations [1]. For onshore wind turbines, the operational and maintenance cost could go up to 30% of the total levelized life-cycle cost [4].

Since the size of the turbines are increasing, the economic value of each individual component is significant, and the cost associated with the replacement of one of the major components can be up to 20% of the price of a new turbine [5]. It is therefore important to implement effective fault detection methods that are able to early identify the occurrence of a fault, in order to minimize any downtime and the damage to the component and its' nearby components. If the fault is detected at an early stage, there is a possibility that the component can be repaired instead of being replaced. For wind turbine topologies based on PMSM as generator, an electrical failure can only occur in the stator circuit. The most common type of fault in the stator circuit of a PMSM is the internal turn-to-turn short-circuit [6]. Nevertheless, effective detection methods for this kind of faults are not available in the market. One reason for this is that if the fault only consists of a few short-circuited turns, it may initially not cause any noticeable impact on the machine's operation. However, if the fault condition

persists, the additional heat generated by the fault can cause an avalanche like failure of the entire stator circuit or even cause a fire.

In order to be able to develop effective detection methods for turn-to-turn faults, knowledge of the behavior of the faulted machine is needed in order to identify the best signals, either electrical or mechanical, to be monitored.

1.2 Purpose of thesis and scientific contributions

The main objective of the work presented in this thesis is to develop a generic analytical model of the permanent magnet synchronous machine with an internal turn-to-turn short-circuit fault, able to accurately model the behavior of the electrical quantities of the machine during this specific fault condition. In this thesis, the models are used to generate knowledge of the faulted machine's behavior, with the intention of using the generated knowledge for developing effective fault detection methods for the turn-to-turn fault for PMSMs.

To the best knowledge of the author, the main contributions of the work presented in this thesis can be summarized as follows:

- Derivation of a generalized analytical model of a permanent magnet machine with turn-to-turn fault in both the stationary and the rotating reference frame, which can be used in a wide range of applications.
- Verification that the less computational intense analytical models present comparable results for the electrical quantities of that of FEM models, both during transient and steady-state operation.
- Analysis of the impact of a turn-to-turn fault on the air-gap flux density and the resulting electromagnetic forces. The obtained results of the electromagnetic forces are verified in an experimental setup.

1.3 Thesis outline

This thesis is constituted by eight chapters, a list of references and three appendices. In Chapter 2, a brief review of typical faults occurring in the different wind turbine sub-systems, including the mechanical, structural and the electrical sub-system is presented. Chapter 3 presents the analytical modeling of the PMSM, where a generic non-faulted PMSM is first presented for reference purposes. From this generic model, the model of the faulted machine is derived both in the stationary and in the rotating reference frame. A model which is able to switch from a non-faulted state into a faulted state is also presented, as well as a model adaptation in order to be able to model machines with parallel windings. Chapter 4 presents finite element method (FEM) models of two different PMSM designs; one smaller machine with concentrated windings and a larger machine with distributed parallel winding. Both models are modified to incorporate the turn-to-turn fault. The FEM models are used to verify the analytical derivation and to investigate the impact of non-linear

materials. Chapter 5 presents the simulation results. First, the analytical model is verified against the FEM model, both for the non-faulted and the faulted machine. Thus, the impact of different operational condition is investigated. Chapter 6 presents how the FEM models are used to study the air-gap flux density of the presented models, how this is affected by the turn-to-turn fault and thereby how the fault impacts the electromagnetic forces of the machine. Chapter 7 presents the experimental setup and the obtained measurement results are used to verify the simulation analysis. Finally, Chapter 8 contains the main conclusions of the work together with some suggestions for future work.

Chapter 2

Overview of faults in wind turbines

This chapter presents a brief overview of the most common component failures that occur in wind turbine systems. A brief explanation of the cause of the failure is also presented.

2.1 Introduction

The amount of wind power installed in the world has steadily increased since the 1980s, where both numbers of turbines and their power rating has increased. Figure 2.1 presents the globally installed wind power up until the year 2015 [8]. The figure clearly shows that the installed wind power capacity has grown exponentially over the past decade.

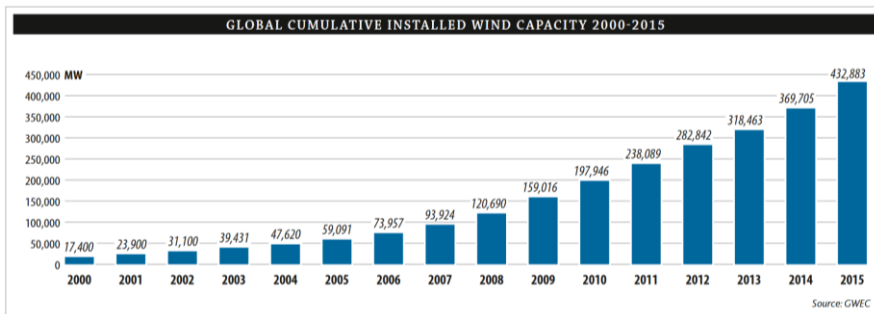


Figure 2.1 The global cumulative installed wind capacity from 1996 to 2015 [8].

The first commercial wind turbines appeared in the 1980's and the turbines back then were small fixed-speed turbines with a power rating of less than 100 kW. Over the years the power rating of the turbines has increased, and already during the mid 1990's the typical turbine rating was between 750 kW and 1000 kW [9]. The modern turbines have a power rating up to 8 MW [10] and utilize variable-speed drive; furthermore, they can provide grid support features, thanks to the presence of power-electronics based controllers.

A critical aspect for any energy production units is the cost of energy. In the case of wind energy, the cost is mainly related to the initial investment and the operational and maintenance cost. Efficient maintenance procedures should provide more hours of operation, which in turn lead to a reduction of the total cost of energy. Through the utilization of effective fault detection systems, maintenance and downtime costs can be reduced. Some of the benefits of an effective fault detection systems are:

- Minimize repairation costs and the loss of power production.

- Reduced the maintenance cost as it can be organized in need-based rather than time-based maintenance strategy.
- Improved capacity factor by better scheduling of maintenance during less windy seasons.

An additional possible benefit of a proper fault detection system is that it may generate additional operational data that can be used in other applications, such as during the development of the next generation of turbines.

According to [11], the most common wind turbine sub-assemblies to fail for variable-speed turbine types (in descending order) are:

- Electrical system
- Rotor (i.e. blades and hub)
- Converter (i.e. electrical control, power electronics)
- Generator
- Hydraulics
- Gearbox

However, this does not completely agree with the data presented in [12], which has studied a different population of wind turbines. Figure 2.2 presents the data presented in [12] which also includes the average downtime caused by each component failure.

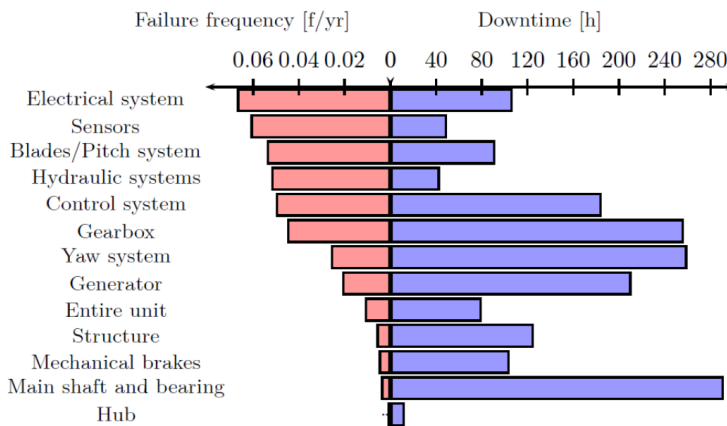


Figure 2.2 The average failure rate and downtime per sub-assembly and year in wind turbines, presented in [12].

As can be seen from Figure 2.2, the difference in the failure rates is rather small among the sub-assemblies which tends to fail the most. However, the downtime caused by the failures of the different sub-assemblies varies more than the failure

rates. The most critical sub-assemblies from a reliability perspective are therefore the ones that have both a high failure rate and a long downtime, such as the gearbox.

In [11], it is also stated that larger wind turbines have a lower reliability as compared to smaller turbines and the failure rate of generators for turbines that use a direct-drive topology is up to double of the geared topologies. However, the generator failure rate can be reduced through replacing the electrical excitation in the rotor winding with permanent magnet. In addition, the failure rate of the power electronics is higher for wind applications than for other industries [11]. Some of these failures and other wind turbine related faults are described more in detail in this chapter, together with a brief explanation of the possible causes of the faults.

2.2 Mechanical faults

Most of the components in a wind turbine can either be said to belong to the mechanical system or to the turbine structure. Examples of sub-assemblies belonging to the mechanical system are the drive-train and the blades, where the foundation and the tower are examples of sub-assemblies belonging to the turbine structure. The cause of a failure in a mechanical component cannot typically be addressed to a single reason, but rather to the combinations of several factors. Possible reasons for failure are fatigue, corrosion, manufacturing errors, assembly errors, and the ambient condition in which the component operates. The ambient condition includes humidity, temperature, and dust. It also includes the weather condition, both for normal and extreme events such as storms and lightning strikes.

If there is any damage on the turbine blades it needs to be detected, since operating with damaged/broken blades can cause secondary damages to the entire wind turbine [1]. The blades also represent a considerable amount of the initial cost of a turbine and they typically are costly and time consuming to repair. This motivates the need for an efficient condition monitoring system for the blades. Even though the blades are constructed in layer structure where the layers consist of different materials, the failure tendency of all the materials can be considered equal. As a result, the blades do not have a typical weak spot inherent in their architecture caused by the used materials. The blade failures that occur in wind turbines are mainly caused by creep- and corrosion fatigue, and the fault impact on the blades behavior depends on the faults location on the blade. In addition, detecting a blade fault is non-trivial as other phenomena can cause similar characteristic behavior as the fault. Ice on the rotor or dead insects both alter the rotor blade surface in a similar manner as cracks and delamination caused by a fault [1]; all of these phenomena have an impact on the blade's aerodynamic efficiency. Figure 2.3a presents a summary of some of the faults that can occur in a rotor blade and Figure 2.3b presents a photo of a blade with cracks in the gelcoat and some splitting along its fibers [13].

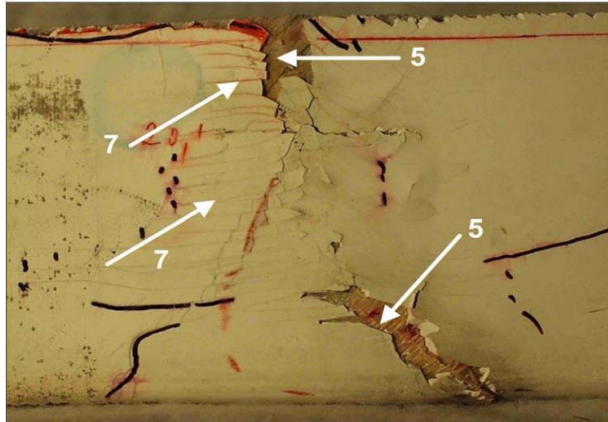
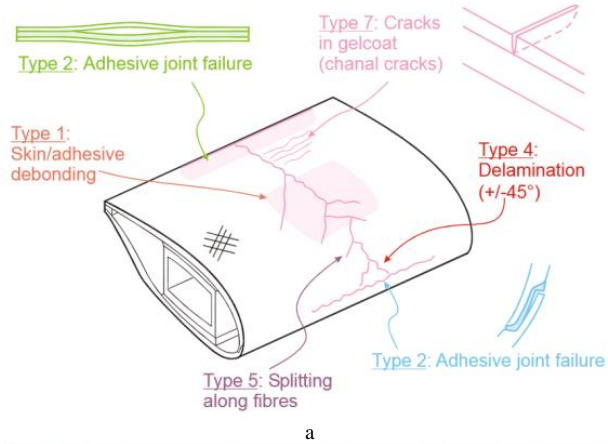


Figure 2.3 Examples of rotor damages, presented in [13].

Even though detecting a blade fault is non-trivial, there are several methods suggested for detecting this kind of events. Different methods use different quantities for detecting a blade fault, such as acoustic emissions, thermal imaging, ultra-sonic methods, and modal-analysis. A more detailed description of the different methods can be found in [14], which also discusses the applicability of similar methods to investigate failures in the structure of the tower.

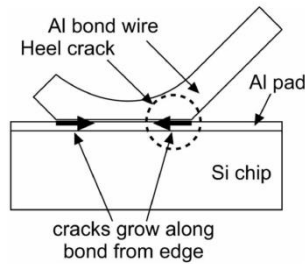
In close connection to the blades is the pitch-system, which in the event of a failure can put the turbine in a critical situation. A faulty pitch-system can cause severe unbalanced loading on the rotor, causing secondary damages to the entire wind turbine. The worst possible scenario is if the pitch-system fails in presence of wind speeds that greater than the cut-out level. In this case, it may result in the turbine being unable to shut down as the pitch-system cannot be used to turn the rotor blades in order to achieve aerodynamic braking [1].

Within the drive-train, gearbox failure for the indirect-drive is one of the most common components to fail [15]. Gear tooth wear is one of the reasons that causes failure in wind turbine failures, but the most common gearbox failure is related to the bearing. A multistage gearbox used in wind applications typically includes several bearings; however, it is typically only a few specific bearings which tends to fail, such as the main bearing [1]. There are methods developed to detect bearing faults based on the use of vibration sensors. To increase the reliability of the fault detection, acoustic measurements can also be included [1]. The issue of gearbox failures can be avoided by choosing a direct-drive topology, but at the expense of a larger and more complex generator. However, statistics show that this does not completely solve the issue, since turbines using direct-drive topology approximately have equal failure as compared with indirect-drive topology. This is because the failure rate of the generator and the power electronics is higher for direct-drive turbines [15]. However, the total downtime may still be reduced, since the downtime caused by generator and power electronic failures are lower compared to gearbox failures, see Figure 2.2.

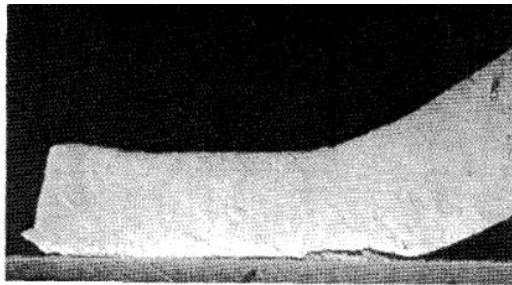
2.3 Power electronic faults

The power electronic components represent a comparably small part of the initial wind turbine cost, but it accounts for a considerable amount of the failures [1]. However, since the mean time to repair of a power electronic component is low, the contribution to the total down time is comparatively low despite the higher fault occurrence. Semiconductor failure can be caused by several factors, such as electrical overstress, electrostatic discharge, contamination and various sorts of mechanical stress. The mechanical failures are typically related to thermal cycling caused by varying electrical loading. Because the different materials used in the packaging of the components have different thermal expansion coefficients, the thermal cycling results in mechanical wear and fatigue [1]. Figure 2.4a presents a principle sketch of bond-wire liftoff caused by cracks originating from thermal cycling [16]. Figure 2.4b shows a photo of bond-wire crack [17].

To model the breakdown mechanism of a power electronic component requires detailed multi-disciplinary sub-models such as electro-thermal and thermo-mechanical models [16]. A review and comparison between different modeling methods for various power electronics faults is presented in [16], which also discusses the different possibilities of condition monitoring to assess the remaining lifetime of the units. The conclusion presented in [16] is that the research area is in its infant stage and more research is needed before effective condition monitoring system can be implemented in converter systems (regardless of application).



a



b

Figure 2.4 Bond-wire cracks due to thermal cycling. Figure a can be found in [16] and figure b in [17].

A fault in a power semiconductor for a two-level converter results in either an open-circuit fault, a short-circuit fault or an intermittent gate-misfire depending on which part of the component has failed [18]. A review of different methods used to detect a failure within a power semiconductor, where each method only focuses on a specific type of fault is presented in [18]. An open-circuit fault will not cause any direct damage but it causes the controller instability which in turn can cause secondary damage. A short-circuit fault will most likely cause too high currents, making it more time critical to detect compared to the open-circuit fault. As a result, the short-circuit fault detection is typically hardware implemented and designed as a protection system rather than a condition monitoring or fault detection system. The intermittent gate-misfire fault will either affect the system as an open-circuit fault in the case of gate-fire inaction or it will create a short-circuit fault in case of an unwanted gate-fire or due to the inability of gate-turnoff.

2.4 Generator faults

The generator, like the mechanical system, can be divided into smaller sub-assemblies: the stator circuit, rotor circuit, the mechanical drive-train, and the machine frame. The machine frame is the static construction that holds the physical machine together, and the part of the machine frame that is referred to as the active structure is the part that carries magnetic flux. The mechanical drive-train consists of the moving parts of the generator, where the most likely component to fail is the bearing [1]. For a PMSM, the rotor circuit only consists of parasitic components,

which ideally should not carry any current. However, due to inhomogeneous air-gap reluctance there will be eddy currents in the rotor, both in the rotor laminate and in the magnets (if the machine is rotating). If excessive, the eddy currents can cause magnet demagnetization. A failure in a magnet mounting results in the loss of a magnet, which causes the machine to become unbalanced. The unbalance in the machine will cause the machine currents to become unbalanced and introduce a ripple in the machine torque.

Failure in the stator circuit is mainly caused by winding insulation failure, where the insulation of the winding can deteriorate due to several reasons. Examples of phenomena that can cause insulation deterioration are thermal, electrical, mechanical, or environmental issues [6]. Thermal stress accelerates the ageing process of the insulation, i.e. it decreases the operational lifetime of the insulation. A “rule of thumb” stated in [6] is that a 10° C increase in temperature reduces the insulation lifetime up to 50 %. However, simple ageing will not lead to insulation failure, it will only make the insulation more susceptible to other types of stresses that will lead to the actual failure. An example of an electrical stress that can cause insulation failure is a too steep voltage transient, which should be considered for machine connected to converters where high voltage transients are applied from the converter switching [19].

Mechanical stress on the winding is caused by the physical movement of the windings, and if two or more windings touch, the friction between them causes the insulation to fail. The movement can originate either from the resulting forces created on a current-carrying conductor within a magnetic field or from external sources, such as vibrations due to rotor misalignment or damaged bearing. Figure 2.5 shows a picture of a stator that has lost some of the slot wedges that are used to restrict the movement of the winding [20]. Without these wedges, the risk of physical movement of windings increases and therefore also the risk of friction-caused faults between neighboring conductors.



Figure 2.5 A picture of a stator missing some slot wedges, presented in [20].

The working environment and the possible ambient issues for an electrical machine depends both on the location and on its application. Example of possible environment issues could be contamination, dust, humidity, aggressive chemicals or salt. For coastal and offshore wind turbines, humidity and salt are typical issues. As for of thermal stress, the environmental stress will not cause a direct failure, but will rather cause indirect failures due to insulation deterioration.

An insulation failure might lead to a short-circuit between the various parts of the machine. The short-circuit may be phase-to-ground, phase-to-phase, coil-to-coil or turn-to-turn, where the phase-to-ground short-circuit can permanently damage the mechanical structure of the stator. If so, the stator needs to be replaced while the rotor can be reused. According to [6], the majority of the insulation faults originate from a small turn-to-turn fault, typically only consisting of a few short-circuited turns. For the synchronous machine or the PMSM, this type of fault leads to an induced current in the loop created by the short-circuited turns (as long as the machine is rotating). Even though the turn-to-turn fault typically only affects a small portion of the complete phase winding, the induced fault current can be greater than the rated one. This high current produces excessive local heat at the fault, causing a rapid reduction of the lifetime of the insulation in the neighboring conductors. As a result, a turn-to-turn fault can initiate an avalanche like failure in the winding, where more and more turns become short-circuited. Once a turn-to-turn fault has occurred, it is typically only a short time period before the entire winding insulation has failed. It could be in the time range of minutes from initial fault to the failure of the entire winding [1]. Even though most winding faults originate from a turn-to-turn fault, there is no commercial proven method for the detection of a turn-to-turn fault for PMSMs. This is the driving force behind this thesis.

2.5 Summary of available work on the turn-to-turn fault

There are works available in the literature that describes how to analytically model a PMSM with a turn-to-turn fault, as the ones reported in [21] and [22]. However, most of the available works present how to model the faulty machine for specific applications, which in turn compromise the generality of the model. For example, [23] presents models for different winding configurations, while [24] and [25] presents how the slots, pole and position of the short-circuited turns affect the machine; a model of the PMSM with parallel stator winding is presented in [26]. In [27], saturation of the magnetic material is considered, where a look-up table derived from the datasheet of the motor is suggested to be used to include saturation effects. A general conclusion that can be drawn from these papers is that the machine's design impacts the behaviour of the machine during faulted conditions. The aim in this thesis is to derive a model that is as generic as possible, allowing to apply the model to any PMSM design; the design of the PMSM will only influence the model's parameter values.

Other papers focus on the derivation of models for the PMSM with turn-to-turn faults aiming at establishing fault detection methods, as in this thesis. However, in this

works only the electrical quantities of the machine are considered and are represented under steady-state operation. For example, [28] proposes a method based on monitoring the reactive power, [29] suggests that the harmonic content should be monitored and [30] suggests to monitor the zero-sequence current as a detection method. For some of these papers, the portion of the phase winding that is short-circuited is fairly high (more than 50%), demonstrating that the suggested signals to monitor for fault detection purposes are ineffective when only a few turns (low portion of the phase winding) are short-circuited. It is of importance to highlight that none of the methods proposed in the currently available literature appear as the ultimate solution to the problem of turn-to-turn fault detection. Furthermore, to the best knowledge of the author, the presented papers focus on the electrical quantities only, neglecting the impact of the fault condition on the mechanical system of the machine. The aim of this thesis is to investigate if it is possible to achieve an effective detection method, based on monitoring of electrical quantities, that enables the identification of the presence of a turn-to-turn fault also when only a few number of turns are short circuited. Furthermore, this thesis investigates the impact of the fault on the machine's vibrations, aiming at understanding if the monitoring of the mechanical vibrations of the machine is a more effective way to detect the occurrence of a turn-to-turn fault as compared to the electrical quantities.

2.6 Chapter summary

This chapter presented a brief overview of some of the most common wind turbine failures. For some of the faults listed in this chapter, detection methods are available in the market, while other types of faults require more research in order to better understand the root cause of the failure. The most common generator failure of electrical nature is the turn-to-turn fault, which can develop into other types of winding failures. Since the time frame between the initial fault and the complete winding failure can be in the range of minutes, an effective fault detection method for this type of fault is needed to minimize and prevent further damage.

The following chapter presents how to analytically model a generic PMSM with a turn-to-turn fault, both in the stationary and rotating reference frame. The model in the stationary reference frame is extended to be able to represent a PMSM that utilizes parallel winding designs.

Chapter 3

Analytical Modeling of Permanent Magnet Synchronous Machine

This chapter presents the derivation of the analytical model of the PMSM, both under normal conditions and in the presence of a turn-to-turn fault. The model of the faulted machine is based on the non-faulted model. The model of the faulted machine is derived in the stationary as well as in the rotating reference frame; furthermore, the model has been extended to represent machines with parallel windings. A flexible model is also presented, which is able to simulate the transition from non-faulted to faulted conditions.

3.1 Introduction

The use of PMSM is increasing thanks to the availability of strong magnets that enable machines with high-torque density in relation to the machine's volume. However, for this type of machine, turn-to-turn faults pose a great issue, due to the fact that the rotor excitation cannot be removed remotely as in the case of the electrically-excited synchronous machine. For this kind of machines, the only method to avoid inducing fault currents in the short-circuited turns is to completely stop the machine from rotating in order to prevent a complete breakdown. It is therefore important to establish fault detection methods, in order to limit the damage caused by the fault. For wind turbine applications, the generator is a vital and expensive component. It is therefore important that there are effective fault detection systems connected to the generator, which must be robust and accurate in order to avoid production losses due to wrongfully triggered alarms. The turn-to-turn fault is difficult to detect, as the current induced in the short-circuited turns cannot typically be measured. However, as the turn-to-turn fault is one of the most common stator faults, there is a need for a detection method that is able to detect turn-to-turn faults using only accessible information. In order to derive effective detection methods, proper modeling of the machine under fault conditions is necessary, in order to understand the behavior of the machine and thereby identify the most suitable quantities to monitor.

This chapter presents an analytical three-phase model of the PMSM with and without turn-to-turn fault implemented in the stationary reference frame, similar to the models described in [21] and [22]. The presented analytical model is then transformed into the synchronously-rotating reference frame using an adapted transformation matrix. A flexible model, which is able to simulate the transition from the non-faulted to the faulted state during a simulation, is then presented. Since large machines (such as wind power generators) are typically equipped with parallel windings, the presented

model of the faulted machine is extended in order to be able to model machines with parallel windings.

3.2 General PMSM model

This section presents a basic and general model of a PMSM; similar models of PMSMs can be found in the literature [31]. The general model is presented for reference purposes and the model of the faulted machine is derived from it. For the clarity of the text, in this thesis a “*linear machine*” refers to a machine where the materials are assumed to have linear properties.

The phase voltage of a wye-connected electrical machine can electrically be modeled as

$$u_x = R_s i_x + \frac{d\Psi_x(i, \theta_r)}{dt} \quad (3.1)$$

where u_x is the voltage of phase x , R_s is the stator winding resistance, i_x is the current in phase x and Ψ_x is the flux linkage of phase x , which for a permanent magnet machine depends on the rotor position θ_r and the phase currents. Since the rotor position and the currents are time dependent, the time derivative of the flux linkage for a three phase machine can be described by a sum of partial derivate as

$$\frac{d\Psi_a(i, \theta_r)}{dt} = \frac{d\Psi_a(i, \theta_r)}{di_a} \frac{di_a}{dt} + \frac{d\Psi_a(i, \theta_r)}{di_b} \frac{di_b}{dt} + \frac{d\Psi_a(i, \theta_r)}{di_c} \frac{di_c}{dt} + \frac{d\Psi_a(i, \theta_r)}{d\theta_r} \frac{d\theta_r}{dt} \quad (3.2)$$

where a, b and c indicate the three phases. For linear machines that do not include saturation, the superposition principle can be adopted, meaning that there are no cross-coupling saturation effects between the three currents and rotor position. This dictates that a change in current will result in a linear response in the flux linkage regardless of operational point, i.e. the different terms in (3.2) can be represented through constant values. For linear models, the term $\frac{d\Psi_a(i, \theta_r)}{di_a}$ is typically referred to as the self-inductance (L), while the terms $\frac{d\Psi_a(i, \theta_r)}{di_b}$ and $\frac{d\Psi_a(i, \theta_r)}{di_c}$ are denoted as mutual inductance (M_{ab} and M_{ac} , respectively). The term $\frac{d\Psi_a(i, \theta_r)}{d\theta_r}$ represents the change in the amount of the permanent magnet flux that is linking phase a due to the rotor position (or alignment). As the machine modeled in this thesis is a synchronous machine, the permanent magnet flux linkage of phase a (inherent from the machine design) has a wave-like shape that can therefore be described using a Fourier series as

$$\Psi_a(\theta_r) = \sum_{k=1}^{\infty} \Psi_k \cos(k\theta_r + \varepsilon_k) \quad (3.3)$$

where Ψ_k is the amplitude of the harmonic and ε_k is the phase shift of that harmonic. The harmonics originate from phenomena such as slot harmonics and magnet skewing, and in general appear due to the non-ideal geometry of the machine;

therefore, these harmonics are always present in the permanent magnet flux linkage, regardless of the material properties of the machine. In addition, the harmonic content may vary during non-linear operation, such as during magnetic saturation. Evaluating the position derivative of the permanent magnet flux for a linear model results in

$$\frac{d\Psi_a(i, \theta_r)}{d\theta_r} \frac{d\theta_r}{dt} = \omega_r \sum_{k=1}^{\infty} -k\Psi_k \sin(k\theta_r + \varepsilon_k) = \omega_r e_a \quad (3.4)$$

where ω_r is the time derivative of the electrical position of the rotor. As the machine modeled in this thesis is a synchronous machine, the time derivative of the electrical position of the rotor equates to the machine's electrical speed. If the machine is approximated to have a perfectly shaped back-EMF waveform, characterized by a single frequency, the modeling of the permanent magnet flux linkage can be simplified into

$$\Psi_{pm}(\theta_r) = \Psi_{pm} \cos(\theta_r) \quad (3.5)$$

However, if a higher accuracy of the back-EMF is needed, the geometry of the specific machine under investigation needs to be known. There are analytical methods available for estimating the back-EMF from the geometry, as for example presented in [32]; alternatively, finite element software can be used for this purpose. The machine geometry is also needed to calculate the values of the self and mutual inductances; as for the back-EMF, the inductance values can be derived analytically (as described in [32] and [33]), or using a finite element software.

A circuit representation of a healthy phase of the linear machine is presented in Figure 3.1, where u is the phase voltage, R is resistance, L is the self-inductance and $\omega_r e$ is the back-EMF.

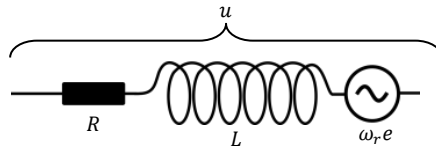


Figure 3.1 Circuit representation of one of the phases of a linear PMSM.

From the symmetries in the geometry of a radial machine it can be assumed that the coupling between two phases is bidirectional, i.e.

$$M_{ab} = M_{ba} \quad (3.6)$$

and if the stator phases are identically constructed (except for being shifted in space), all phases have identical inductive coupling and self-inductances:

$$M_{ab} = M_{ac} = M_{bc} = M, L_a = L_b = L_c = L \quad (3.7)$$

Utilizing (3.4), (3.6) and (3.7) the flux derivative of phase a can be evaluated as

$$\frac{d\Psi_a(i, \theta_r)}{dt} = L \frac{di_a}{dt} + M \left(\frac{di_b}{dt} + \frac{di_c}{dt} \right) + \omega_r e_a \quad (3.8)$$

The same approach can be used to evaluate the flux derivatives for the other two phases, with the only difference that phase b and phase c will be $-\frac{2\pi}{3}$ and $\frac{2\pi}{3}$ electrical radians shifted with respect to phase a , respectively. With all phases evaluated, the complete three-phase machine can be represented in a matrix form as

$$\begin{bmatrix} u_a \\ u_b \\ u_c \end{bmatrix} = \begin{bmatrix} R_s & 0 & 0 \\ 0 & R_s & 0 \\ 0 & 0 & R_s \end{bmatrix} \begin{bmatrix} i_a \\ i_b \\ i_c \end{bmatrix} + \begin{bmatrix} L & M & M \\ M & L & M \\ M & M & L \end{bmatrix} \frac{d}{dt} \begin{bmatrix} i_a \\ i_b \\ i_c \end{bmatrix} + \omega_r \begin{bmatrix} e_a \\ e_b \\ e_c \end{bmatrix} \quad (3.9)$$

Denoting with bold quantities either a vector or a matrix, (3.9) can be written in a compact form as

$$\mathbf{u} = \mathbf{R}\mathbf{i} + \mathbf{L} \frac{d\mathbf{i}}{dt} + \mathbf{e} \quad (3.10)$$

where \mathbf{u} represent the voltage vector, \mathbf{R} represents the resistances matrix, \mathbf{L} represents the inductance matrix and \mathbf{e} represents the back-EMF vector. Using the matrix representation the machine model can be rearranged in the state-space form in order to simplify the implementation of the model in a simulation environment.

3.2.1 State-space representation of linear model

From the matrix representation, the machine model can be described using a state-space model representation as:

$$\begin{aligned} \frac{d\mathbf{x}}{dt} &= \mathbf{A}\mathbf{x} + \mathbf{B}\mathbf{u} \\ \mathbf{y} &= \mathbf{C}\mathbf{x} + \mathbf{D}\mathbf{u} \end{aligned} \quad (3.11)$$

where \mathbf{x} is the state variables, \mathbf{u} is the system inputs and \mathbf{y} is the system output. Selecting the stator currents as state variables and system outputs, then (3.9) converted into state-space form becomes

$$\frac{d\mathbf{i}}{dt} = \mathbf{L}^{-1}(\mathbf{U} - \mathbf{R}\mathbf{i} + \mathbf{e}) \quad (3.12)$$

which translates into

$$\begin{aligned} \mathbf{A} &= \mathbf{L}^{-1}(-\mathbf{R}) \\ \mathbf{B} &= \mathbf{L}^{-1}\mathbf{U}_{mat} \\ \mathbf{C} &= \mathbf{I} \\ \mathbf{D} &= \mathbf{0} \end{aligned} \quad (3.13)$$

where \mathbf{U}_{mat} is the resulting input matrix correlating the input voltages and the back-EMF. By selecting the applied voltages and the electrical speed of the machine as inputs to the state-space model

$$\mathbf{u} = \begin{bmatrix} u_a \\ u_b \\ u_c \\ \omega_r \end{bmatrix} \quad (3.14)$$

then \mathbf{U}_{mat} for a non-faulted PMSM is

$$\mathbf{U}_{mat} = \begin{bmatrix} 1 & 0 & 0 & e_a \\ 0 & 1 & 0 & e_b \\ 0 & 0 & 1 & e_c \end{bmatrix} \quad (3.15)$$

Evaluating the \mathbf{A} and \mathbf{B} matrixes gives

$$\mathbf{A} = \begin{bmatrix} -\frac{(L+M)R_s}{L^2+LM-2M^2} & \frac{MR_s}{L^2+LM-2M^2} & \frac{MR_s}{L^2+LM-2M^2} \\ \frac{MR_s}{L^2+LM-2M^2} & -\frac{(L+M)R_s}{L^2+LM-2M^2} & \frac{MR_s}{L^2+LM-2M^2} \\ \frac{MR_s}{L^2+LM-2M^2} & \frac{MR_s}{L^2+LM-2M^2} & -\frac{(L+M)R_s}{L^2+LM-2M^2} \end{bmatrix} \quad (3.16)$$

$$\mathbf{B} = \begin{bmatrix} \frac{L+M}{L^2+LM-2M^2} & -\frac{M}{L^2+LM-2M^2} & -\frac{M}{L^2+LM-2M^2} & \frac{e_a}{L-M} \\ -\frac{M}{L^2+LM-2M^2} & \frac{L+M}{L^2+LM-2M^2} & -\frac{M}{L^2+LM-2M^2} & \frac{e_b}{L-M} \\ -\frac{M}{L^2+LM-2M^2} & -\frac{M}{L^2+LM-2M^2} & \frac{L+M}{L^2+LM-2M^2} & \frac{e_c}{L-M} \end{bmatrix} \quad (3.17)$$

All elements in matrixes \mathbf{A} and \mathbf{B} are constants constituted by the machine parameters, except for the fourth column in the \mathbf{B} matrix, which also includes the back-EMF. This introduces non-linearities in the state-space representation. However, if all machine parameters are known, the state-space representation can be used in simulation software if the \mathbf{B} matrix of the model is updated at every iteration, i.e. make a linear approximation of the state-space model at every simulation time step.

To be able to simulate the presented state-space model, the values of all parameters constituting \mathbf{A} and \mathbf{B} need to be known. The resistive part of the machine directly depends on the amount of copper used, while the values of the inductances depend on the machine geometry and winding configuration. The following subsection describes how the geometry of the machine impacts the inductance values and how these can be calculated for a given geometry.

3.2.2 Inductance calculations using the machine geometry

For electrical machines, the inductance can be seen as an index of the stator currents' ability to affect the airgap flux. Simplified, the machine inductance can be said to depend on the number of winding turns and the reluctance path of the magnetic flux, where the reluctance of a flux path is defined as

$$\mathcal{R} = \frac{l}{\mu_0 \mu_r A} \quad (3.18)$$

where l is the length of the flux path, μ_0 is the permeability of vacuum, μ_r is the relative permeability of the material and A is the cross-section area of the path. With the use of (3.18), the reluctance of the various parts of the machine can be calculated for a given geometry and material properties. By dividing the machine geometry into smaller segments, the machine can be modeled using a reluctance grid as illustrated in Figure 3.2. In the presented example, the different reluctance segments the machine are divided into are the stator tooth \mathcal{R}_t , the part of the stator back in between two teeth \mathcal{R}_s , the airgap and magnet between tooth and rotor \mathcal{R}_g , the leakage airgap path between two neighboring teeth \mathcal{R}_σ , and a part of the rotor core between two teeth \mathcal{R}_r . Each of these segments has a different reluctance value. The machine windings are represented at each tooth as magnetomotive force (*MMF*) sources. The upper loops (in this example indexed 1 to n) represent the stator circuit, while the lower loops (in this example indexed $n + 1$ to $2n$) mainly represent the rotor and airgap circuits. Note the absence of *MMF* sources in the lower (rotor) loops, as it is only the current carrying coils which are of interest when calculating the values of the inductances.

The reluctance of each segment can be estimated using various methods, depending on the needed accuracy. A crude but simple method is to assume that each segment has a rectangular shape, neglecting the realistic shape of the tooth shoe, slot leakage and the slot opening effects on the airgap. In [33], a more accurate method of estimating the reluctance of each segment is presented. In this thesis, both the crude and more accurate method are used and compared with results acquired from a FEM model.

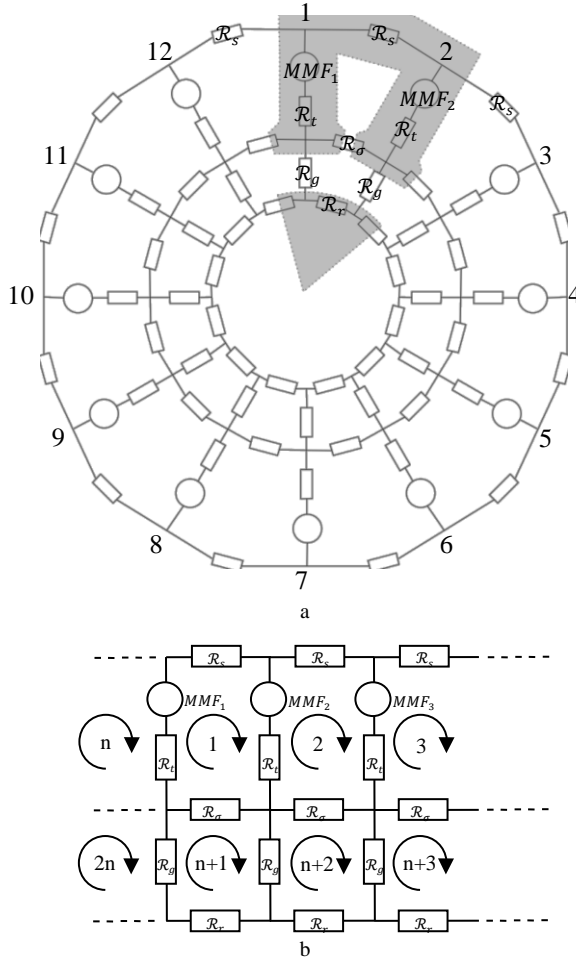


Figure 3.2 Reluctance circuit of a PMSM. Figure a presents the reluctance grid as it is connected in the machine. Figure b presents a more general reluctance grid with its generated flux loops.

Based on the reluctance grid, a reluctance matrix can be formed, where the elements in the matrix represent the total reluctance of each loop presented in Figure 3.2b. The reluctance matrix is expressed as

$$\mathcal{R} = \begin{bmatrix} \sum_{k=1}^{2n} \mathcal{R}_{1,k} & -\mathcal{R}_{1,2} & -\mathcal{R}_{1,3} & \dots & -\mathcal{R}_{1,2n} \\ -\mathcal{R}_{2,1} & \sum_{k=1}^{2n} \mathcal{R}_{2,k} & -\mathcal{R}_{2,3} & \dots & -\mathcal{R}_{2,2n} \\ -\mathcal{R}_{3,1} & -\mathcal{R}_{3,2} & \sum_{k=1}^{2n} \mathcal{R}_{3,k} & \dots & -\mathcal{R}_{3,2n} \\ \vdots & \vdots & \vdots & \ddots & \vdots \\ -\mathcal{R}_{2n,1} & -\mathcal{R}_{2n,2} & -\mathcal{R}_{2n,3} & \dots & \sum_{k=1}^{2n} \mathcal{R}_{2n,k} \end{bmatrix} \quad (3.19)$$

where $\sum_k^{2n} \mathcal{R}_{x,k}$ is the summation of all the reluctance components in contact with loop x . For example, the reluctance part $\mathcal{R}_{1,2}$ is the reluctance component present both in loop 1 and loop 2, i.e. \mathcal{R}_t . However, $\mathcal{R}_{1,3}$ is zero as loop 1 and 3 do not share any reluctance element. The case when $x = k$ refers to the element exclusively present in that loop, for instance $\mathcal{R}_{1,1} = \mathcal{R}_s$. The non-diagonal elements of the matrix are the shared elements of the different loops, where the negative sign is due to the selected reference of positive flow in each loop being defined from the tooth reluctance \mathcal{R}_t towards the *MMF* source (see Figure 3.2b). As the loops only share elements with neighboring loops, the reluctance matrix is a sparse matrix.

The machine coils, represented as *MMF* sources, can be described as a column vector, whose dimension is equal to the number of loops in the reluctance circuit. The elements of the column vector are constituted by the sum of the *MMF* sources within the loop, where the positive direction of flux used for the reluctance matrix needs to be used. For the example circuit presented in Figure 3.2, the *MMF* elements are

$$\mathbf{MMF} = \begin{bmatrix} MMF_1 - MMF_2 \\ MMF_2 - MMF_3 \\ \vdots \\ MMF_n - MMF_1 \\ 0 \\ \vdots \\ 0 \end{bmatrix} \quad (3.20)$$

where the half of the vector is constituted by zero elements, since the loops $n + 1$ to $2n$ represents the rotor circuit (which does not contain any *MMF* source).

Using the *MMF* vector and the reluctance matrix, the flux in each loop can be calculated as

$$\Phi = \mathcal{R}^{-1} \mathbf{MMF} \quad (3.21)$$

where the flux in each tooth is calculated as the difference between the two neighboring loops sharing the tooth reluctance \mathcal{R}_t . Using (3.21), it is possible to calculate the flux distribution generated from a single coil through the excitation of a single MMF_1 source. Figure 3.3 presents the resulting flux in each tooth when only MMF_1 is excited; in the figure, the fluxes are normalized with respect to the flux in tooth 1. It is assumed that MMF_1 is a coil consisting of one turn carrying 1 A and that all teeth have the same positive orientation of flux. In this example, the reluctance of the stator back is small compared to the airgap, which results in the produced flux being distributed across the entire machine.

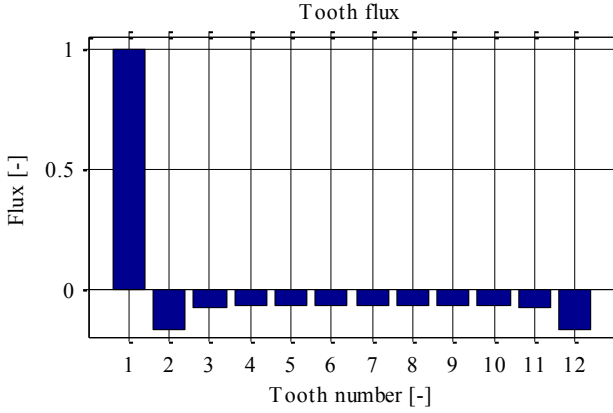


Figure 3.3 Flux distribution from a single coil.

If leakage is neglected, the amount of flux produced by coil x that reaches coil y , i.e. Φ_{xy} can be calculated as

$$\Phi_{xy} = \frac{MMF_x}{\mathcal{R}_{xy}} = \frac{n_x i_x}{\mathcal{R}_{xy}} \quad (3.22)$$

where n_x is the number of turns carrying the current i_x in coil x and \mathcal{R}_{xy} is the reluctance of the flux path from coil x to coil y .

The self-inductance of each coil, L , is defined as the flux produced by the coil multiplied with the number of turns in the coil, in relation to the current flowing in the coil, i.e.

$$L = \frac{\psi_{xx}}{i_x} = \frac{n_x \Phi_{xx}}{i_x} \quad (3.23)$$

ψ_{xx} is the flux linkage originating from coil x and Φ_{xx} is the amount of flux in coil x generated by that coil. The mutual inductance between coils, M , is defined as the

amount of flux linkage produced by coil x that reaches coil y multiplied with the number of turns in coil y , in relation to the current of coil x , i.e.

$$M = \frac{\psi_{xy}}{i_x} = \frac{n_y \Phi_{xy}}{i_x} \quad (3.24)$$

If the machine is assumed to have linear material, i.e. the flux is linearly proportional to the current, the self- and mutual inductances can be simplified by the insertion of (3.22) in to (3.23) and (3.24) respectively. Thus

$$L = \frac{n_x}{I_x} \Phi_{xx} = \frac{n_x n_x I_x}{I_x \mathcal{R}_{xx}} = \frac{n_x^2}{\mathcal{R}_{xx}} \quad (3.25)$$

$$M = \frac{n_y}{I_x} \Phi_{xy} = \frac{n_y n_x I_x}{I_x \mathcal{R}_{xy}} = \frac{n_x n_y}{\mathcal{R}_{xy}} \quad (3.26)$$

which states that for a non-saturated system, the inductance is inversely proportional to the reluctance of the flux paths and cubically proportional to the number of turns.

With the knowledge of the flux distribution, the self- and mutual inductance per tooth and turn can be calculated using (3.25) and (3.26), respectively. With the knowledge of how the phases are distributed among the teeth and how many turns each coil has, the total phase inductance can be evaluated using the inductance values calculated for each tooth winding. The total self-inductance of one phase can be calculated as

$$L = \sum_{i=1}^m \left(\sum_{j=1}^m L_{ij} n_i n_j \right) \quad (3.27)$$

where L_{ii} is the self-inductance of one tooth and L_{ij} is the coupling term from one tooth to another (i.e. the mutual inductance between coils, M). L_{ij} for teeth not belonging to the selected phase are assumed zero when calculating the self-inductance. The terms n_i and n_j are the number of turns surrounding tooth i and j respectively, and m is the total number of teeth.

A similar approach can be applied when calculating the mutual inductance for one phase

$$M = \left(\sum_{i=1}^m \left(\sum_{j=1}^m L_{ij} n_i n_j \right) \right) \quad (3.28)$$

with the difference that L_{ii} is assumed zero.

This subsection presented how the machine geometry can be used to estimate the values of machine inductances. The following subsection describes instead how the machine design impacts the back-EMF.

3.2.3 Buildup of back-EMF

For PMSMs, the back-EMF is induced by the movement of the rotor magnets in relation to the stator coils; the amplitude of the induced voltage, here denoted by e , is defined by Faraday's law of induction as

$$e = -n \frac{d\Phi}{dt} \quad (3.29)$$

where n represents the number of turns through which the flux Φ passes. If the amplitude of the flux from the permanent magnet is considered constant, then the amplitude of the induced voltage is proportional to rotational speed. The waveform of the induced voltage depends on amount of flux within in the coils, which in turn depends on the machine design. Depending on the machine's design (especially the shape of the magnets and the stator teeth), the waveform can vary from sinusoidal to square wave. However, a pure sinusoidal shape with no harmonic components is practically impossible to achieve, but if needed measures can be taken during the machine design to reduce the back-EMF THD. If the machine is to be used in an application where the impact of the harmonics of the back-EMF cannot be neglected, simulation software such as FEM can be used to acquire the needed back-EMF data.

The total induced voltage in one phase is attained through the summation of the induced voltage in all of the series-connected coils of that phase. However, as the coils are spatially distributed within the machine, the voltages induced in the different coils might not be in phase. The spatial distance between coils can be translated into an electrical distance of

$$\varphi = \frac{p n 360^\circ}{\sum c} \quad (3.30)$$

where φ is the electrical distance between two coils, p is the number of pole-pairs, n is the harmonic number and $\sum c$ is total number of coils in the stator. To have a more accurate representation of the total induced voltage in one phase, the contribution from each individual coil (including the harmonic content) should be treated as vectors, characterized by an amplitude and a phase. Because of the electrical distance between coils, the phase of the induced voltage for each coil is likely to be shifted. Machines typically have a symmetric distribution, giving a constant coil displacement that results in a fixed phase difference between two neighboring coils. As an illustrative example, the buildup of fundamental component of the back-EMF of a machine with six coils is illustrated in Figure 3.4, where each short black arrow represents the contribution from a single coil to the total back-EMF (red arrow); the

latter can be measured while the machine is operating in open circuit mode (no current).

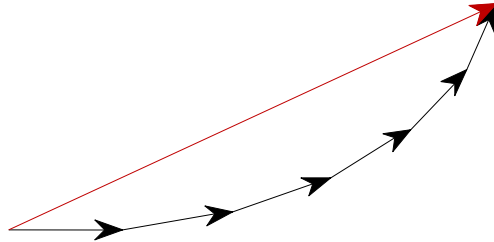


Figure 3.4 Example of the buildup of phase back-EMF for one phase, where the long red arrow presents the resulting back-EMF.

The shape of the back-EMF can also be influenced by selecting the winding direction of the coil as a means to reduce the electrical distance between coils, which is utilized in Section 4.1.1. The principle can clearly be seen through the simple example in Figure 3.5, where although the two coils are both separated by 150° , the different winding direction results in different amplitude and phase for the resulting total back-EMF vector.



Figure 3.5 Build-up of phase back-EMF for one phase, left 150° shift and right -30° shift. The red arrow represents the sum of the two black arrows.

The winding direction of the coils is typically arranged to maximize the amplitude of fundamental component of the back-EMF; however, as can be seen from (3.30) and from Figure 3.5, the coil distribution also has an impact on its harmonic content.

3.3 PMSM model with a turn-to-turn fault

When a turn-to-turn fault occurs in any phase of a PMSM, the affected phase (for example, phase a) changes from a non-faulted state into a faulted state, as indicated in Figure 3.6. As shown in the figure, under this condition the phase winding can be modelled as two series-connected circuits, representing the fault loop and the remaining winding turns with the corresponding induced voltage. Denoting with u_a the voltage across the non-faulted phase, the voltages u_1 and u_2 in Figure 3.6b are the resulting voltages over the two parts.

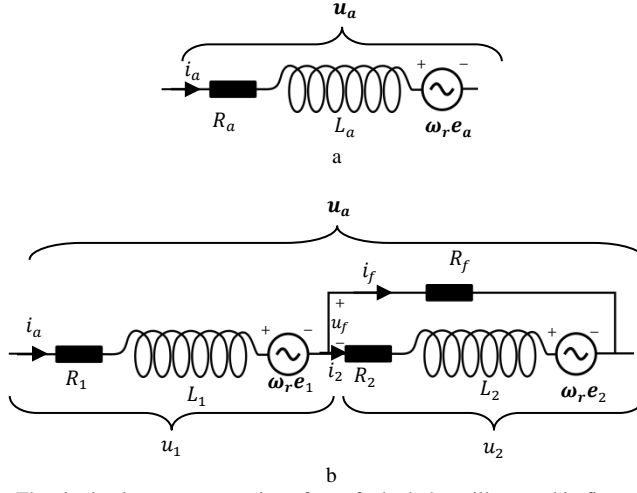


Figure 3.6 The single phase representation of non-faulted phase illustrated in figure a, and figure b presents the single phase representation of the affected phase in the case of a turn-to-turn fault.

Under the assumption of linear properties of the machine, the equations describing the faulted phase are

$$u_1 = R_1 i_a + L_1 \frac{di_a}{dt} + M_{21} \frac{d(i_a - i_f)}{dt} + M_{1b} \frac{di_b}{dt} + M_{1c} \frac{di_c}{dt} + \omega_r e_1 \quad (3.31)$$

$$u_2 = R_2 (i_a - i_f) + L_2 \frac{d(i_a - i_f)}{dt} + M_{12} \frac{di_a}{dt} + M_{2b} \frac{di_b}{dt} + M_{2c} \frac{di_c}{dt} + \omega_r e_2 \quad (3.32)$$

where R_i is the resistance (with $i = 1, 2$ in reference to Figure 3.6b), L_i is the self-inductance, e_i is the back-EMF and M_{ij} is the mutual inductance (where j can be either 1, 2, b or c). The term R_f represents the contact resistance between the short-circuited turns. As the number of turns and amount of copper used in the machine has not been altered due to the turn-to-turn fault, it can be assumed that

$$u_1 + u_2 = u_a, \quad R_1 + R_2 = R_a, \quad u_2 = R_f i_f \quad (3.33)$$

It is of importance to observe that due to the uneven temperature distribution during the fault, R_a in (3.33) cannot be considered constant over time. However, as the resistive part of the stator impedance is typically much smaller than the reactive component, the error introduced by the variation of this resistance can be considered negligible and does not affect the validity of the overall model. Thus, the phase voltage u_a for the faulted machine is modelled as

$$u_a = R_a i_a + L_a \frac{di_a}{dt} + M_{ab} \frac{di_b}{dt} + M_{ac} \frac{di_c}{dt} + \omega_r e_a - R_2 i_f - (M_{21} + L_2) \frac{di_f}{dt} \quad (3.34)$$

with the self-inductance L_a defined as the sum of the self-inductances from both parts in Figure 3.6b together with their mutual couplings, i.e.

$$L_a = L_1 + L_2 + M_{12} + M_{21} \quad (3.35)$$

Under the assumption of linear material for the machine, the mutual coupling between the faulted phase and the other non-faulted phases is then equal to the sum of the coupling of the two circuits in Figure 3.6b to the other phases, i.e.

$$M_{ab} = M_{1b} + M_{2b}, \quad M_{ac} = M_{1c} + M_{2c} \quad (3.36)$$

The new short-circuit loop created by the turn-to-turn fault can be described as

$$u_f = 0 = (R_f + R_2)i_f - R_2i_a + L_2 \frac{di_f - i_a}{dt} - M_{12} \frac{di_a}{dt} - M_{2b} \frac{di_b}{dt} - M_{2c} \frac{di_c}{dt} + \omega_r e_2 \quad (3.37)$$

where the negative sign on the mutual couplings is due to the selected direction for the current i_f being opposite to i_a (see Figure 3.6b). If the machine is assumed to be symmetrical, the following simplifications can be made:

$$R_a = R_b = R_c = R_s \quad (3.38)$$

$$L_a = L_b = L_c = L \quad (3.39)$$

$$M_{ab} = M_{ac} = M_{bc} = M \quad (3.40)$$

In order to simplify the analytical expression of the faulted PMSM, a new parameter σ is defined, equal to the ratio between the number of short-circuited turns and the total number of turns in the faulted phase [28]:

$$\sigma = \frac{N_2}{N_a} \quad (3.41)$$

Using σ , the resistances R_1 and R_2 can then be defined as

$$\begin{aligned} R_1 &= (1 - \sigma)R_s \\ R_2 &= \sigma R_s \end{aligned} \quad (3.42)$$

It is important to stress that for some machine designs, all parameters related to the fault (such as R_1 , L_1 and M_{12}) can be derived using σ , as in the case of the resistances shown in (3.42). However, this relation does not hold in case of machines with more pole-pairs or for machines with more complex geometry (such as distributed windings) [22]. Because the derivation of a generic model of a faulted PMSM is the aim of this investigation, the parameter σ should only be used to describe the resistive elements of the machine. Since the inductances have a non-linear relation with the number of turns, the parameter σ cannot be used to model the inductive elements for generic machines, as σ is linearly dependent on the number of short-circuited turns.

To acquire the inductance values, a reluctance grid or finite element software is needed in order to account for all the internal magnetic couplings.

Using σ for the resistive terms only, the generic three phase faulted PMSM can be described in matrix form as

$$\begin{aligned} \begin{bmatrix} u_a \\ u_b \\ u_c \\ u_f (= 0) \end{bmatrix} &= \begin{bmatrix} R_s & 0 & 0 & -\sigma R_s \\ 0 & R_s & 0 & 0 \\ 0 & 0 & R_s & 0 \\ -\sigma R_s & 0 & 0 & \sigma R_s + R_f \end{bmatrix} \begin{bmatrix} i_a \\ i_b \\ i_c \\ i_f \end{bmatrix} \\ + \begin{bmatrix} L & M & M & -(M_{1f} + L_f) \\ M & L & M & -M_{bf} \\ M & M & L & -M_{cf} \\ -(M_{1f} + L_f) & -M_{bf} & -M_{cf} & L_f \end{bmatrix} \frac{d}{dt} \begin{bmatrix} i_a \\ i_b \\ i_c \\ i_f \end{bmatrix} + \omega_r \begin{bmatrix} e_a \\ e_b \\ e_c \\ -e_f \end{bmatrix} \end{aligned} \quad (3.43)$$

where e_i is the back-EMF of the three phase windings, and the fault winding and the subscript “2” is substituted with “f” to refer to the faulted part of the winding. As a simple estimation, the amplitude of e_f can be approximated to σe_a ; however, if the coils are heavily electrically scattered, resulting in a large phase difference between the faulted turns and the affected phase, the approximation becomes less accurate. To have a more accurate representation of e_f , knowledge of the actual induced voltage in the faulted turns is needed; this information can typically be acquired using a FEM model. The negative sign of e_f is due to the selected direction of the fault current i_f being opposite to i_a , see Figure 3.6b.

To be able to implement the model of the faulted machine in to a simulation, it can be rearranged into the state-space form.

3.3.1 State-space representation of faulted model

The faulty machine described by (3.43) can be more densely described as

$$\mathbf{v}_{abcf} = \mathbf{R} \mathbf{i}_{abcf} + \mathbf{L} \frac{d\mathbf{i}_{abcf}}{dt} - \mathbf{e}_{abcf} \quad (3.44)$$

and if (3.44) is re-arranged into the state-space form it becomes

$$\frac{d\mathbf{I}_{abcf}}{dt} = \mathbf{L}^{-1}(\mathbf{V}_{abcf} - \mathbf{R} \mathbf{I}_{abcf} + \mathbf{E}_{abcf}). \quad (3.45)$$

where

$$\mathbf{A} = \mathbf{L}^{-1}(-\mathbf{R}) \quad (3.46)$$

$$\mathbf{B} = \mathbf{L}^{-1}\mathbf{u}_{mat} \quad (3.47)$$

$$\mathbf{C} = \mathbf{I} \quad (3.48)$$

$$\mathbf{D} = 0 \quad (3.49)$$

By selecting the terminal voltages and the electrical speed of the machine as inputs, \mathbf{u}_{mat} for the faulted machine becomes

$$\mathbf{U}_{mat} = \begin{bmatrix} 1 & 0 & 0 & e_a \\ 0 & 1 & 0 & e_b \\ 0 & 0 & 1 & e_c \\ 0 & 0 & 0 & -e_f \end{bmatrix} \quad (3.50)$$

Evaluating the \mathbf{A} and \mathbf{B} matrixes results in a large analytical expressions for each element. Equation (3.51) presents the structure of the matrixes after some algebraic and trigonometric reduction:

$$\mathbf{A} = \begin{bmatrix} A_{11} & A_{12} & A_{13} & A_{14} \\ A_{21} & A_{22} & A_{23} & A_{24} \\ A_{31} & A_{32} & A_{33} & A_{34} \\ A_{41} & A_{42} & A_{43} & A_{44} \end{bmatrix} \quad (3.51)$$

$$\mathbf{B} = \begin{bmatrix} B_{11} & B_{12} & B_{13} & \beta_{14}e_a \\ B_{21} & B_{22} & B_{23} & \beta_{24}e_b \\ B_{31} & B_{32} & B_{33} & \beta_{34}e_c \\ B_{41} & B_{42} & B_{43} & \beta_{44}e_f \end{bmatrix}$$

where the terms A_{ij} and B_{ij} are constants consisting solely of different mathematical combinations of the parameters of the faulted machine. Since the matrixes for the state-space representation of the faulted model only consist of constants (except the last column of the \mathbf{B} matrix), a sinusoidal input signal results in a sinusoidal output at the same frequency. In essence, the turn-to-turn fault does not introduce any new frequency components in the machine currents, but rather affects their amplitude and phase. If only a few of the total number of turns are short-circuited, the alteration on the currents introduced by the fault will most likely be small and thus difficult to detect.

3.4 PMSM model with a turn-to-turn fault in the synchronously rotating reference frame

A three phase machine with a turn-to-turn fault can be modeled as a machine with four windings, where the fourth winding represents the short-circuited loop in the faulty phase. Therefore, in order to transform the model of the faulty machine into the synchronously-rotating reference frame, the amplitude-invariant transformation matrix used in this thesis is

$$T'(\theta_r) = \frac{2}{3} \begin{bmatrix} \cos \theta_r & \cos\left(\theta_r - \frac{2\pi}{3}\right) & \cos\left(\theta_r + \frac{2\pi}{3}\right) & 0 \\ -\sin \theta_r & -\sin\left(\theta_r - \frac{2\pi}{3}\right) & -\sin\left(\theta_r + \frac{2\pi}{3}\right) & 0 \\ 0 & 0 & 0 & \frac{3}{2} \end{bmatrix} \quad (3.52)$$

$$T'^{-1}(\theta_r) = \begin{bmatrix} \cos \theta_r & -\sin \theta_r & 0 \\ \cos\left(\theta_r - \frac{2\pi}{3}\right) & -\sin\left(\theta_r - \frac{2\pi}{3}\right) & 0 \\ \cos\left(\theta_r + \frac{2\pi}{3}\right) & -\sin\left(\theta_r + \frac{2\pi}{3}\right) & 0 \\ 0 & 0 & 1 \end{bmatrix} \quad (3.53)$$

where θ_r is the electrical position of the rotor's north pole. The angle θ_r is chosen to be zero when the rotor's north pole is aligned with the positive magnetic axis of phase a . Observe that the zero-sequence component is neglected in the transformation, to avoid singularities when the model is implemented in a state-space model form, where the singularities are originated from the inverse of the machine inductance matrix. However, as long as the machine utilizes a floating neutral point, the zero sequence component can be neglected as it does not affect the machine operation.

It should be stressed that in (3.52) the fault current is not transferred into the rotating reference frame and will remain an AC-quantity in the rotating reference frame. The three-phase quantities are instead transformed, making their fundamental component appear as DC-quantity in the rotating reference frame. The currents will however not be pure DC-quantities, as the fault creates an imbalance between the phases. This unbalance will introduce an oscillating component, as is shown by the equations describing the faulty machine in the rotating reference frame.

By applying the transformation matrix to the model of the faulty machine described by (3.44) yields

$$T'^{(\theta_r)} \mathbf{v}_{abc f} = T'^{(\theta_r)} \mathbf{R} \mathbf{i}_{abc f} + T'^{(\theta_r)} \mathbf{L} \frac{d\mathbf{i}_{abc f}}{dt} - T'^{(\theta_r)} \mathbf{e}_{abc f} \quad (3.54)$$

By utilizing

$$\mathbf{i}_{abc f} = T'^{-1}(\theta_r) \mathbf{i}_{dqf} \quad (3.55)$$

then

$$T'^{(\theta_r)} \mathbf{v}_{abc f} = T'^{(\theta_r)} \mathbf{R} T'^{-1}(\theta_r) \mathbf{i}_{dqf} + T'^{(\theta_r)} \mathbf{L} \frac{dT'^{-1}(\theta_r) \mathbf{i}_{dqf}}{dt} - T'^{(\theta_r)} \mathbf{e}_{abc f} \quad (3.56)$$

Evaluation of the derivative term gives

$$T'^{(\theta_r)} \mathbf{L} \frac{dT'^{-1}(\theta_r) \mathbf{i}_{dqf}}{dt} = T'^{(\theta_r)} \mathbf{L} \frac{dT'^{-1}(\theta_r)}{dt} + T'^{(\theta_r)} \mathbf{L} T'^{-1}(\theta_r) \frac{d\mathbf{i}_{dqf}}{dt} \quad (3.57)$$

Inserting (3.57) into (3.54) gives

$$\mathbf{v}_{dqf} = \mathbf{R}' \mathbf{i}_{dqf} + d\mathbf{L}' \mathbf{i}_{dqf} + \mathbf{L}' \frac{\partial \mathbf{i}_{dqf}}{\partial t} - \mathbf{e}_{dqf} \quad (3.58)$$

where

$$\mathbf{v}_{dqf} = T'(\theta_r) \mathbf{v}_{abcf} \quad (3.59)$$

$$\mathbf{R}' = T'(\theta_r) \mathbf{R} T'^{-1}(\theta_r) \quad (3.60)$$

$$d\mathbf{L}' = T'(\theta_r) \mathbf{L} \frac{\partial T'^{-1}(\theta_r)}{\partial t} \quad (3.61)$$

$$\mathbf{L}' = T'(\theta_r) \mathbf{L} T'^{-1}(\theta_r) \quad (3.62)$$

$$\mathbf{e}_{dq0f} = T'(\theta_r) \mathbf{e}_{abcf} \quad (3.63)$$

Therefore, the equations describing the faulty machine in the rotating reference frame are given by

$$\begin{aligned} \begin{bmatrix} u_d \\ u_q \\ u_f (= 0) \end{bmatrix} &= \begin{bmatrix} R_s & -(L-M)\omega_r & -\sigma \frac{2R_s \cos(\theta_r)}{3} \\ (L-M)\omega_r & R_s & \sigma \frac{2R_s \sin(\theta_r)}{3} \\ K_1 \cos(\theta_r - K_2) & K_1 \cos(\theta_r - K_3) & R_f + \sigma R_s \end{bmatrix} \begin{bmatrix} i_d \\ i_q \\ i_f \end{bmatrix} \\ &+ \begin{bmatrix} L-M & 0 & \frac{3}{2} K_4 \cos(\theta_r - K_5) \\ 0 & L-M & \frac{3}{2} K_4 \cos(\theta_r - K_6) \\ K_4 \cos(\theta_r - K_5) & K_4 \cos(\theta_r - K_6) & L_f \end{bmatrix} \frac{d}{dt} \begin{bmatrix} i_d \\ i_q \\ i_f \end{bmatrix} \\ &+ \omega_r \Psi_{pm} \begin{bmatrix} 0 \\ 1 \\ E_f \sin(\theta_r + \varphi) \end{bmatrix} \end{aligned} \quad (3.64)$$

where

$$K_1 = -\frac{1}{2} \sqrt{(-2M_{af} + M_{bf} + M_{cf} - 2L_f)^2 \omega_r^2 + (-2\sigma R_s + \sqrt{3}(-M_{bf} + M_{cf})\omega_r)^2} \quad (3.65)$$

$$K_2 = \tan^{-1} \left(\frac{(-2M_{af} + M_{bf} + M_{cf} - 2L_f)\omega_r}{2\sigma R_s + \sqrt{3}(M_{bf} - M_{cf})\omega_r} \right) \quad (3.66)$$

$$K_3 = \tan^{-1} \left(\frac{-2\sigma R_s - \sqrt{3}(M_{bf} - M_{cf})\omega_r}{(-2M_{af} + M_{bf} + M_{cf} - 2L_f)\omega_r} \right) \quad (3.67)$$

$$K_4 = -\frac{1}{2} \sqrt{(-2M_{af} + M_{bf} + M_{cf} - 2L_f)^2 + 3(M_{bf} - M_{cf})^2} \quad (3.68)$$

$$K_5 = \tan^{-1} \left(\frac{\sqrt{3}(-M_{bf} + M_{cf})}{-2M_{af} + M_{bf} + M_{cf} - 2L_f} \right) \quad (3.69)$$

$$K_6 = \tan^{-1} \left(\frac{-2M_{af} + M_{bf} + M_{cf} - 2L_f}{\sqrt{3}(M_{bf} - M_{cf})} \right) \quad (3.70)$$

As can be seen in (3.64), the fault current's contribution to both the d - and q -current contains either a sine or cosine function. Therefore (as mentioned earlier) the d - and

q -currents will not be pure DC-quantities in the event of a turn-to-turn fault, as an oscillating component is introduced. The sine and cosine functions in (3.64) originate from the described coordinate transformation; however, as the sine and cosine functions only appear in the third column of the matrixes, they only interact with the fault current, which is inherently an AC quantity. Therefore, the frequency content of the d - and q -currents depends on the fault current (which has a sinusoidal shape) multiplied with the sine and cosine functions introduced by the transformation. This results in two new frequency components: a DC and a double frequency component. For the investigated system, the latter corresponds to twice the electrical speed.

The frequency of the fault current depends on the electrical speed of the machine; on the other hand, the angle used for the coordinate transformation is also a function of the electrical speed of the machine. Therefore, two frequency components will appear: a zero-frequency component and a double-frequency component. As such, a turn-to-turn fault will introduce a negative-sequence component in both the d - and q -currents. As can be observed in (3.64), the fault current affects the d - and q -currents equally with regards to amplitude. However, the fault current contribution is 90° electrically shifted between the d - and q -currents as K_2 is 90° shifted from K_3 , as can be seen in (3.66) and (3.67). It can also be seen that this applies for K_5 and K_6 .

The faulty machine model in the rotating reference frame can also be transformed into a state-space form, in order to more clearly visualize how the different model inputs contribute to the outputs. Using the same approach as in the previous section gives

$$\frac{d\mathbf{i}_{dqf}}{dt} = \mathbf{L}'^{-1}(\mathbf{v}_{dqf} - \mathbf{R}'\mathbf{i}_{dqf} - d\mathbf{L}'\mathbf{i}_{dqf} + \mathbf{e}_{dqf}) \quad (3.71)$$

$$\mathbf{A} = \mathbf{L}'^{-1}(-\mathbf{R}' - d\mathbf{L}') \quad (3.72)$$

$$\mathbf{B} = \mathbf{L}'^{-1}\mathbf{U}_{mat} \quad (3.73)$$

$$\mathbf{C} = \mathbf{I} \quad (3.74)$$

$$\mathbf{D} = \mathbf{0} \quad (3.75)$$

where

$$\mathbf{U}_{mat} = \begin{bmatrix} 1 & 0 & 0 \\ 0 & 1 & -\Psi_{pm} \\ 0 & 0 & \Psi_{pm}E_f \sin(\theta_r + \varphi) \end{bmatrix}, \mathbf{u} = \begin{bmatrix} u_d \\ u_q \\ \omega_r \end{bmatrix} \quad (3.76)$$

Evaluating the \mathbf{A} and \mathbf{B} matrixes results in large and complex analytical equations, as for the model implemented in the stationary reference frame. However, after some algebraic and trigonometric reduction, the structure of the matrixes becomes

$$\mathbf{A} = \begin{bmatrix} A_{11} + \alpha_{11} \cos(2\omega_r t + \varphi_{11}) & A_{12} + \alpha_{12} \cos(2\omega_r t + \varphi_{12}) & \alpha_{13} \cos(\omega_r t + \varphi_{13}) \\ A_{21} + \alpha_{21} \cos(2\omega_r t + \varphi_{21}) & A_{22} + \alpha_{22} \cos(2\omega_r t + \varphi_{22}) & \alpha_{23} \cos(\omega_r t + \varphi_{23}) \\ \alpha_{31} \cos(\omega_r t + \varphi_{31}) & \alpha_{32} \cos(\omega_r t + \varphi_{32}) & A_{33} \end{bmatrix} \quad (3.77)$$

$$\mathbf{B} = \begin{bmatrix} B_{11} + \beta_{11} \cos(2\omega_r t + \psi_{11}) & \beta_{12} \cos(2\omega_r t + \psi_{12}) & B_{13} + \beta_{13} \cos(2\omega_r t + \psi_{13}) \\ \beta_{21} \cos(2\omega_r t + \psi_{21}) & B_{22} + \beta_{22} \cos(2\omega_r t + \psi_{22}) & B_{23} + \beta_{23} \cos(2\omega_r t + \psi_{23}) \\ \beta_{31} \cos(\omega_r t + \psi_{31}) & \beta_{32} \cos(\omega_r t + \psi_{32}) & \beta_{33} \cos(\omega_r t + \psi_{33}) \end{bmatrix} \quad (3.78)$$

where A_{ij} , α_{ij} , B_{ij} , β_{ij} , φ_{ij} , and ψ_{ij} are all constants consisting solely of different mathematical combinations of the machine parameters of the faulty machine. It is important to stress that the constants (such as A_{ij} and B_{ij}) do not have the same value as for the machine model in the stationary reference frame described in (3.16) and (3.17). The complete expression of the constants in \mathbf{A} and \mathbf{B} for the machine in the rotating reference frame is given in Appendix C. These matrix structures show that a PMSM with a turn-to-turn fault behaves like an unbalanced machine, i.e. any single frequency input in the stationary reference frame will be seen as two frequency components in the rotating reference frame.

3.5 Flexible analytical model

Assuming that the original state of a machine is non-faulted and, after some time, the insulation of the stator winding fails (see Section 2.4), causing a turn-to-turn fault that turns the non-faulted machine in to a faulted machine. In order to simulate this behavior, there is a need to develop a model that is able to switch from a non-faulted state to a faulted state. This model feature would allow the study of the behavior of the machine before and after the fault occurs given the identical operational conditions, which is utilized in Section 5.4. As the faulted model is derived from the non-faulted one, it still contains all its information. As a result, the faulted model can, after some manipulation, be used to emulate both machines' conditions. However, as the models assume linear material properties it may not be able to accurately model any transient behavior during the transition between the states. From the method by which the faulted machine is modeled, the faulty behavior is caused by the presence of the fault current i_f and its interaction with the other currents. Hence, by keeping i_f equal to zero, the faulty machine model is effectively the same as the non-faulted machine model. In essence, it is possible to create a model which is able to transition from a non-faulted to a faulted state by first preventing the fault current and then being able to re-enable it when faulted operation is desired.

One method to prevent the circulation of the fault current is to have a variable value of the emulated contact resistance R_f , since selecting an infinite value represents an open circuit, i.e. no fault. By reducing the value of R_f the fault is introduced, where a zero value represents a perfect short circuit between two conductors. However, simply selecting the value of R_f to be infinitely large is not a practical solution for analytical implementation. When solving the state-space equations, a large value of R_f leads to large derivative terms, which requires an impractically small simulation time step in order to guarantee the convergence of the simulation. An alternative way to simulate the transition between the non-faulted and the faulted machine model is to modify the fault loop by adding a controllable voltage source, u_f , in series with the resistance R_f , see Figure 3.7. The model with the added voltage source is referred to as the flexible model in this thesis.

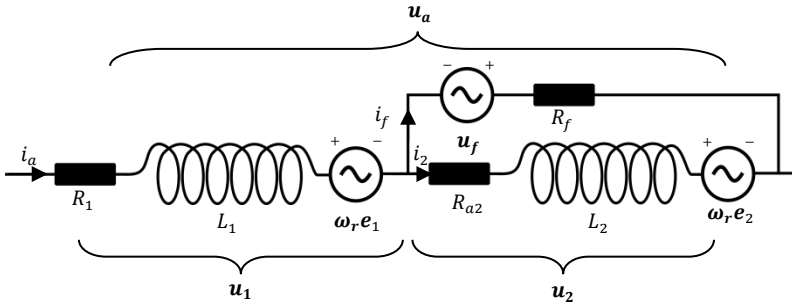


Figure 3.7 The circuit representation of the faulted phase of the flexible model, which includes the controllable voltage u_f , in series with R_f .

During non-faulted operation, the voltage level of u_f is for each time step selected to maintain the fault current derivative at zero, without affecting the other currents. To model the faulted machine, the value of u_f is forced to zero as in the case presented in Section 3.3. Thus, having zero fault current as the initial condition of the flexible model will cause it to remain at zero. The level of u_f for the non-faulted operation is calculated using (3.45).

To verify the effectiveness of this approach, the flexible model is compared with a non-faulted machine model with the same parameter values. The simulation results are presented in Figure 3.8. As it can be noticed from the obtained results, the two models can be considered to be identical; this can also be appreciated by evaluating the error between the two models, depicted in Figure 3.8b. To verify that the flexible model is able to switch from a non-faulted to a faulted state, the voltage of the voltage source is forced to zero after 10 ms. Figure 3.8c shows the fault current of the flexible model; as expected, there is no fault current until it is enabled after 10 ms. Hence, the flexible model can be used to model both non-faulted machines and machines with turn-to-turn faults.

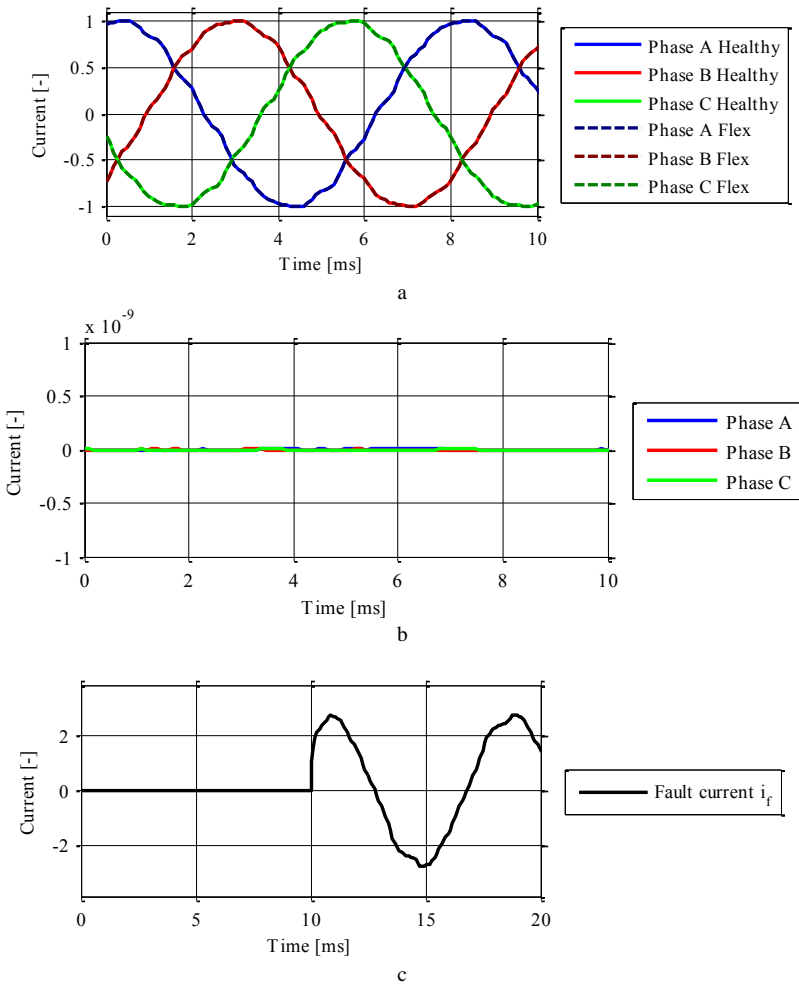


Figure 3.8 Comparison of simulation results from the non-faulted and flexible models. Figure a presents both simulation results and figure b presents the difference between the two models. Figure c presents the simulated fault current i_f . All are normalized with respect to the peak current of the non-faulted machine.

3.6 PMSM with parallel windings and turn-to-turn fault

In larger machines with higher power levels (such as wind power generators), the use of parallel windings is a common method to reduce the voltage rating at the expense of increasing the current rating of the machine. The use of parallel windings does however lead to circulating currents in the phase branches, unless the machine is identical in all branches. Since this is practically impossible to achieve, typically a

small circulating current exist, but its impact can generally be neglected during normal operation due to its comparably small amplitude. However, as previously stated, a turn-to-turn causes the machine to become asymmetric, causing an increase in the circulating current.

To analytically model a machine with parallel windings and a turn-to-turn fault, the model presented in Section 3.3 can be extended to incorporate the parallel branches. The extended circuit model for a machine with two parallel branches is presented in Figure 3.9,

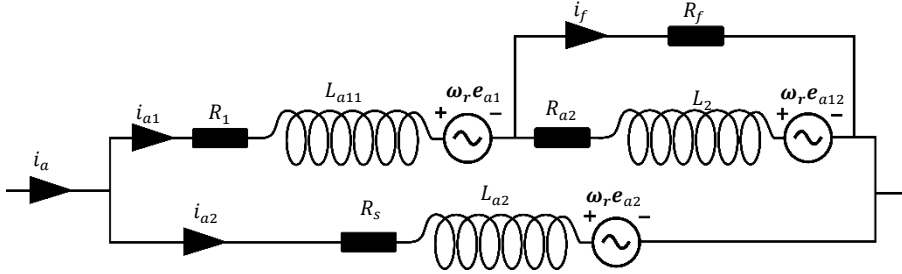


Figure 3.9 Circuit model of the phase with the turn-to-turn fault of a PMSM with two parallel windings.

where i_a is the phase current and i_{a1} and i_{a2} are branch currents. The amplitude of the circulating current during a turn-to-turn fault depends on several factors, such as the number of parallel branches, the number of turns short-circuited, the fault resistance and the external loading/operation condition. More affected turns lead to a higher current, and a low fault resistance results in both a large fault current as well as in a larger circulating current. The machine's external loadings also influence the circulating current, where the circulating current is inversely proportional to the external loading, i.e. the highest circulating current with respect to external loading occurs during no-load/open circuit operation. It is therefore difficult to draw any general conclusion regarding the amplitude of the circulating current. In order to be able to estimate the circulating current using models, the operational conditions must to be known.

By using the same approach described in Section 3.3, an analytical model of a PMSM with parallel windings can be derived. The size of the square matrixes describing the model will be $np_l + 1$ where n is the number of phases, p_l is the number of parallel branches and the plus one term is due to the fault. As an example, for a three phase machine with two parallel windings, the resistance and inductance matrixes will be $[7 \times 7]$, where the resistance matrix will be diagonal except the additional fault resistance entries in the last row and column (as in the case presented in (3.43)). The inductance matrix may be a full matrix, depending on the machine design (as all windings can be magnetically coupled). Accordingly, a generic model of a PSMS with n number of parallel windings with a turn-to-turn fault in the first branch of phase a can be modelled as

$$\begin{aligned}
\begin{bmatrix} u_{a1} \\ \vdots \\ u_{an} \\ u_{b1} \\ \vdots \\ u_{bn} \\ u_{c1} \\ \vdots \\ u_{cn} \\ u_f (= 0) \end{bmatrix} &= \begin{bmatrix} R_s & 0 & \cdots & 0 & -\sigma R_s \\ 0 & R_s & \cdots & 0 & 0 \\ \vdots & \vdots & \ddots & \vdots & \vdots \\ 0 & 0 & \cdots & R_s & 0 \\ -\sigma R_s & 0 & \cdots & 0 & \sigma R_s + R_f \end{bmatrix} \begin{bmatrix} i_{a1} \\ \vdots \\ i_{an} \\ i_{b1} \\ \vdots \\ i_{bn} \\ i_{c1} \\ \vdots \\ i_{cn} \\ i_f \end{bmatrix} - \omega_r \begin{bmatrix} e_{a1} \\ \vdots \\ e_{an} \\ e_{b1} \\ \vdots \\ e_{bn} \\ e_{c1} \\ \vdots \\ e_{cn} \\ -e_f \end{bmatrix} \\
+ \begin{bmatrix} L_{a1} & M_{a1a2} & \cdots & M_{a1cn} & -(M_{a1f} + L_f) \\ M_{a1a2} & L_{a2} & \cdots & M_{a2cn} & -M_{a2f} \\ \vdots & \vdots & \ddots & \vdots & \vdots \\ M_{a1cn} & M_{a2cn} & \cdots & L_{cn} & -M_{cnf} \\ -(M_{a1f} + L_f) & -M_{a2f} & \cdots & -M_{cnf} & L_f \end{bmatrix} \frac{d}{dt} \begin{bmatrix} i_{a1} \\ \vdots \\ i_{an} \\ i_{b1} \\ \vdots \\ i_{bn} \\ i_{c1} \\ \vdots \\ i_{cn} \\ i_f \end{bmatrix}
\end{aligned} \tag{3.79}$$

For ideal machines, the parallel phase voltages and currents are identical, i.e.

$$u_{x1} = u_{x2}, \quad i_{x1} = i_{x2}, \quad e_{x1} = e_{x2} \tag{3.80}$$

As for the machine without parallel windings, the values of the self-inductance can be assumed to be equal for all phases; however, in the case of the mutual couplings this may not be true for all machines as it depends on the winding distribution. For such machines either a reluctance grid or a FEM model is needed in order to acquire the mutual coupling between individual branches.

The presented model can be used to estimate the circulating current which occurs during no-load operation in order to investigate if the amplitude of circulating current is sufficient to cause additional stress or damage the machine. In order to simplify the analysis, only the steady-state circulating current is considered as it allows phasor representation of the machine branches. To further simplify the model the mutual couplings are neglected, hence the phasor describing branch x can be represented as

$$u_x \angle \varphi = R_s i_x + j\omega_r L i_x + \omega_r \Psi_{pm} \angle 0 \tag{3.81}$$

and for the branch with the fault, the phasor representation can be estimated to

$$u_{xf} \angle \varphi = R_s k i_{xf} + j\omega_r L k^2 i_{xf} + k\omega_r \Psi_{pm} \angle \varphi_f \tag{3.82}$$

where k is defined as $1 - \sigma$. The φ_f term is introduced to account for any phase shift in the back-EMF caused by the fault. The amplitude of the back-EMF is estimated to be proportional to the number of lost turns, though this may not be completely accurate depending on the coil distances of the machine as discussed in Section 3.2.3.

The parallel winding connection enforces that the voltages $u_x = u_{xf}$ and that the branch currents $i_x = -i_{xf}/(p_l - 1)$. Adding these conditions to (3.81) and (3.82) gives

$$R_s \left(k + \frac{1}{(p_l - 1)} \right) i_{xf} + j\omega_r L \left(k^2 + \frac{1}{(p_l - 1)} \right) i_{xf} = \omega_r \Psi_{pm} (1 - k\angle\varphi_f) \quad (3.83)$$

The simplified estimation of current in the faulted branch during no-load operation can be thus be described as

$$i_{xf} = \omega_r \Psi_{pm} \frac{(1 - k\angle\varphi_f)}{R_s \left(k + \frac{1}{(p_l - 1)} \right) + j\omega_r L \left(k^2 + \frac{1}{(p_l - 1)} \right)} \quad (3.84)$$

If the stator resistance is neglected, then the current in the faulted branch becomes

$$i_{xf} = -\frac{j\Psi_{pm}}{L} \frac{(1 - k\angle\varphi_f)}{\left(k^2 + \frac{1}{(p_l - 1)} \right)} \quad (3.85)$$

For non-faulted operation ($k = 1$) there is no circulating current as the numerator in (3.84) is zero (the phase difference φ_f introduced by the fault is zero, i.e. if $k = 1$ then $\varphi_f = 0$). Figure 3.10 presents the steady-state amplitude of the current in the non-faulted part of the affected branch as a function of k and p_l . The amplitude is given relative the resulting current during a complete short-circuit of one branch (i.e. $k = 0$).

Depending on the machine design, the branch short-circuit current may be several times larger than rated current. For those machine designs, severe turn-to-turn faults can cause circulating currents which are greater than the machine's rated current, which may cause additional winding damage or demagnetize the permanent magnets.

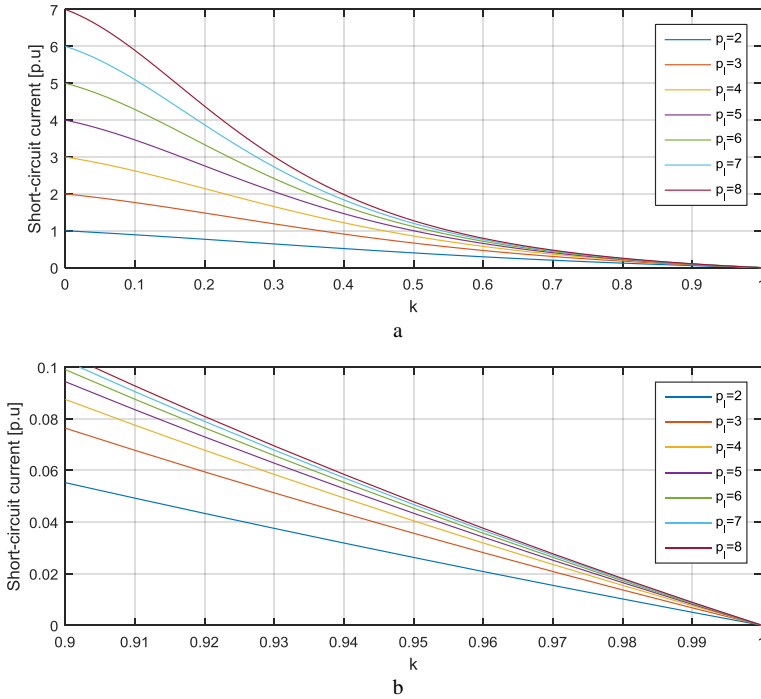


Figure 3.10 Circulating current in the case of turn-to-turn fault for various degrees of short-circuited turns and number of parallel branches.

3.7 Chapter summary

This chapter has dealt with the analytical model of both a non-faulted and a PMSM with a turn-to-turn fault. The model of the faulty machine has been mathematically transformed into the rotating reference frame; it has been shown that additional frequency components in the rotating reference frame are introduced due to the imbalance caused by the fault. A flexible model that is able to transition from a non-faulted state to the faulted state during a simulation has also been presented. The analytical model has been extended to be able to include machines with parallel windings.

The following chapter presents FEM models of the PMSMs with turn-to-turn faults. The FEM models are used to validate the analytical models presented in this chapter.

Chapter 4

FEM Modeling of Permanent Magnet Synchronous Machine

This chapter presents the FEM models that are used to verify the analytical models presented in the previous chapter. A model of a non-faulted machine is presented for reference purposes. To model the faulted turns in the faulted machine, an additional winding is added to the non-faulted FEM model. In order to correct resemble the internal connections of the fault winding and the affected phase, the FEM software is coupled to a circuit software in a co-simulation environment.

4.1 FEM model of non-faulted machine

In order to validate the analytical model presented in the previous chapter and to acquire the needed inductance and back-EMF values, a FEM model has been developed using ANSYS Maxwell [34]. Two PMSM models with different design are presented in this chapter: one smaller machine and one larger with parallel windings. The small machine model presented in this section is based on a prototype machine available at the electrical machine laboratory at Chalmers University of Technology; this machine has been selected due to the availability of the parameter values. The machine has a continuous power rating of 30 kW and a rated line-to-line voltage rating of 270 V. Although this prototype machine has been designed for the automotive industry, the previously presented analytical models are independent from the machine's application, as the analytical model describes a generic PMSM. In addition, as the FEM model is only used for validation purposes, its intended application is of no importance for this work.

The modelled machine has three phases, five pole-pairs, surface mounted magnets, twelve teeth and concentrated windings. Each tooth has a single coil wound around it, which consists of five turns. One phase consists of four series-connected coils, leading to a total of twenty turns per phase. The implemented model is presented in Figure 4.1 together with the coil arrangement, where “-“ index indicates that positive current is entering into the paper. The coils are arranged so that the flux travels in a closed loop through only one of the neighboring coils, where the neighboring coil is also part of the same phase. This coil arrangement gives a maximal self-inductance with minimal mutual coupling between the phases. The advantage of this arrangement lies in its ability to minimize the fault current during a complete single-phase short circuit, being the phase impedance maximized due to the maximized self-inductance. It should be stressed that the physical arrangement does not impact the derived analytical model, as the analytical model is more general and does not have a direct dependency on the structure or winding arrangement of the machine. These

aspects only affect the model indirectly, through the values of the machine's parameters.

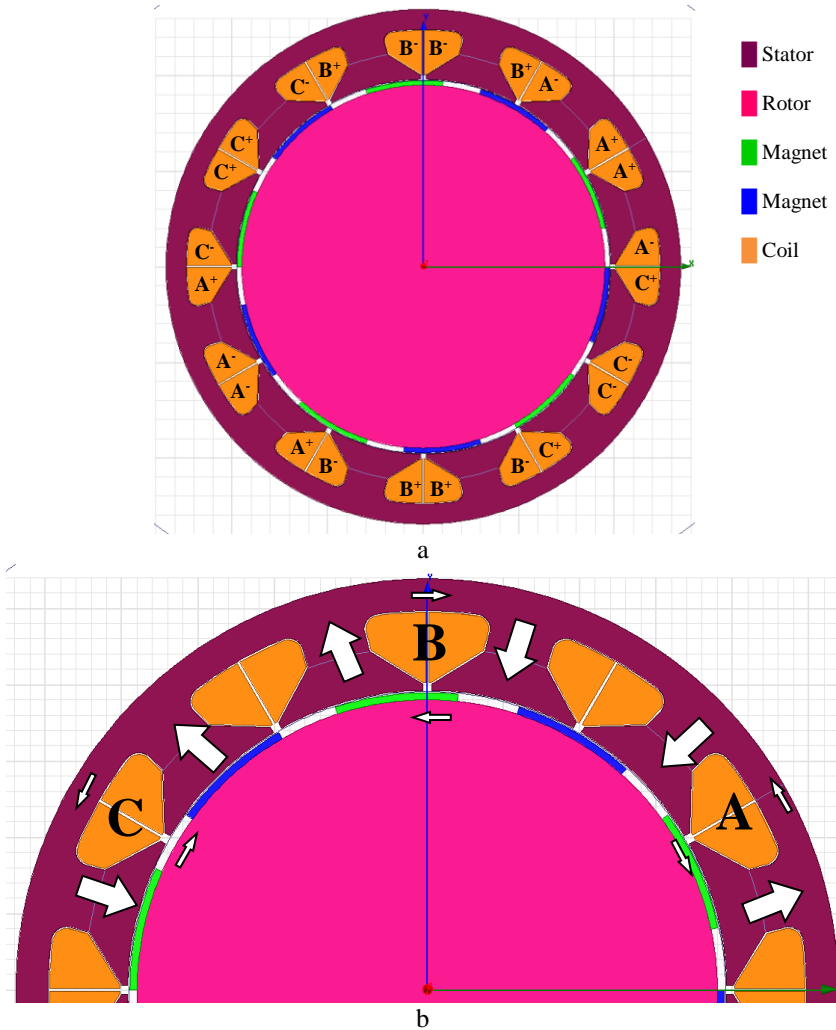


Figure 4.1 FEM model of the machine. Figure a presents the complete machine and the individual winding arrangement of each coil. Figure b presents the flux direction at one time instance.

The stator and rotor material is chosen to be linear iron, the magnet material is neodymium and the coil material is copper. Simulating the FEM model in a magneto-static simulation, the self- and mutual-inductance of each coil can be determined. Through some post-processing of the simulation results the FEM software calculates the total self-inductance and mutual-inductance for each phase using a method similar to the one described in Section 3.2.2.

Figure 4.2 presents the calculated values of the phase inductances using a reluctance grid, where both the simplified rectangular shape for each reluctance segment described in Section 3.2.2 and the more accurate method described in [33] are used. The calculated values are compared with the results from the FEM simulation; the results are normalized with respect to the self-inductance from the FEM model. The numerical values of the machine parameters are presented in Appendix B. The analytical method agrees well for the self-inductance, especially when using the more accurate model. For the mutual coupling the different methods have a larger spread in the results. However, it should be stressed once more that this machine has a very low mutual coupling due to its coil arrangement. Therefore, the difference in absolute values between the different methods is small since the actual value is small. It can also be seen that the more accurate reluctance method's results are closer the FEM results compared to the simple model. However, the simple method provides a good first estimation of the inductance value, also when considering the accuracy of the input data required.

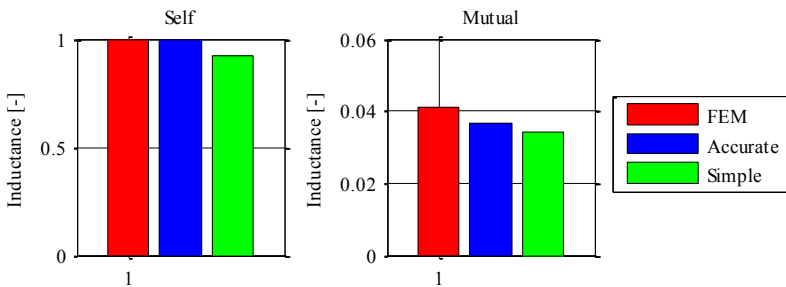


Figure 4.2 Comparison of inductance values for the healthy machine using different method of acquiring the values. The results are normalized with respect to the self-inductance from the FEM model.

Using the FEM model it is possible to determine the inductance dependency on rotor position. Figure 4.3 presents the normalized inductance value with respect to the electrical position of the rotor. As can be noticed from the figure, the inductances can be considered constant with respect to the rotor position, as it can be expected for machines with surface mounted magnets (the permeability of the magnets is comparable to the permeability of the air).

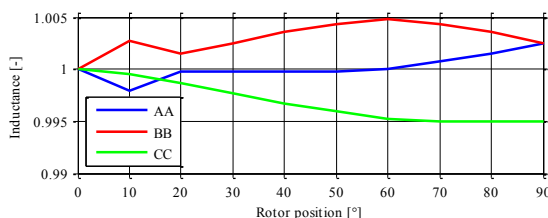


Figure 4.3 The normalized self-inductance from the FEM model as a function of the electrical rotor position for the different phases.

4.1.1 Back-EMF of the non-faulted FEM model

In the analytical model, the back-EMF represented the voltage induced in the stator coils by the alternation of the permanent magnet flux, where the alteration is caused by the mechanical movement of the magnets. In the FEM software, the voltage induced in the stator coils is calculated through the integration of the flux through the coil. A short-coming of the FEM software is its inability to distinguish the origin flux. As a result, in order to acquire the voltage solely induced by the permanent magnet flux, the stator currents need to be forced to zero during the FEM simulation. Figure 4.4 shows the FEM-calculated back-EMF for the three phases normalized with the peak value of phase a ; the FEM model is simulated to rotate at 1500 rpm while forcing the stator current to zero.

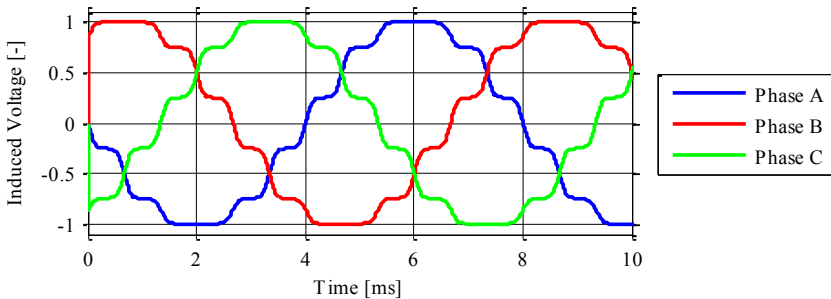


Figure 4.4 FEM calculated back-EMF for the three phases. The machine operates at 1500 rpm while all stator currents are forced to zero.

Because of the realistic design of the modeled machines, the back-EMF is not a pure sinusoidal waveform. By a Fourier analysis of the back-EMF waveform, the exact harmonic content is retrieved. Figure 4.5 presents the harmonic content of the back-EMF, normalized with respect to the fundamental, where the fundamental frequency is equal to the machine's electrical speed. The harmonics are selected to be presented as multiples of the fundamental component rather than in their respective frequency, in order to make the harmonic components independent of the machine's operational speed.

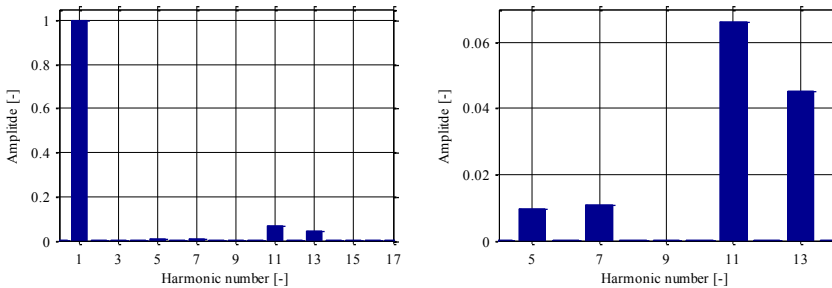


Figure 4.5 Fourier analysis of back-EMF where the amplitude normalized with respect to the fundamental frequency. The left figure presents the first 17 harmonics. The right figure presents a zoomed in version which only presents the largest harmonics.

The result of the Fourier analysis can be implemented in the analytical model of the non-faulted machine, thus the back-EMF vector of the analytical model is given by

$$\mathbf{e}_{abc} = -\omega_r \Psi_{pm} \begin{bmatrix} \sum_{i=1}^{\infty} \sin(A_{H,i} \theta_r + \varphi_{a,i}) \\ \sum_{i=1}^{\infty} \sin\left(A_{H,i} \theta_r + \varphi_{b,i} - i \frac{2\pi}{3}\right) \\ \sum_{i=1}^{\infty} \sin\left(A_{H,i} \theta_r + \varphi_{c,i} + i \frac{2\pi}{3}\right) \end{bmatrix} \quad (4.1)$$

where $A_{H,i}$ is the relative amplitude of the i^{th} harmonic and φ_i is the phase shift of i^{th} harmonic.

To be able to visualize how the turn-to-turn fault impacts the back-EMF, the build-up of the phase back-EMF for the non-faulted machine is presented. Here, the phase back-EMF is the resulting sum of the induced voltage of the four series connected coils. Since the modeled machine has one coil wound around each stator teeth, the phase shift of the fundamental component between each coil can be calculated using (3.30). For the modeled machine, the electrical distance between two teeth for the fundamental component is

$$\varphi = \frac{p n 360^\circ}{\sum c} = \frac{5 \cdot 1 \cdot 360^\circ}{12} = 150^\circ \quad (4.2)$$

Figure 4.6 presents the fundamental electrical distance of all teeth with respect to tooth A_1 , both in total and effective degrees.

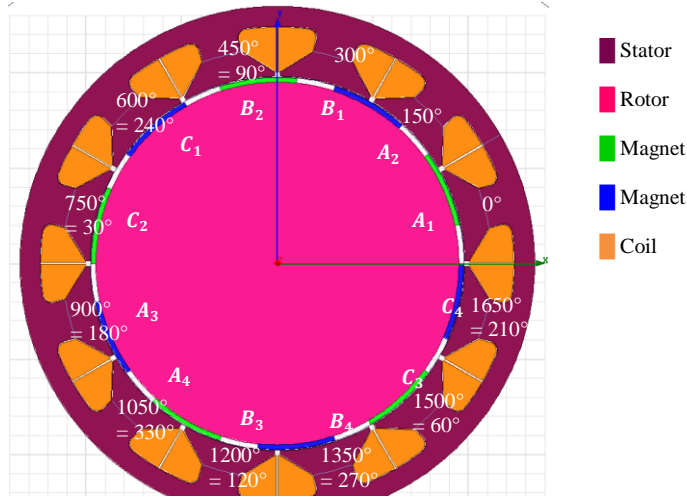


Figure 4.6 The electrical distance off all teeth with respect to tooth A_1 , both in total and effective amount of degrees.

However, as discussed in Section 3.2.3, the electrical distance as well as the winding direction must be taken into consideration when calculating the electrical distance. As can be seen in Figure 4.1a, coils A_2 and A_3 are wound in opposite direction compared to A_1 , resulting in a flux that has a direction from the stator towards the rotor for A_1 for a positive current, and in opposite direction for A_2 . Because this winding arrangement introduces an additional electrical distance of 180° , the total fundamental component of the back-EMF for phase a is

$$E_{af} = |A_1|\angle 0^\circ + |A_2|\angle (150 + 180)^\circ + |A_3|\angle (180 + 180)^\circ + |A_4|\angle 330^\circ \quad (4.3)$$

The amplitude of the fundamental component of the induced voltage in each coil is identical, since the shape of all the teeth and the number of turns are identical for all coils. If the peak amplitude of the fundamental component of the induced voltage in a single turn is referred to as E_1 , then

$$|A_1| = |A_2| = |A_3| = |A_4| = 5E_1 \quad (4.4)$$

The fundamental component of the back-EMF of a single phase for the modeled machine is then

$$E_{af} = 2 \cdot 5 E_1 \angle 0^\circ + 2 \cdot 5 E_1 \angle -30^\circ \approx 19.32 E_1 \angle -15^\circ \quad (4.5)$$

With regards to the harmonics, the electrical distance increases with the harmonic number, i.e. for the fifth harmonic the electrical distance between coils should be multiplied with five. By considering this aspect during the machine design, the amplitude of selected harmonics can thus be reduced by the choice of the electrical distance between the coils. As an example, the fifth harmonic for the modeled

machine is reduced since the electrical distance between coils is -30° , which for the fifth harmonic becomes -150° and (as presented in Figure 3.5) this has a great impact on the resulting amplitude.

4.2 FEM model with turn-to-turn fault

As mentioned earlier, the FEM model of the faulted machine is a modified version of the non-faulted model presented in the previous section; in particular, the faulted modeled has an additional coil in order to emulate the short-circuited loop caused by the turn-to-turn fault. The new coil shares space with one of the existing coils as illustrated in Figure 4.7. Although not visible in the figure, there is a thin layer of air surrounding the extra coil, to provide a galvanic separation between the faulted coils and the affected coil. This insulating layer is added in order have a more realistic representation, as the insulation of the wire in the short-circuited loop is assumed to still be intact (except for the single point were the short-circuit has occurred).

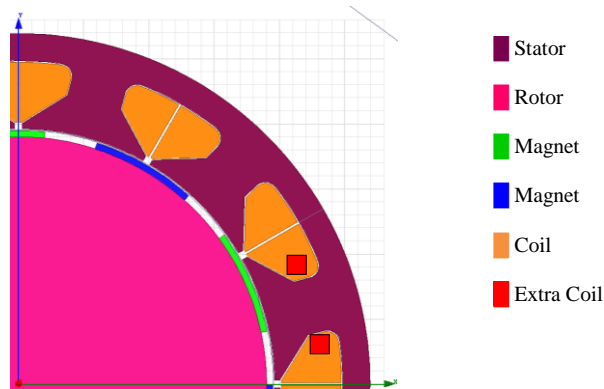


Figure 4.7 FEM model of a PMSM with an additional coil to represent the turn-to-turn fault.

The added coil used to model the turn-to-turn fault will further be referred to as “faulted coil”.

The maximum number of turns that the faulty coil can consist of is limited to the number of turns in the non-faulted coil, as the faulty coil is simply a representation of short-circuited turns. For the machine modeled in this section, the number of turns in a non-faulted coil is five; as a result, the number of short-circuited turns can be selected arbitrary between one and five. For example, if an entire coil is short circuited then, the affected phase consists of three non-faulted coils plus the faulted coil. If only one turn is short-circuited, instead, the affected phase will consist of three non-faulted coils plus a coil constituted by four turns and the faulty coil constituted of a single turn. Since a turn-to-turn fault does not alter the geometry or remove any turns, it can be said that a turn-to-turn fault does not change the number of turns in the affected phase, it only alters how the turns are internally connected.

The orientation of the faulty coil is selected to be in the same direction as the non-faulted coil, in order to preserve the current orientation. It should be stressed that the current in the faulty coil in the FEM model is not the current referred to as i_f in analytical model, but rather the current i_2 in Figure 3.6b. The current in the faulted coil of the FEM model can be acquired from the analytical model through the relation $i_a - i_f$.

The simulated back-EMF of the faulty machine obtained from the FEM model is presented in Figure 4.8, where the phase currents are forced to zero (including the fault current), as for the non-faulted model. In the simulations, the faulty coil is selected to be constituted by a single turn only. For the analytical model, this results in that the term σ becomes

$$\sigma = \frac{N_2}{N_a} = \frac{1}{20} = 0.05 = 5\% \quad (4.6)$$

i.e. 5% of the winding is short-circuited.

Because of the fault, the induced voltage in phase a is reduced as compared with the non-faulted case (as phase a is now only constituted by 19 turns), while the voltages in phase b and c are remain unchanged. Depending on the machine design, the induced voltage in the affected phase can be phase shifted as compared to the non-faulted case, where the phase shift is introduced by the electrical distance between coils. For the modeled machine, the fundamental component of back-EMF for phase a is (where the coil with the turn-to-turn faults is used as reference),

$$E = 4E_1\angle 0^\circ + 5E_1\angle(150 + 180)^\circ + 5E_1\angle(180 + 180)^\circ + 5E_1\angle 330^\circ \\ \approx 18.35E_1\angle -15.8^\circ \quad (4.7)$$

which is -0.8° phase shifted compared to the non-faulted machine, see (4.5). The amplitude of the fundamental component of the phase voltage, relative to the non-faulted case, is

$$\frac{18.35E_1}{19.32E_1} = 0.9498 \approx 0.95 = 1 - \sigma \quad (4.8)$$

This small amplitude difference, together with the small phase shift makes the back-EMF of the faulty machine unbalanced, which coincides with the analysis of the analytical model.

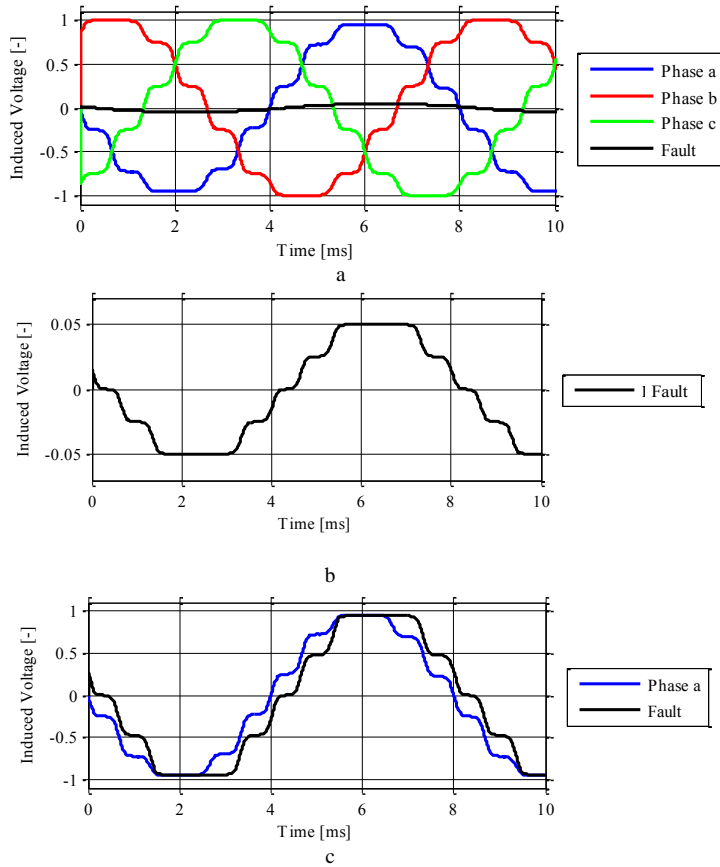


Figure 4.8 FEM calculated back-EMF. Figure a presents the induced voltage in the three phases and the faulty coil normalized with respect the peak value of a non-faulted phase. Figure b presents the induced voltage in the faulty coil only and figure c presents the induced voltage of the faulty coil and phase *a* where the values of the faulty coil is scaled to match that of phase *a*.

Because the faulty coil is selected to be constituted by a single turn (located at the reference tooth) the back-EMF in the faulty coil is

$$E_f = E_1 \angle 0^\circ \quad (4.9)$$

i.e. the part of the back-EMF removed from the non-faulted machine model described by (4.3) compared with the faulted machine model described by (4.7).

The inductance values of the faulty machine are calculated using the same method as for the non-faulted model. The reluctance grid can be used also for this condition. Figure 4.9 presents the two reluctance grid methods and the results from the FEM

software, normalized with respect to the FEM result of the mutual coupling between the faulty coil and the affected phase.

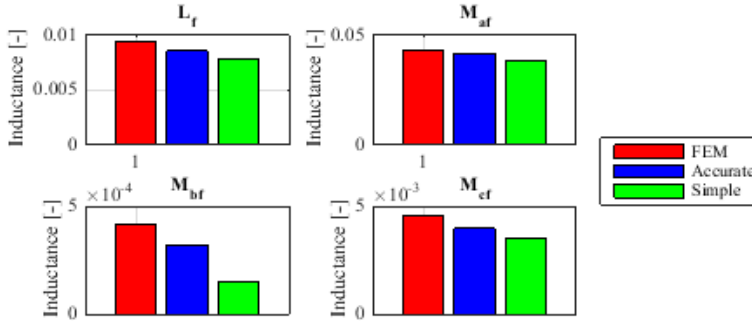


Figure 4.9 Comparison of the different methods for calculating the self-inductance of the faulty coil and the mutual coupling between the faulty coil and the other phases. Note the different scales in the figures, but all models are normalized with respect to self-inductance value of the non-faulted machine.

The analytical methods show less agreement with the FEM results compared with the non-faulted machine (see Figure 4.2). The comparative values for M_{bf} is greatly different and for M_{cf} the results also shows low agreement. However, due to the concentrated winding design used in this machine, the mutual coupling between phases is comparably small during non-faulted conditions, it is therefore only natural that the coupling between the faulted coil and the other phases very small. By comparing the absolute difference between the methods rather than the relative difference, it is possible to observe that the mismatch when using the different methods is small. In the FEM modeled used to acquire the inductance values, the fault is located at coil A_1 (see Figure 4.6) where the neighboring coils are A_2 and C_4 . Hence the amount of flux produced by the faulted coil that reaches a coil belonging to phase b is much less than that of a coil belonging to phase c . As a result, the mutual coupling between the fault and phase b is the smallest (close to being non-existing).

In the FEM model, the faulted coil is implemented as a fourth phase. This creates issues when trying to simulate the model for other operating conditions than the non-load. A limitation of the FEM software is its inability to have allow internal connections between phases, it only allows for pre-selected current or voltage excitation. The galvanic connection between the faulted coil and the affected phase (which included the fault resistance R_f) can therefore not be implemented by the FEM software alone. In order to overcome this limitation and to represent the model depicted in Figure 3.6b, the FEM software is coupled to the circuit simulator Ansoft Simplorer [35]. Through the use of the co-simulation setup, it is possible to correctly interconnect the FEM model's phases to achieve a more realistic simulation. Figure 4.10 presents the co-simulation setup, where the faulted FEM model is set to operate as a generator loaded with a pure resistive load of 1Ω ; the model is externally excited to rotate at a constant speed of 1500 rpm. Due to the adopted implementation of the

coils of the FEM model, the FEM software is unable to account for the winding resistance R_s ; for this reason, these resistances have been added externally, as it can be noticed in the figure.

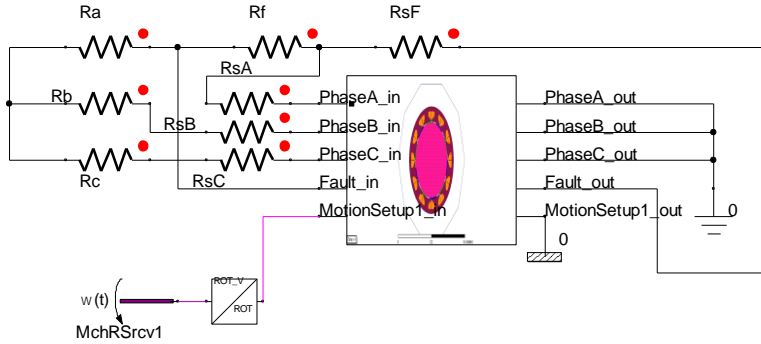


Figure 4.10 Coupling between Ansoft Simplorer and Ansoft Maxwell in order to create the correct connections between the coils.

The simulated currents for the faulty machine when R_f is set to $20\text{ m}\Omega$ are shown in Figure 4.11, normalized with respect to the peak value of the non-faulted phase current.

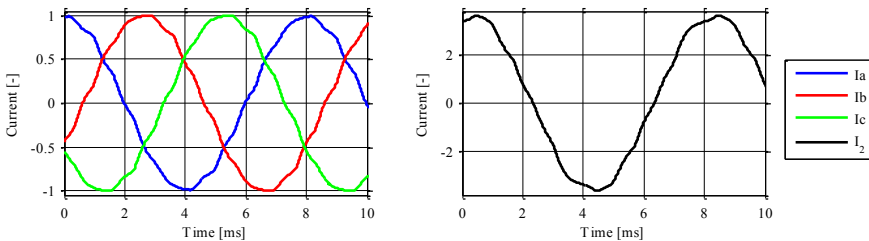


Figure 4.11 Co-simulation between Ansoft Simplorer and Ansoft Maxwell in order to create more accurate connections of the coils.

For this operation point, the peak current in the faulty coil is almost four times the peak current in the other phases, resulting in almost 16 times higher resistive losses, where all the additional losses produce heat locally. The extra heat will likely lead to further winding failure and/or other types of faults, as described in Section 2.4. However, even though this comparatively large current has a non-negligible local impact on the machine, the impact on the phase current is very small, as seen in Figure 4.11.

4.3 Impact of non-linear materials

The FEM model described in the previous sections used iron with a linear B-H curve for the stator and rotor material. To evaluate the impact that non-linear materials have

on the fault and the model, the FEM model presented in Section 4.2 is modified to utilize a non-linear rotor and stator material. The selected non-linear material is M19-29G steel, and its B-H curve is presented in Figure 4.12. The B-H curve can be estimated to consist of two regions, defined by their slope. The impact of the non-linear property depends on the operation point of the machine. From the FEM model with the non-linear material operating as a generator loaded with a pure resistance of 1Ω , it has been found that the peak flux level inside one of the stator teeth is 1.38 T, which is on the top of the knee point of the stator material.

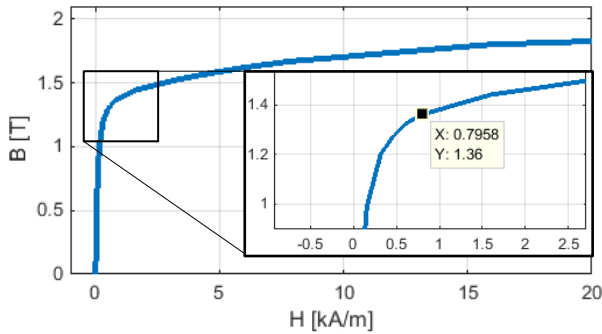


Figure 4.12 B-H curve of the non-linear material used in the non-linear FEM model.

As a result, the machine operates in the most non-linear region of the BH-curve, i.e. in the border region between the linear and saturated operation. By comparing the obtained simulation results of the non-linear FEM model and the linear analytical model, it is found that the models still show good agreement for the fundamental component, with minor differences in the harmonic range, mainly due to the local saturation in the edges of the stator teeth. The simulated currents for the linear and non-linear model are presented in Figure 4.13.

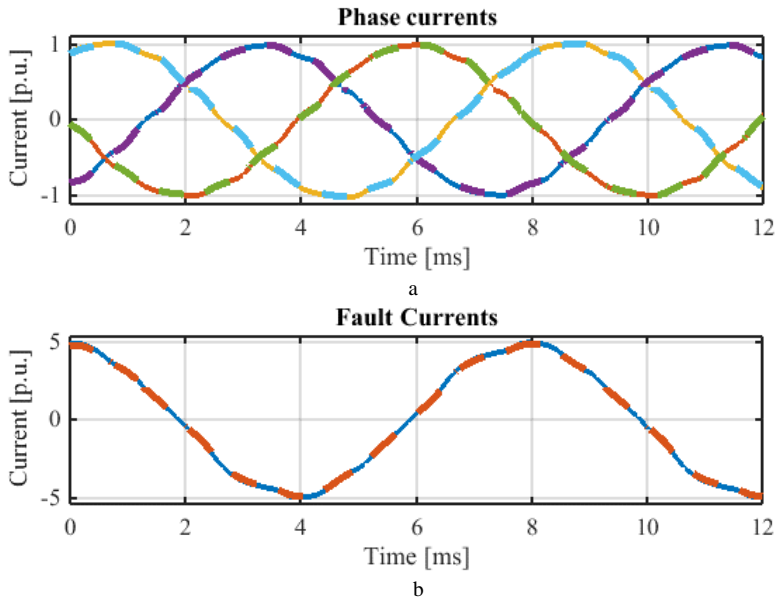


Figure 4.13 Comparison between linear analytical model and non-linear FEM. The dashed lines are from the FEM model. Figure a presents the three phase currents and figure b the faulty current.

Table 4.1 presents the five largest harmonics in the current flowing in the affected phase, where the values are normalized with respect to the fundamental current component obtained from the analytical model.

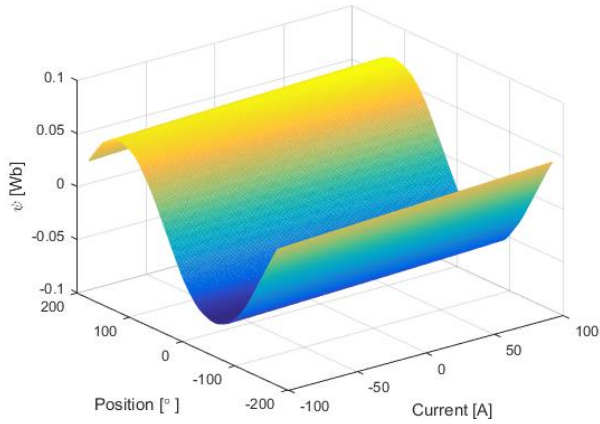
Table 4.1 Amplitude of current harmonics with respect to the to the fundamental

Harmonic number	Analytical	Lin. FEM	Non. Fem
1 (fundamental)	1	0.9904	0.9739
5	0.00394	0.00413	0.00625
7	0.00849	0.00706	0.00315
11	0.02430	0.0210	0.02001
13	0.01411	0.01214	0.01144
23	0.00212	0.00172	0.00166

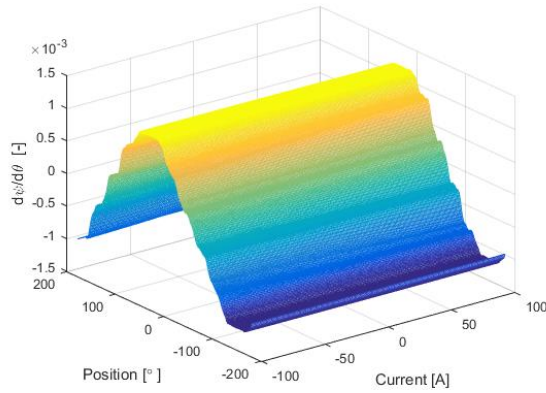
Although a larger deviation between the analytical model and the FEM model using non-linear material is expected (mainly due to the fact that the system inductances or the back-EMF are not constant for the latter) it is important to stress that the two

models still show a very good agreement. Regardless the fact that the fault current in this simulation is about five times larger than the phase current, the machine does not magnetically saturate due to the fault. This is due to the inherent property of the current induced in the turn-to-turn fault loop, which opposes to any change in flux. Therefore, if a linear analytical model shows satisfactory agreement with a non-linear model during non-faulted operation of the machine, then the same analytical model of a machine with a turn-to-turn fault will present similar agreement, as additional saturation is not introduced by the fault. If the machine is designed to operate well into the saturated region during normal operation and a linear analytical model is unable to represent the machine during normal operation, then the presented model will most likely not be able to accurately model the fault current. As a result, the actual fault current is likely to be larger than the current acquired from the analytical model, due to the effect of the saturation. In such case, or in general when there is a need for an analytical model that can accurately represent the behaviour of the machine for all operating conditions (including the saturation region), FEM should be used to create look-up tables describing the total machine's flux with respect to current levels and rotor position. This can be done through a range of simulations where the rotor's position and current levels are altered. Thus, the accuracy of the analytical model depends on the resolution of the sweep and the number of cross-coupling terms taken into consideration. It is however important to stress that sweeping the model for all position and current combinations is heavily time consuming and that in practice it might be more convenient to directly use the FEM model

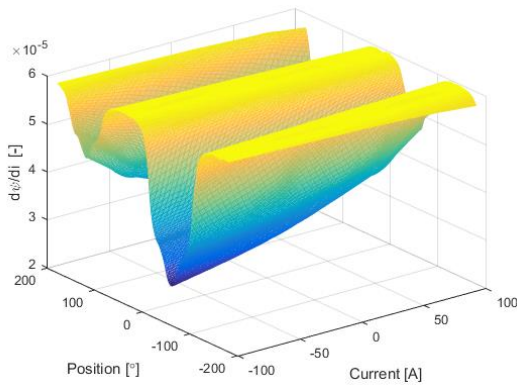
As demonstration of creating look up tables in order to model saturated machines, a crude sweep of the FEM model is performed on an unaffected phase. The sweep resolution was increased through post-processing using a cubic interpolation between the acquired FEM values using Matlab. Inherent from the modeled machine's design, the mutual inductance is negligible compared to the self-inductance. Thus, in order reduce the complexity of the model, the cross-coupling of other phase currents are neglected in the sweep. The result of the simulation sweep is presented in Figure 4.14 which shows that the flux linkage Ψ is dependent on both current and position, which is not considered in the linear analytical model.



a



b



c

Figure 4.14 Flux linkage for a non-faulty phase of the non-linear model. Figure a presents the total flux linkage of the phase and figure b and c presents the partial derivatives of the flux linkage with respect to the position and current, respectively.

For a machine with a different design, where both the mutual coupling between phases as well as the impact of fault current needs to be considered, the number of simulations needed in order to acquire the look-up tables may be considerable. Though possible, this may not be a practical solution and the option of using a FEM model directly may be more efficient.

4.4 FEM model with parallel windings

The machine model with parallel windings used in this thesis is based on the model presented in [36]. The selected model is larger compared with the previously presented model as it is intended application is as an indirect-drive wind power generator. The rating of the larger model is 5 MW with a line-to-line voltage of 4.5 kV. The machine has three phases, where each phase is constituted by four parallel branches organized in a distributed double-layer winding configuration. The coils are distributed in a stator consisting of 72 slots, giving each branch the equivalent of six full slots. As a result, each branch is constituted of six series-connected coils. However, due to the double-layer configuration where two coils share one slot, one branch winding is present in ten slots. Figure 4.15 presents the FEM model and the winding arrangement of one branch (of the four) of phase A. For this model, each coil consists of seven turns, resulting in a total of 42 turns per branch. The rotor has eight surface mounted magnets, i.e. the modeled machine has four pole-pairs and the designed maximum speed is 750 rpm. Further details model details are given in [36]. As can be seen in Figure 4.15, the winding arrangement for the larger machine is selected so that the parallel branches are spatially distributed where each branch utilizes one fourth of the stator. Inherent from this design, the inductance matrix for the analytical model will be sparse as the mutual couplings of the windings is mainly between neighboring branches.

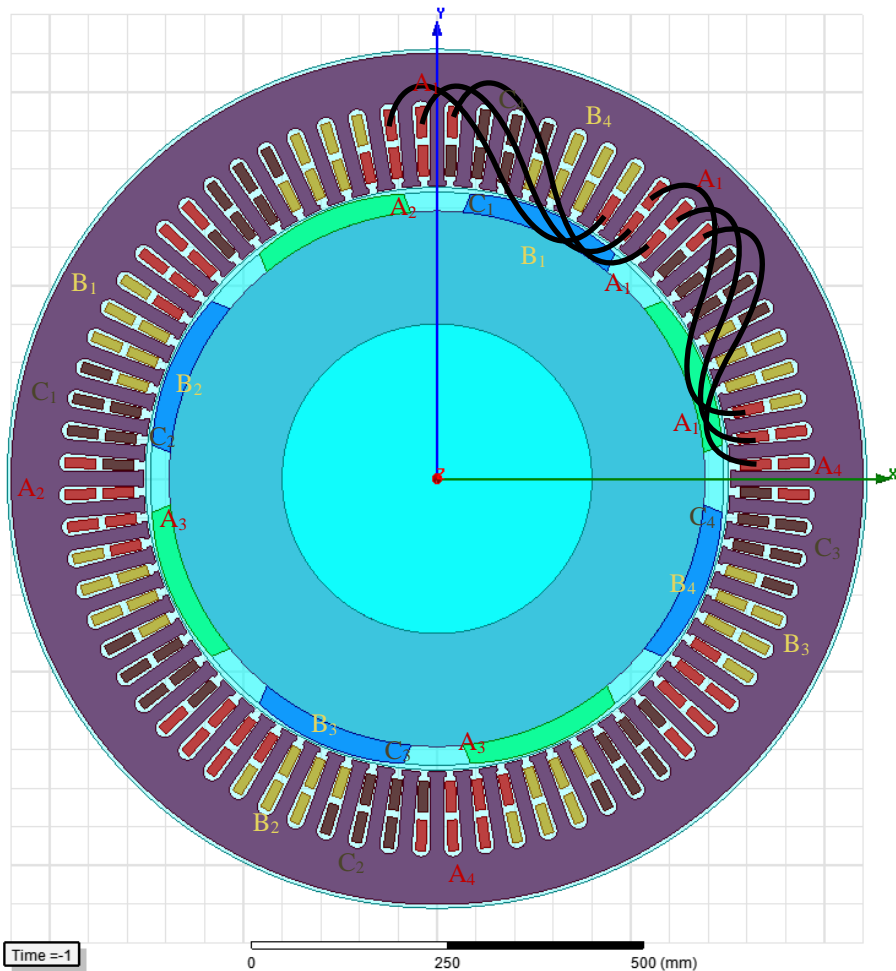


Figure 4.15 FEM model of a machine with parallel windings. The color of the coils is determined by its associated phase.

Because the machine is design with distributed windings the total harmonic disorder (THD) of the back-EMF is lower compared to the smaller machine. Due to the larger number of winding turns, the machine inductance is relatively also larger than for the smaller machine. As a result, the resulting THD of the branch and phase currents is close to zero. Figure 4.16 presents simulated the phase and branch currents of the larger non-faulted machine, where the current has been normalized with respect to the peak value of a branch current. The model is simulated using a co-simulation setup in order to achieve more accurate internal connections as described in a previous section. Similar conditions as for the simulation of the smaller machine was used; generator operation loaded with pure resistive load of 1Ω . Since the model of the larger machine is perfectly symmetrical, the branch current provides and equal

contribution to the phase current, which is the reason to why there appears to be only three currents in Figure 4.16b. Hence, there is no circulating current during non-faulted operation for the model of the large machine.

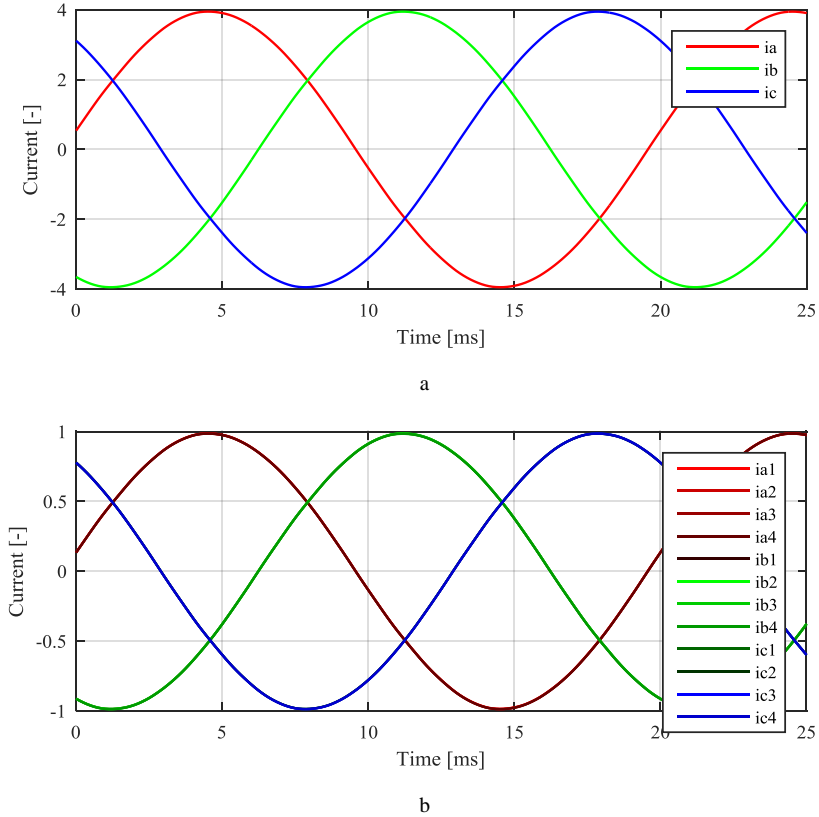


Figure 4.16 Currents of the larger machine model. Figure a presents the phase current and figure b presents the branch currents. The branch currents have close to identical values making it appear as though there is only one branch current for each phase, although all twelve branch currents are presented.

To introduce a turn-to-turn fault in the large machine, an additional coil is added to the model as was done to the small model in Section 4.2. The faulted coil is added to branch A1, see Figure 4.17. As for the smaller machine, the number of turns in the faulted coil can be arbitrarily selected between zero and the available number turns in the non-faulted coil (seven for the larger machine).

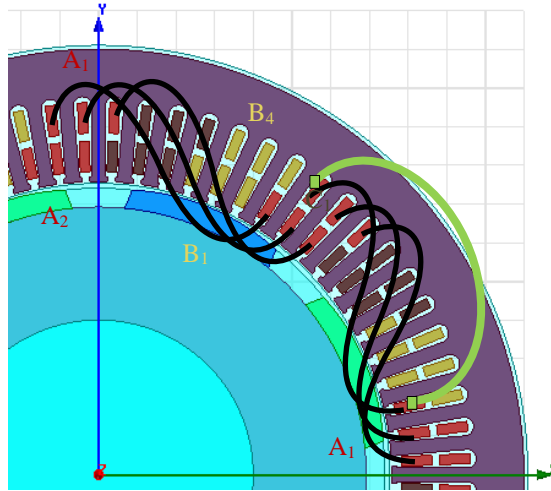


Figure 4.17 The FEM model with the added fault coil, presented in green.

The simulation results using the faulted model of the larger machine are presented in Section 5.5.

4.5 Chapter summary

This chapter presented FEM models of both a non-faulted PMSM and a PMSM with a turn-to-turn fault. The fault was introduced to the FEM model by the addition of a fourth phase consisting of a single coil, where the number of turns in that coil can be arbitrarily selected between zero and the number of turns in a non-faulted phase. In order to overcome the limitations of the FEM software, the model of the faulted machine is simulated in a co-simulation with a circuit software in order to create the more realistic connections between the faulted coil and the affected phase. It was shown that the fault does not introduce additional saturation, hence if a linear analytical model presents acceptable results with a non-linear FEM model during non-faulted operation, then models of the faulty machines will present comparable agreement. A second, larger FEM model with parallel windings was introduced. Due to the perfect symmetry of the larger machine model no circulating currents are introduced during normal operation.

The following chapter presents and compares the simulation results of the analytical models and the FEM models for various operational conditions.

Chapter 5

Model validation and simulation results

This chapter presents the comparison between the analytical and FEM models for both the non-faulted and faulted machine, with focus on the faulted case. The faulted machine models are compared during various operational conditions. In the case of PMSM machine with parallel windings, the fault's impact on the circulating currents is considered.

5.1 Comparison between analytical and FEM Models

A non-faulted three phase machine is analytically modeled according to (3.9); the values of the different machine's parameter values together with the waveform of the back-EMF are extracted from the corresponding FEM model. For the analytical model, the back-EMF is modeled to linearly increase with the electrical speed of the machine. To verify the validity of this assumption, both for the fundamental component and in the harmonic range, the FEM model is simulated when the machine is operated in no-load conditions (open-circuit mode) at different speeds: two times, half, quarter and at one eighth of the nominal speed. The obtained results are presented in Figure 5.1, normalized with respect to the fundamental component at nominal speed. As expected, since the FEM model considers linear material for the iron, the amplitude of both the fundamental and the harmonic components of the back-EMF is linearly dependent on the electrical speed of the machine.

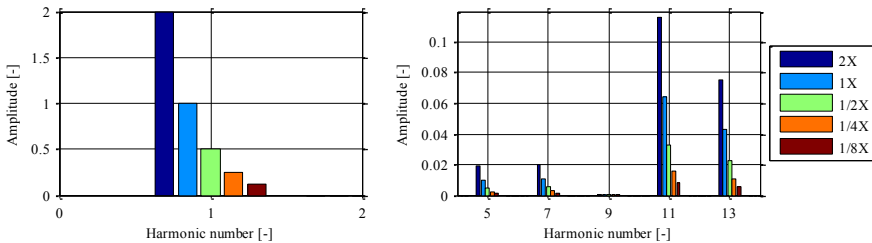


Figure 5.1 Amplitude of FEM back-EMF at various speeds, normalized with respect to the fundamental component at nominal speed.

To verify that both the analytical and the FEM model presents comparable currents during normal operation, they have been simulated under identical operating conditions: generator operation with a pure resistive load of 1Ω . The input power is supplied from an ideal mechanical power source that governs the machine speed. The resulting simulated currents from the two models are presented in Figure 5.2 while the difference between the two models is presented in Figure 5.2b. As it can be observed, there is a very small difference between the models, due to the fact that not all harmonic components of the back-EMF have been included in the analytical

model. The harmonic selection criteria is that the amplitude of the specific harmonic needs to have an amplitude larger than 2% of the fundamental component. As a result, the highest-order harmonic that has been included in the analytical model is the 25th harmonic; higher-order harmonics, which present a small amplitude, have been neglected in the analytical model.

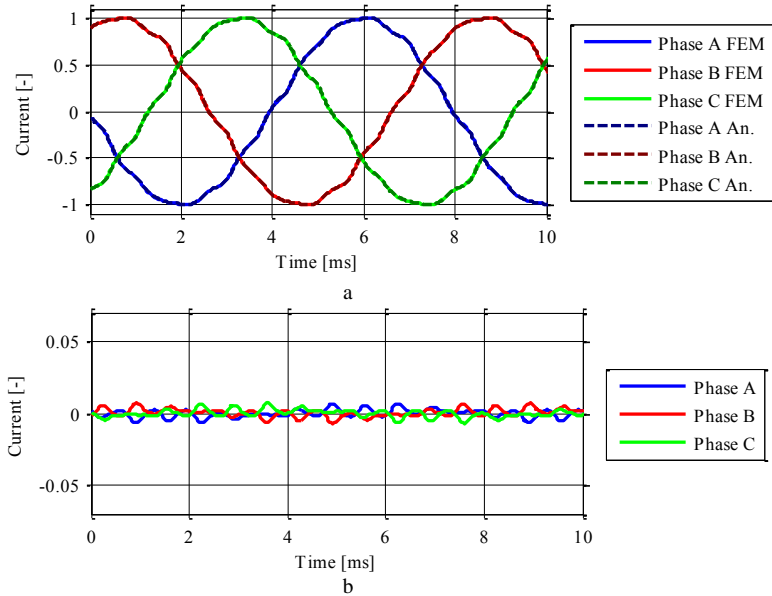


Figure 5.2 Comparison of simulation results from the FEM and the analytical model with added back-EMF components. Figure a presents both simulation results and figure b presents the difference between the two models. Both are normalized with respect the fundamental component.

As can be seen, the analytical model achieves a satisfactory agreement with the FEM model. To verify that the analytical model and the FEM model presents comparable results not only under steady-state operation, the models are simulated under dynamic conditions, where the machine speed is varied. Figure 5.3a presents the obtained simulated current response during acceleration of the machine. Only the current flowing in one phase of the machine is shown for clarity of the figure. The machine starts accelerating at 5 ms, and at 15 ms the machine speed has reached twice the original speed. Note that the speed increase considered for this set of simulations does not represent a realistic scenario, but merely present an illustrative example aiming at model validation. Figure 5.3b instead presents the simulated current response when a speed step is applied (machine's speed doubled after the step). Both figures are normalized with respect to the maximum current amplitude at maximum speed. As it can be seen from the presented results, very good agreement between the FEM and the analytical model is obtained also during dynamic conditions of the machine.

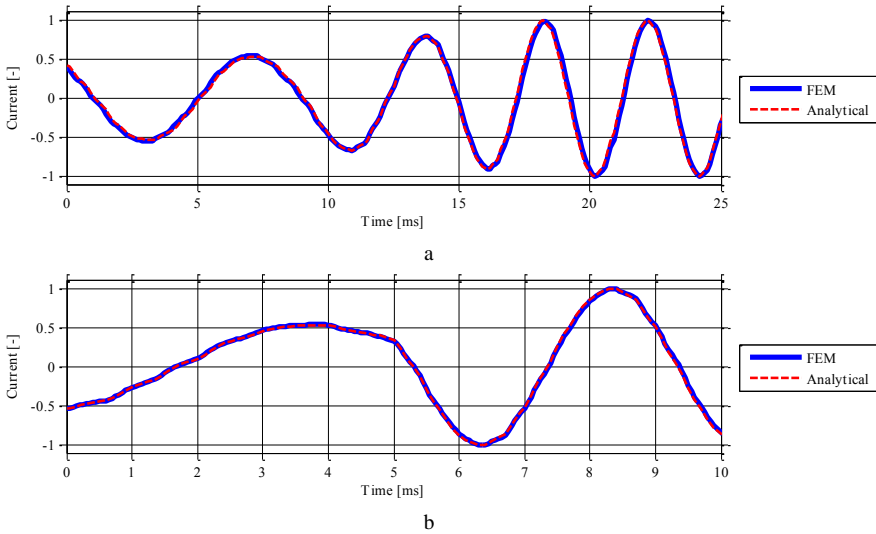


Figure 5.3 Simulation results for one phase from both the analytical model and the FEM model during simulations where the speed is varied. Figure a shows the results during a ramp increase of the speed, where figure b presents a step increase of the speed.

In order to verify that the analytical model and the FEM model also agree for various external loadings, the external resistance connected at the machine terminals is varied. Figure 5.4 presents the obtained simulation results when the load resistance is increased while the machine speed is kept at the nominal value. The results are normalized with respect to when the load is 1Ω , as used in the previous simulations. As can be seen, the two models present a good agreement also under these conditions.

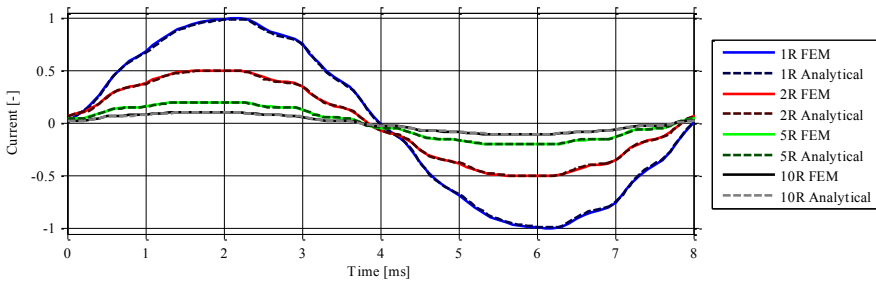


Figure 5.4 Simulation results from both the analytical model and the FEM model for various external loadings.

The same verification procedure is utilized for the faulted machine model. The machine parameter values and the back-EMF waveform are extracted from the FEM model and implemented in the analytical model. Figure 5.5a presents the simulation results for the analytical model of faulted machine together with the results from the corresponding FEM model. The faulted machine is arbitrarily selected to have one

out of the twenty turns short circuited and it is simulated when operating at nominal speed, loaded with a the pure restive load of 1Ω as in previous simulations. Figure 5.5b presents the difference between the two models. All results are normalized to with respect to non-faulted machine case.

The analytical model and the FEM model of the faulted machine show a satisfactory agreement with a comparable mismatch between models as for the non-faulted case. The error is (as for the non-faulted models) caused by the approximation in the harmonic content in the back-EMF in the analytical model. Since the analytical model and the FEM model of the faulty machine provides comparable results, it motivates the use of the analytical model in place of the FEM model for analysis, as the computational time required for the analytical model is greatly reduced as compared to FEM models.

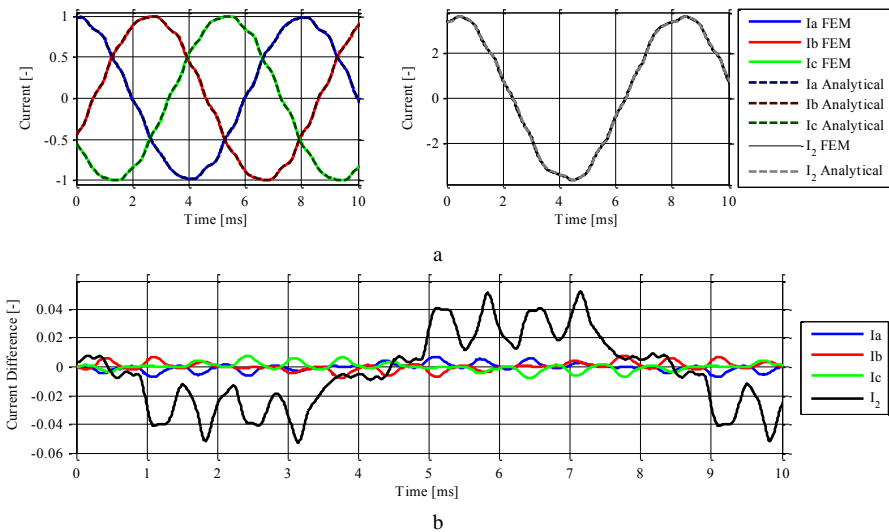


Figure 5.5 Comparison of simulation results from the FEM and the analytical model with added back-EMF components. Figure a presents simulation results from both analytical FEM models and figure b presents the difference between the two models. Both are normalized with respect to the fundamental component of a non-faulted phase.

In order to further increase the level of the details of the implemented analytical model, so that it can be applicable in system level simulations where the fault's impact on other components can be studied, the machine torque of the faulted model needs to be accurately modeled, as it will be shown in the following section.

5.2 Comparison of machine torque between FEM and analytical model

Since FEM models suffers from the classical dilemma of computational time versus accuracy, where a few seconds of simulation time can result in weeks of computation time, it is not practical to use this kind of analysis tools for larger system simulations. For this kind of simulations, the less computationally demanding analytical model is more suitable. It is therefore of importance to verify that the analytical model of the faulted machine presents comparable results with the FEM model with respect of both currents and torque for under all possible operational conditions. So far, the implemented model only considered the electrical properties of the machine, where the speed is treated as an input to the state-space model. To further develop the model, a mechanical model of the PMSM can be implemented. Here, a one-mass representation of the mechanical drive train is added to the model. In order to show the validity of the implemented model both during steady-state conditions and in case of variations in the applied mechanical torque, an ideal voltage-source converter has been connected to the machine's terminals. The converter is used as a mean to control the torque of the machine, in order to extend the operational applications of the model from those of a generator with pure resistive loading. In the case of the analytical model, to add a converter controller is a simple procedure. However, this is less trivial when dealing with FEM, as the software used in this thesis does not have a function that allows a direct implementation of the control algorithm. Therefore, a third software, which is capable of implementing the control system, needs to be incorporated into the previously used co-simulation between the FEM and the circuitual software.

In this thesis, the adopted third software is Matlab Simulink, which has already been adapted for simulating the analytical model. In the co-simulation, Simplorer acts as the main software, which provides the coupling between the different the simulation tools. The implemented controller utilizes a cascade design, where the inner loop consists of a vector current controller while the outer loop is a torque controller, as the one described in [31]. The inputs to the vector current controller, other than the current references, are the machine speed and the machine currents, where the currents are extracted from the FEM model. The speed is retrieved from the model of the mechanical drive train, which is incorporated in the Simulink model. The inputs to the mechanical model are the torque acquired from the FEM model and an additional mechanical torque source modeled internally in the Simulink environment. The mechanical torque source is ideal and unlimited and it is used to control the speed of the machine. Due to the ideal nature of the mechanical torque source, it is able to produce any desired machine speed regardless of the machine torque. The machine speed from the mechanical model in Simulink is thus used as an input to the FEM model. The output from the controller are the reference values for the converters voltage modulator, and since this thesis assumes an ideal converter, the reference values equals the voltage applied to the machine terminals. Figure 5.6 presents a schematic view of the information trade of the co-simulation. As in the case of the

previously presented FEM simulation, Simplorer is used to achieve realistic connections between the phases of FEM model and the faulted coil.

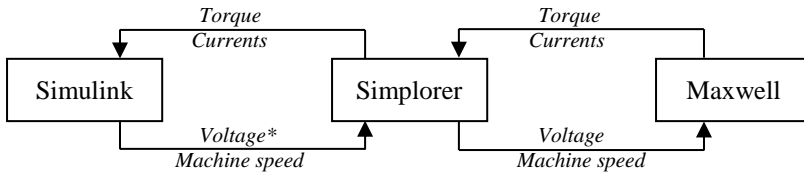


Figure 5.6 A schematic view of the information trade of the co-simulation, where the * indicates a reference value.

Using the described co-simulation setup, the FEM model's behavior during converter-controlled operation can be verified. In the simulation, the reference values for the control system are selected so the machines should generate a breaking torque of 100 Nm for 200 ms during which the mechanical power source ensures a linear acceleration of the machine speed. After 200 ms the machine torque reference is stepwise reduced to 30 Nm in order to appreciate the validity of the model during dynamic conditions. In addition, at 200 ms the output of the mechanical torque source is reduced to match the machine's breaking torque of 30 Nm, in order to gain constant-speed operation. The simulated machine speed and torque obtained from the co-simulation is presented in Figure 5.7. The torque of the FEM model shows some torque ripple (as to be expected), which is caused by fluctuation in the air-gap flux due to the geometry of the machine. Further analysis of the machine torque and its ripple is discussed Chapter 6.

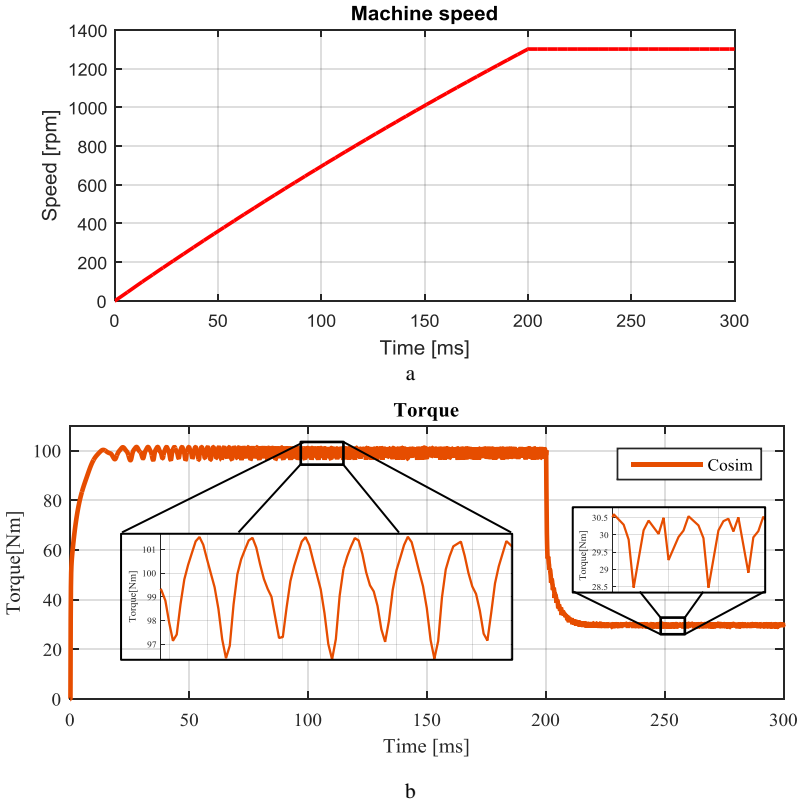


Figure 5.7 Machine speed and torque from the co-simulation.

From a controller perspective, the machine torque can be modeled as [31]

$$T = \frac{m}{2} p \Psi_{pm} i_q \quad (5.1)$$

However, as this representation assumes a constant magnetic flux it is only able to model the average torque. As a result, the instantaneous machine torque, which also includes the torque ripple, cannot be represented (5.1) and therefore may not be sufficient for the investigated applications. A more accurate model of the machine torque can be derived using the analytical model and its electrical representation of the machine's mechanical power, which is acquired through the product of the currents and the corresponding back-EMF, i.e.

$$P_{mech} = e_a i_a + e_b i_b + e_c i_c \quad (5.2)$$

Using (5.2) together with the information of the mechanical speed of the machine, the instantaneous machine torque can be found, which accuracy is mainly determined by the accuracy of the back-EMF representation. However, the analytical model only

incorporates the active interaction between the stator and rotor fluxes; any reluctance/cogging torque inherited from the machine design is therefore not considered. Even though the average value of the cogging torque is zero, it does contribute to the instantaneous value of the machine torque and is therefore contributing to the torque ripple. The cogging torque data for the modeled machine can be extracted from the FEM model, where the data can be implemented in the analytical model. For linear machines, the cogging torque only depends on the rotor position (i.e. independent on the operational condition of the machine), the cogging torque component can be added as an additional component of the model of the mechanical drive train for the analytical model.

The cogging torque data is retrievable from the FEM model when it is simulated with all stator currents forced to zero, i.e. open-circuit operation. The simulated cogging torque for two different machine speeds is presented in Figure 5.8.

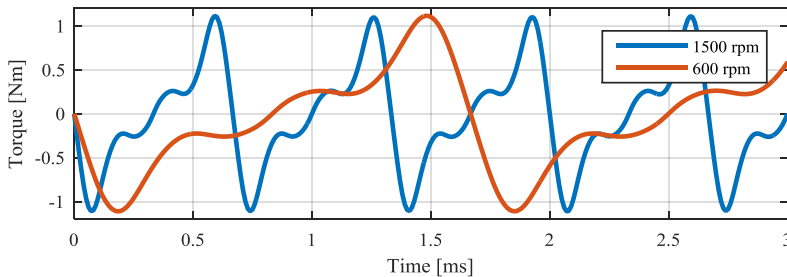


Figure 5.8 Cogging torque retrieved from the FEM model for two different speeds.

The cogging torque for the small machine presents a peak amplitude of $1.1 Nm$, while the peak amplitude of the total torque ripple of the non-faulted machine is about $2.5 Nm$ for a reference torque of $100 Nm$ and $1.35 Nm$ for a reference torque of $30 Nm$, see Figure 5.7b. Hence, for the small machine model the cogging torque cannot be neglected if an accurate representation of the machine is desired. Through a Fourier analysis of the retrieved cogging torque data it is shown that the cogging torque is constituted by 12th-order frequency component and multiples of it, which is to be expected as the stator of the modeled machine has twelve teeth.

Using the more accurate model of the machine's active torque given in (5.2), and with the cogging torque implemented as a position dependent part of the mechanical system, the analytical model is simulated using identical conditions as for the co-simulation. The resulting currents and torque is presented in Figure 5.9, where the speed is identical as in Figure 5.7a.

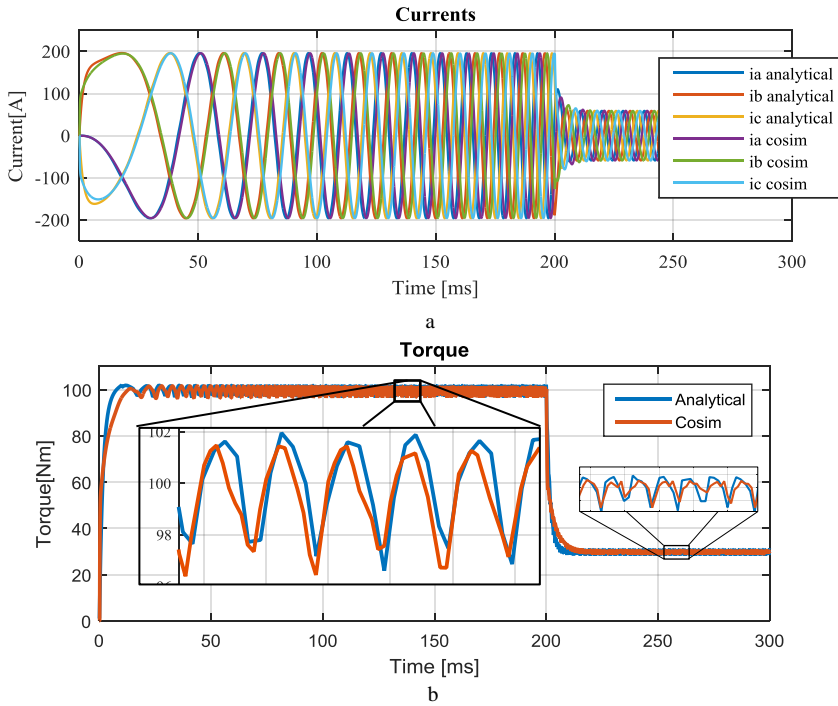


Figure 5.9 Currents and torque from analytical model and the co-simulation for non-faulted machine models.

As shown, due to the inclusion of the cogging torque, good agreement during non-faulted operation has been obtained between the analytical model and the co-simulation. In the case of a turn-to-turn fault, the model of the machine's mechanical power needs to be updated to include impact of the fault. The updated power equation is

$$P_{mech} = e_a i_a + e_b i_b + e_c i_c - e_f i_f \quad (5.3)$$

The impact of the fault on the machine's mechanical power is clearly visible through the term $e_f i_f$ in (5.3). Since the modelled machine is a PMSM, both the induced voltage e_f and the fault current i_f has the same frequency; therefore, the presence of the turn-to-turn fault causes a torque component that oscillates at twice the fundamental frequency. Note that the amplitude of this oscillation with respect to the average torque depends on the output power level and on the severity of the fault. As a result, this oscillation might not be noticeable in the output torque for all operation conditions.

Through the use of (5.3), the torque obtained for the analytical model can be compared with the torque for the faulted FEM model. The models of the faulted

machines are simulated given identical excitation as was used for the non-faulted models. The resulting currents and torque for the faulted machine models are presented in Figure 5.10

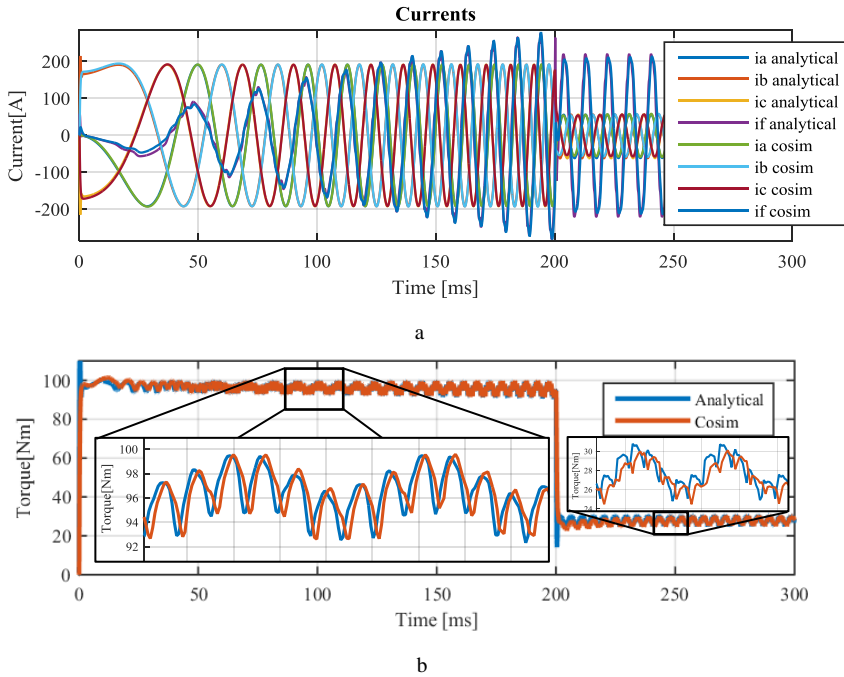


Figure 5.10 Currents and torque from analytical model and the co-simulation for faulted machine.

As can be seen in the figure, the torque oscillation at two times the frequency as predicted by (5.3) is clearly visible. Hence, by using the modelled back-EMF (and its harmonic content) and the current to calculate the machine's mechanical power, the analytical model is able to accurately represent both the inherited torque ripple caused by the machine design as well as the torque ripple introduced by the fault. For the modeled machine, the ripple component introduced by the fault has a larger amplitude compared to the components which are also present for the non-faulted machine, i.e. the ripple component introduced by the fault may cause additional stress on the mechanical system to which the machine is connected.

To summarize, the analytical and FEM models of the faulted machine shows very good agreement, both during dynamical and steady-state operation, confirming that the presented analytical model can be used for a wide range of applications. Examples of such applications are the investigate of the faults impact on an system level or to investigate the machine controller reacts for converter controlled machines. However, the goal of this thesis being to develop knowledge to be used for the

development of fault develop detection methods, this will be the main use of the presented models in the following chapters of this thesis.

5.3 Comparison between faulted and non-faulted analytical models loaded with a pure resistive load

In order to develop effective fault detection methods, it is important to identify characteristic (and preferably unique) behaviors of the faulted device that are not present, or clearly visible, during non-faulted operation. For this purpose, the modeled faulted machine is compared with the non-faulted model. The currents of the models are compared while both models are operated in steady-state; using the previously presented setup where the machine is operated as a generator loaded with pure resistive load. The speed of the machine is governed by an external mechanical torque source. The simulated currents from the two model and the difference between them are presented in Figure 5.11, where the currents are normalized with respect to the peak value of one of the non-faulted phases. One turn (5% of the winding) is selected to be short-circuited for the faulted machine model.

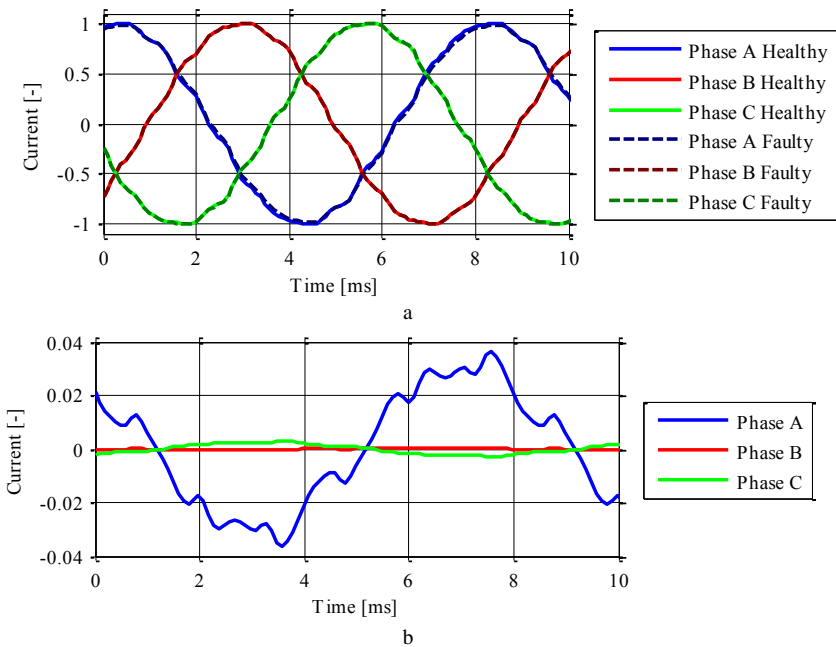


Figure 5.11 Normalized phase currents from the non-faulted and faulted machine models. Figure a presents the three phase currents of both models and figure b present the difference between the two models.

The current from the two models are very similar, but not identical; as it was easy to expect, the largest difference between the models is for the affected phase (in this simulation phase *a*). However, unless a track record of the phase currents is kept for all operation points, this small difference is likely not detectable. The method of

comparison presented here can therefore not be utilized as an online indication method that a fault has occurred. An additional general drawback of the comparison method is that it can only present an indication that a difference exists, as the method typically is unable to provide information regarding the cause of the difference.

For a PMSM with a turn-to-turn fault, both the stator circuit and the back-EMF become unbalanced, as discussed in Section 3.3, and the severity of the introduced unbalance depends on the number of short-circuited turns. The fundamental component of the back-EMF for the affected phase becomes reduced and a small phase shift may also be introduced depending on the machine design. Similarly, the fault affects the harmonic components, as discussed in Section 4.1.1. In the event of a fault, the cancelling effect of the harmonics caused by the electrical distance between coils may be reduced, resulting in an increased amplitude of the harmonic. This motivates the possibility that both the fundamental and the harmonic content of the machine currents should be considered when identifying characteristics of the faulted machine.

Figure 5.12 presents the frequency spectra of the current in phase *a* depicted in Figure 5.11 for both the non-faulted and the faulted model. The results are normalized with respect to the fundamental component of the non-faulted model. Observe that the two models present minor amplitude differences, where all components are reduced except for the 7th, i.e. the canceling effect of the 7th harmonic is reduced in the event of a turn-to-turn fault for this machine design.

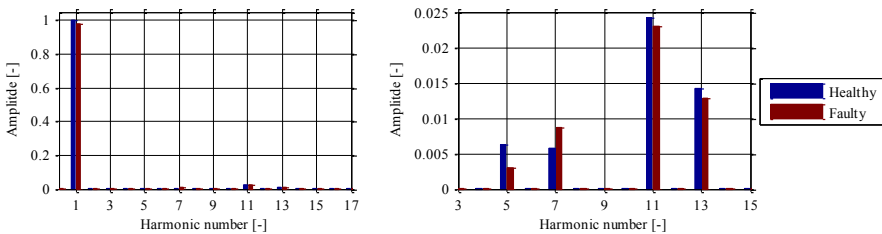


Figure 5.12 Normalized harmonics in the current of phase *a* from both the non-faulted and faulted machine models

Since the fault only impacts the already existing harmonics in the stationary reference frame, and considering that the harmonic variation is very small, it may prove difficult to use the amplitude of the harmonics directly as a fault indication method. As an alternative, it is possible to monitor the frequency content of the stator current in the rotating reference frame, since the transformation of the currents can introduce additional frequency components as shown by the model derived in Section 3.4. The currents of both the non-faulted and the faulted model are therefore transformed into the rotating reference frame. The results from the Fourier analysis of the transformed currents are presented in Figure 5.13 where Figure 5.13a is normalized with respect to the non-faulted model's respective fundamental component. Figure 5.13b presents the absolute values to show that the *d*- and *q*-components are affected equally by the

fault, which is to be expected from the model of the faulted machine in the rotating reference frame presented in (3.64).

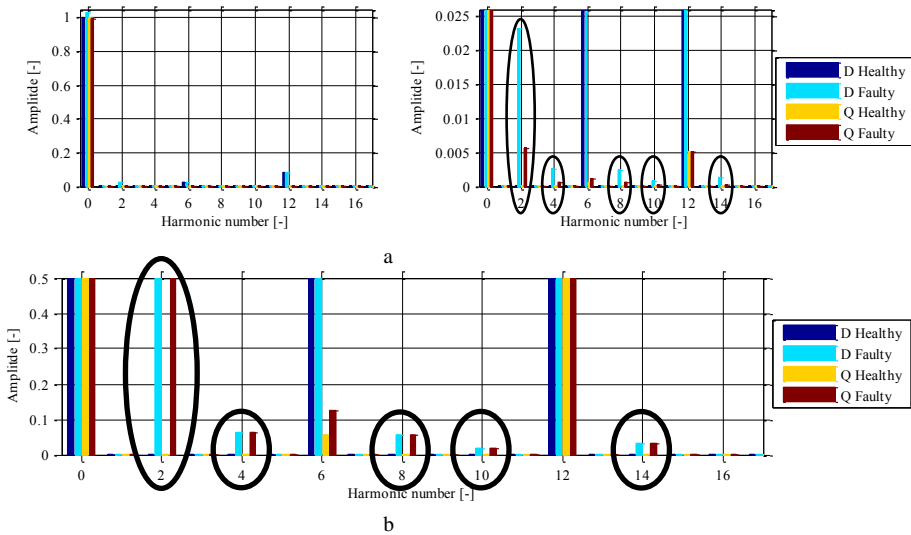


Figure 5.13 The harmonics content of the currents in the rotating reference frame from both the non-faulted and faulted machine models. Figure a presents the normalized currents, figure b presents the non-normalized information which shows that d - and q -components are affected equally.

As in the stationary reference frame, the amplitude of the harmonics in the rotating reference frame becomes altered in the event of a turn-to-turn fault. However, a more apparent difference between the two reference frames is the introduction of new harmonic components, where the appearance of the second harmonic is the most noticeable due to its large amplitude. The introduction of the second harmonic is to be expected in the event of a turn-to-turn fault, since the fault will effectively change the machine from a balanced to an unbalanced system, as in (3.64). As can be seen in Figure 5.13, the fault introduces more than the second harmonic. For example, the fourth and eighth harmonic are also introduced, although their amplitudes are smaller than the amplitude of the second harmonic. These harmonics originate from the harmonics of the back-EMF, but only becomes visible after the fault. The unbalance introduced by the fault causes the harmonics in the rotating reference frame to split-up and appear as additional frequency components. For example, the fourth harmonic in the rotating reference frame originates from the fifth harmonic in the stationary reference frame. As an example, the transformation of the d -component for the fifth harmonic is

$$\begin{aligned}
& \frac{2}{3} \left[\cos \theta \quad \cos \left(\theta - \frac{2\pi}{3} \right) \quad \cos \left(\theta + \frac{2\pi}{3} \right) \right] \begin{bmatrix} A_{H,5}^* \cos(5\theta + \alpha) \\ A_{H,5} \cos \left(5 \left(\theta - \frac{2\pi}{3} \right) \right) \\ A_{H,5} \cos \left(5 \left(\theta + \frac{2\pi}{3} \right) \right) \end{bmatrix} \\
&= \frac{1}{3} \left[A_{H,5}^* \cos(5\theta + \alpha - \theta) + A_{H,5} \cos \left(5\theta + \frac{2\pi}{3} - \left(\theta - \frac{2\pi}{3} \right) \right) \right. \\
&\quad \left. + A_{H,5} \cos \left(5\theta - \frac{2\pi}{3} - \left(\theta + \frac{2\pi}{3} \right) \right) + A_{H,5} \cos(5\theta + \alpha + \theta) \right. \\
&\quad \left. + A_{H,5} \cos \left(5\theta + \frac{2\pi}{3} + \left(\theta - \frac{2\pi}{3} \right) \right) + A_{H,5} \cos \left(5\theta - \frac{2\pi}{3} + \left(\theta + \frac{2\pi}{3} \right) \right) \right] \\
&= \frac{1}{3} \left[A_{H,5}^* \cos(4\theta + \alpha) + A_{H,5} \cos \left(4\theta - \frac{2\pi}{3} \right) + A_{H,5} \cos \left(4\theta + \frac{2\pi}{3} \right) \right. \\
&\quad \left. + A_{H,5}^* \cos(6\theta + \alpha) + A_{H,5} \cos(6\theta) + A_{H,5} \cos(6\theta) \right]
\end{aligned} \tag{5.4}$$

The same procedure can be performed for the q -component and for other harmonics. In the normal (balanced) case, the 5th harmonic typically is symmetrical, meaning that $A_{H,5}^* = A_{H,5}$ and α is zero. Therefore, under these conditions the harmonic term that oscillates with a frequency of four times the machine speed is equal to zero. However, during a turn-to-turn fault α becomes non-zero and $A_{H,5}^*$ is altered as compared with the pre-fault condition (see Figure 5.12), leading to

$$A_{H,5}^* \cos(4\theta + \alpha) + A_{H,5} \cos \left(4\theta - \frac{2\pi}{3} \right) + A_{H,5} \cos \left(4\theta + \frac{2\pi}{3} \right) \neq 0 \tag{5.5}$$

for the faulted machine and thereby the appearance of the fourth harmonic.

In general, this new set of harmonics in the rotating reference frame can be explained using a vector representation (see Appendix A) of a three phase system. A generic unbalanced and distorted three phase voltage vector $\mathbf{e}_k(t)$ in the stationary reference frame can be described as [37]

$$\mathbf{e}_k(t) = \mathbf{e}_{k_p}(t) + \mathbf{e}_{k_n}(t) = E_{k_p} e^{jk(\omega t + \varphi_p)} + E_{k_n} e^{-jk(\omega t + \varphi_p)} \tag{5.6}$$

where ω is the angular frequency of the system. E_{k_p} and E_{k_n} are the amplitudes of positive and negative phase sequence voltage vectors, respectively, φ_p and φ_n are their phase displacements, and k indicates the harmonic number. Observe that in (5.6) the zero sequence component has not been considered. During balanced operation, the negative sequence component for the harmonics 1, 4, 7, ..., is zero. Analogously, for harmonics 2, 5, 8, ..., the positive sequence is zero. By moving (5.6) into the rotating reference frame it can be seen that the harmonic shift in frequency as

$$e^{-j\omega} \mathbf{e}_k(t) = E_{k_p} e^{j(k-1)(\omega t + \varphi_p)} + E_{k_n} e^{-j(k+1)(\omega t + \varphi_p)} \tag{5.7}$$

The positive components are represented at one harmonic order below while the negative sequence are represented at one harmonic order above. Thus, both the fifth and seventh harmonic in the stationary reference will appear as a sixth harmonic in the rotating reference frame during balanced operation. However, as previously described, during an unbalanced condition the fifth harmonic in the stationary reference frame contains both a negative and positive sequence component, which will appear as the fourth and sixth harmonic in the rotating frame.

In essence, through monitoring the harmonic content of the machine currents in the rotating reference frame a turn-to-turn fault can be detected. The harmonics to monitor are the second in combination with a set of specific harmonics which are determined by the harmonic content of the machine's back-EMF in the stationary frame for the non-faulted machine. Note that the amplitude of the fault introduced harmonics have an equal amplitude in both the d - and the q -currents, which is to be expected by an inspection of (3.77) and (3.78). The advantage of this method is that it does not require the knowledge of the amplitude of the monitored quantities for a set of operational conditions, as they should have a zero amplitude for all non-faulted operational conditions. However, because of the small amplitude of the introduced harmonics, a measurable difference may in practice not be visible until a larger portion of the winding is short-circuited.

5.4 Impact of ideal converter on the electrical quantities of the faulted PMSM

In the previous sections, it has been shown that a turn-to-turn fault only has a limited impact on the measurable electrical quantities of the investigated machine. PMSMs are typically driven by power converters; therefore, it is of interest to investigate how the converter control reacts to a faulted machine; in particular, the aim is to study if the presence of the converter allows a more effective fault detection method through the different measurements available. In converter-driven machines, any control-loop structure requires local measurements for proper operation. This information is already available in the system and, together with signals estimates or internal control quantities, can be utilized for detection purposes. In addition, the controller is likely to react on the altered machine response caused by the fault and this will impact the ability to detect a fault condition. The way how the system reacts on the specific fault condition is highly dependent on the machine's time constants, its application and on the implemented control structure.

In this thesis, the implemented control algorithm for the converter is based on a cascade structure, as the one described in [31]. An overview of the control structure is presented in Figure 5.14. The outer-loop controller is a PI-regulated speed controller, which uses the torque-current relation presented in (5.1) in order to calculate the current reference for the inner-current controller. The converter is considered ideal, meaning that the reference voltage output from the current

controller are assumed to be directly applied to the converter terminals, without a modulation stage or system delays, as in the simulations presented in Section 5.2

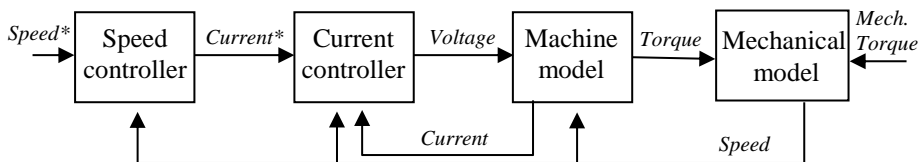
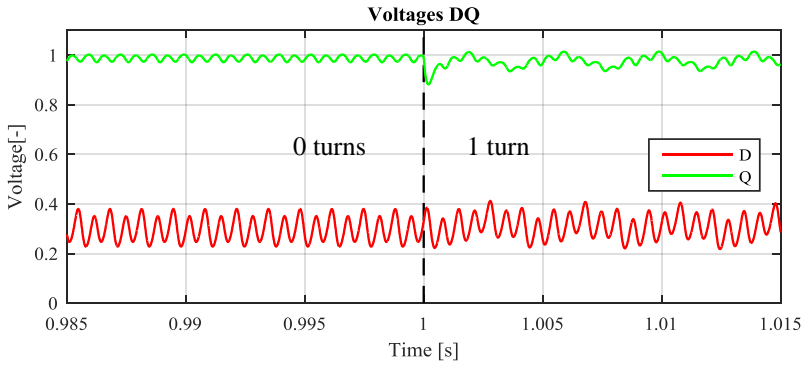


Figure 5.14 System overview, where the * indicates a reference value.

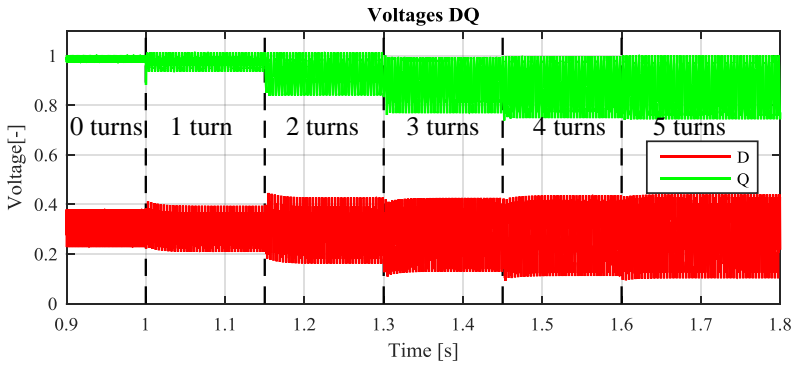
Figure 5.15 presents the steady state voltages output from the control system when the flexible model is simulated to operate as a generator. The values are normalized with respect to the non-faulted value of the Q voltage. The speed reference is set to 1500 rpm and an ideal external mechanical torque is applied to provide a constant power input. During non-faulted operation, the output voltages are close to constant for the selected operating condition. However, once the flexible model transitions into faulted operation, the output voltages visibly change. The voltage ripple increases and an additional frequency component appears, as already observed in the currents when the machine has been loaded with a pure resistive load.

As the machine is current controlled, the voltage ripple introduced is the controllers attempt to counteract the current ripple introduced by the fault; note that the main frequency component in the voltage ripple is at two times the fundamental frequency, which is within the close-loop controller bandwidth. With an increasing number of short-circuited turns the level of unbalance increases, leading to an increasing current ripple and thereby a larger voltage ripple, see Figure 5.15b.

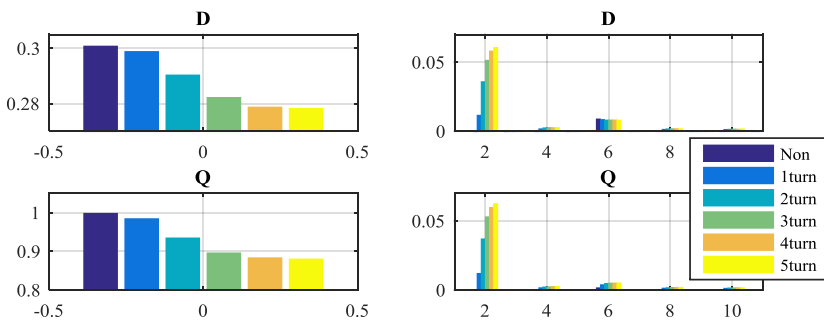
The simulation shows that the controller's output voltage can be monitored to identify the occurrence of a turn-to-turn fault; however, as for the machine current while loaded with a pure resistive load, only monitoring the amplitude of the additional components introduced by the fault can be ineffective, especially in case of low number of short-circuited turns.



a



b

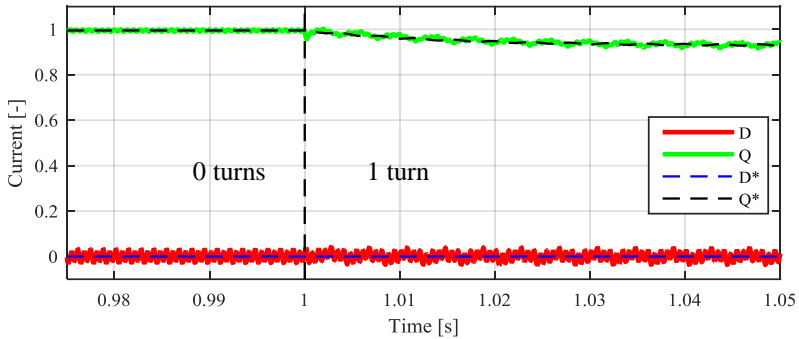


c

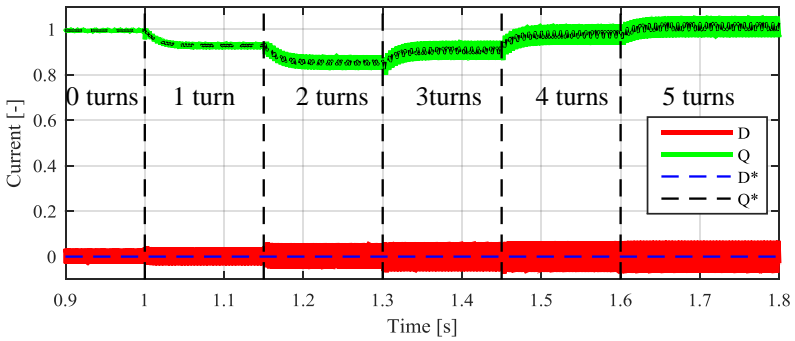
Figure 5.15 DQ-voltages for non-faulted and faulted operation, figure a presents a higher resolution of the non-faulted operation and a single turn fault. Figure b presents how the voltages changes with an increasing number of turns, and figure c presents the results of a FFT analysis of the voltages during different number of short circuited turns.

Figure 5.16 presents both the reference and the actual currents in the rotating reference frame, together with the Fourier analysis of the actual current. The currents are normalized with respect to the non-faulted value of the Q current. Through the comparison of the current and the voltage, it can be seen that the amplitude of the voltage harmonics is larger than the current ones. However, a change in the DC value is clearly visible for the currents; note that this change is also visible in the reference current. Therefore, monitoring only the harmonics may not be the most efficient method to detect the turn-to-turn fault, as the fault has a noticeable impact on the fundamental component as well. However, the advantage of monitoring the harmonics still remains although it can be beneficial to also monitor the DC value.

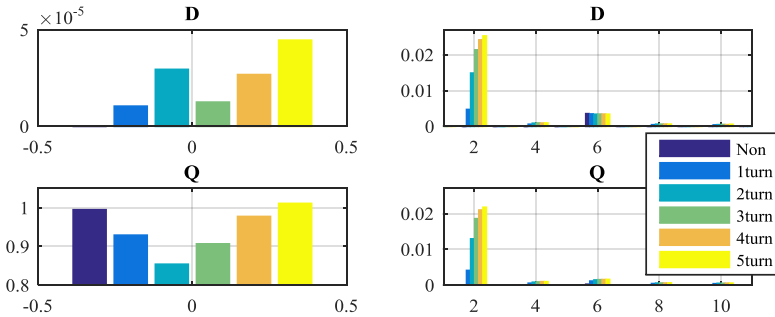
Since both the current and the voltage are affected by a turn-to-turn fault during converter operation, also the electric power will be affected. This can also be seen from the representation of the mechanical power of the faulted machine described by (5.3). Under specific circumstances, the impact of the fault on the power might be more visible than thorough monitoring of the current and voltage individually.



a



b



c

Figure 5.16 DQ currents for non-faulted and faulted operation, figure a presents a higher resolution of the non-faulted operation and a single turn fault. Figure b presents how the current changes with an increasing number of turns, and figure c presents the FFT values of the currents for the different number of turns short circuited.

Figure 5.17 presents the simulated electrical power of the machine. The figure is normalized with respect to the non-faulted value. For the modeled machine, the impact of a single turn fault can clearly be seen in the change of both the DC component as well as in the ripple amplitude. The reduction in the DC value is a

reaction from the speed controller, due to the fact that the machine (which is operated as a generator) is supplied with a constant mechanical power and now has to account for the increased losses due to the fault condition. Obviously, similar considerations hold when the machine is operated as a motor.

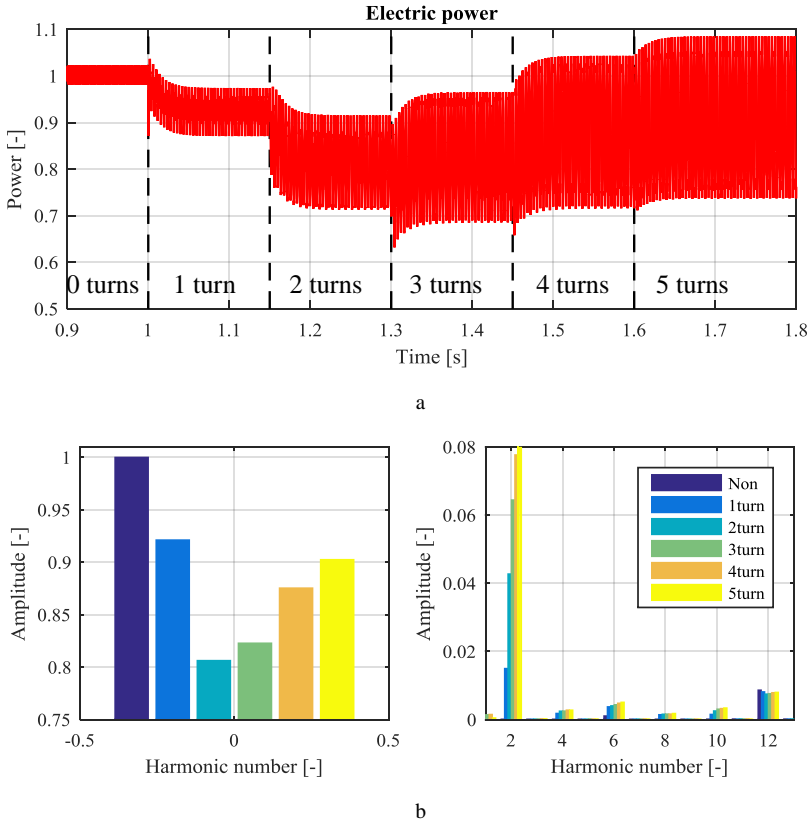


Figure 5.17 The output power of the flexible model during converter driven generator mode. Figure a presents the time values of the normalized power and figure b presents the results of the Fourier analysis of the power for the varying number of short-circuited turns.

The simulations shows that the amplitude of double-frequency ripple increases with the number of short-circuited turns; analogous consideration does not hold for the DC component. This is caused by a decrease of the fault current for the higher number of short-circuited turns. The resistance and the induced voltage in the short-circuited loop can be estimated to increase linearly with number of short-circuited turns while the inductance (and by extension its impedance for a given frequency) can be estimated to increase with the number of short-circuited turns squared. Therefore, for a low value of the fault resistance R_f (i.e. a good contact between short-circuited turns), the inductance of the short-circuited loop can quickly become the dominating impedance, which limits the fault current. However, since the inductive impedance

does not contribute to the active losses of the machine, an increase in the number of short-circuited turns can reduce the losses caused by the fault. As a result, the power output of the machine can increase even if the number of short-circuited turns increases.

In response to the non-symmetrical machine currents, the voltages output of the control system will no longer be symmetrical, i.e. their relative phase shift will not be 120° electrical degrees. Thus, an alternative detection approach can be based on the monitoring of the phase angles of the controller output voltage and machine currents. To track these angles, a single phase Phase-locked loop (PLL) can be used, as the one presented in [38]. The estimated angles output from the single-phase PLLs are compared with the actual electrical position of the rotor, which is here used for the rotating reference frame transformation. Figure 5.18 presents the resulting PLL angles, both reference and simulated values, for the current and the voltage.

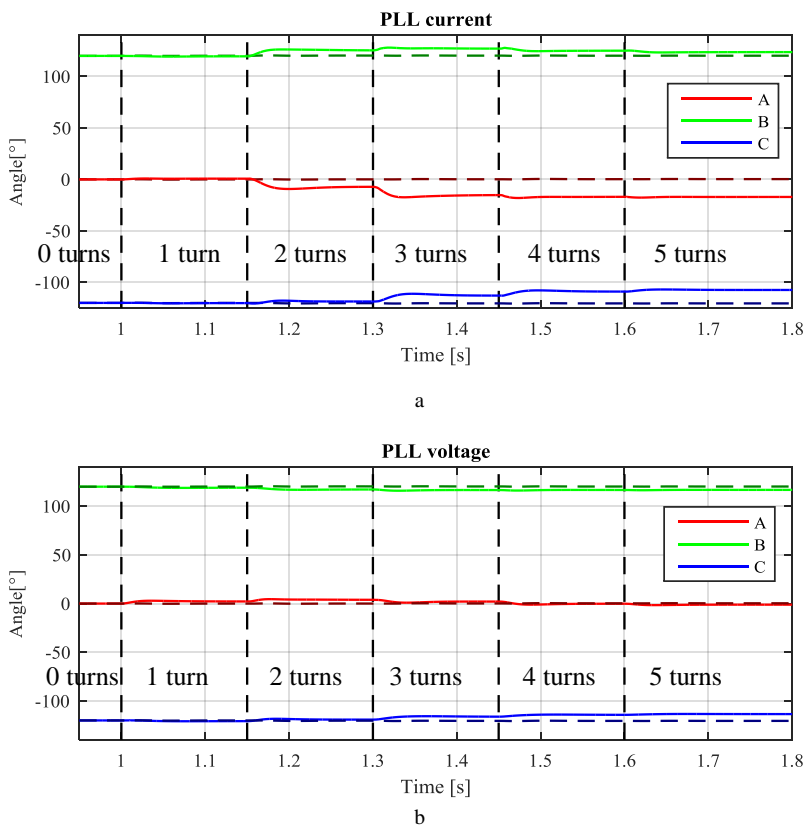


Figure 5.18 PLL estimated angles of the machine current and machine voltage.

The largest shift occurs in the current; however, observe that when only one turn is short-circuited the phase shift introduced by the fault is less than 1° , thus difficult to

detect in practical applications. However, as the fault progresses, leading to an increasing number of short-circuited turns, the shift increases and at two short-circuited turns the largest shift is more than 7° for the currents and about 4° for the voltages. This shift should be sufficiently large to be detectable.

By comparing the different electrical quantities, it is clear that the power is the one that is the most affected by a turn-to-turn fault during converter operation. An additional benefit of using the power as an indication tool is the possibility to acquire a crude estimate of the severity of the fault, as the power difference between expected and actual value is caused by the fault. However, as shown more quantities can be monitored at the same time, increasing the chances to be able to detect a fault condition.

5.5 Parallel windings and circulating currents

The machine model with turn-to-turn fault presented in Section 4.4 is used in this section and it is coupled to the circuit simulator Ansoft Simplorer in order to achieve more realistic connections between branches, as discussed in Section 4.2.

For machines with parallel windings a turn-to-turn fault does, in addition to the fault current, cause circulating currents between the phase branches. As previously stated, the largest circulating current, with respect to the external loading, occurs during open circuit/no load operation. For this operational condition, the voltage difference between the affected branch and the non-faulted ones is the cause of the circulating current and it is limited by the branch impedances. Figure 5.19a presents the simulated branch currents for the affected phase during no-load operation, when one of the 42 turns is short-circuited. Because of the reduction in the induced voltage in the affected branch, the current in that branch is in the opposite direction as compared to the other branches. However, the current is not shared evenly between the non-faulted branches. The current imbalance is caused by the mutual couplings between branches. In addition, because of the mutual coupling between branches, the fault will also induce circulating currents in the non-faulted phases. Depending on the coupling factors, the induced current in a branch of a non-faulted phase can become larger than the current that flows in a non-faulted branch of the affected phase; this is clearly visible in Figure 5.19b, where i_{b1} is larger than i_{a2} . Since the origin of the branch currents in the other phases is the mutual coupling, the induced current is in phase (or 180° out of phase depending on coupling factor) with the affected phase. Hence, if all branch currents are monitored, the turn-to-turn fault can easily be detected during no-load operation: all branch currents are in phase with the affected phase and the branch with the largest current (and opposite sign as compared with the others branches in the same phase) is the faulted branch. As can be seen from Figure 5.19, the simulation shows that for the modeled machine, a single short-circuited turn results in a circulating current that presents an amplitude of about 20% of the rated branch current in the affected branch and between 5% and 10% of the rated branch current in the other non-faulted branches.

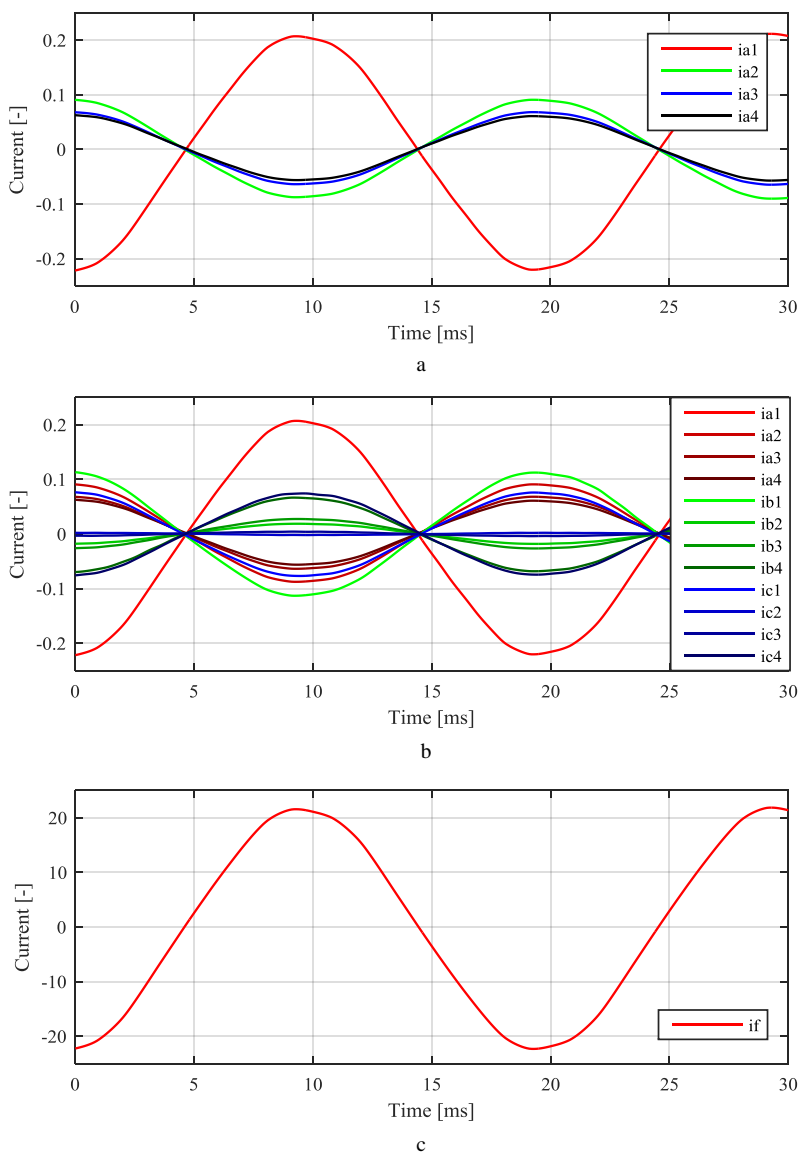
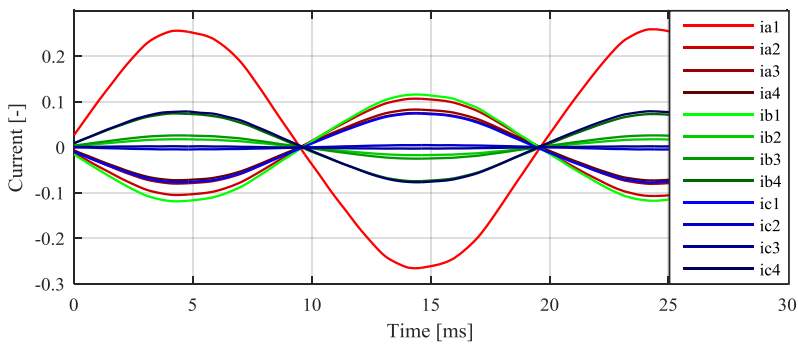


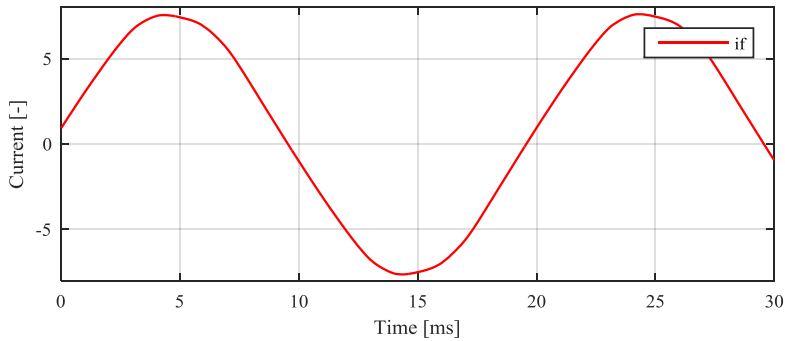
Figure 5.19 Figure a presents the branch currents of the affected phase fault and figure b presents all the branch currents for all phases when one turns is short-circuited. Figure c presents the fault current in the short-circuited loop. All figures are normalized with respect to the peak value of the rated branch current.

If only one turn is short-circuited, the circulating current caused by the fault is small compared to the rated branch current and should therefore not cause any excess stress which the system is not able to cope with. However, as the fault current is many times

greater than the rated current, it is highly probable that additional turns will become short-circuited. Since an increase in the number of short-circuited turns leads to a greater difference in the induced voltages between the branches, it will result in a larger circulating current. However, it is important to keep in mind that the circulating current is not proportional to the number short circuited turns, as the branch impedances is not linearly dependent on the number of short-circuited turns. Figure 5.20 presents the no-load branch currents when three turns are short-circuited. As can be seen, the circulating current increases with the number of short-circuited turns. However, the fault current decreases with the number of short-circuited turns, indicating that the inductance quickly becomes the dominating impedance of the faulted loop.



a

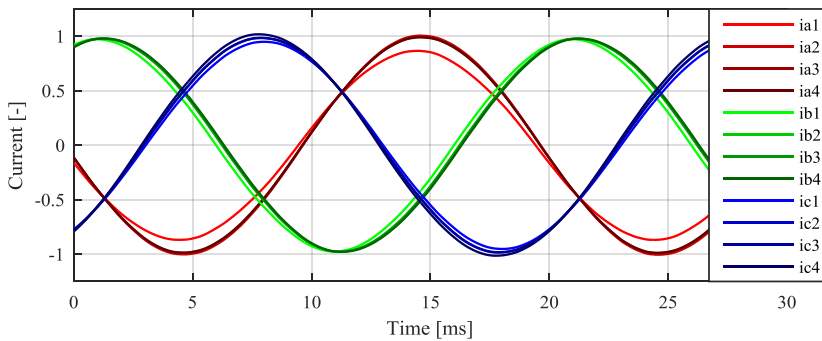


b

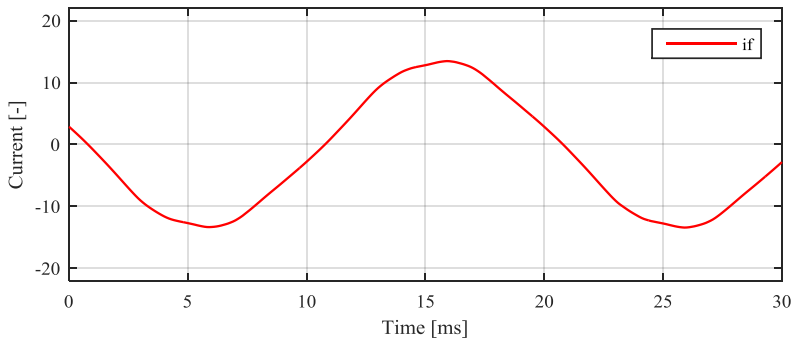
Figure 5.20 Figure a presents all branch current during no-load operation with three short-circuited turns. Figure b presents the fault current in the short-circuited loop

So far, the investigation has been carried out under the assumption that the machine is operated in no-load. For a loaded machine with a turn-to-turn fault (where it is assumed that only a few turns are short-circuited), the resulting voltage difference between the branches is not sufficiently large to cause the affected branch current to

become of opposite sign compared to the other branches of the affected phase. This is because the internal voltage drop of the branches generated by the load current compensates the voltage drop caused by the fault, i.e. the internal voltage drop over the stator impedance is larger than the induced voltage reduction caused by the turn-to-turn fault. Figure 5.21 presents the branch currents when the machine is producing rated power; for this simulation, one turn has been short-circuited. The affected branch still contributes to the load power, even though it provides less than the other branches. As a result, the power outputs from the non-faulted branches of the affected phase are increased in order to compensate for the missing power of the faulted branch, leading to a small over loading of the non-faulted branches.



a



b

Figure 5.21 All branch currents during rated operation and one turn short-circuit in branch a1.

Hence, the power of the affected branch varies with the load (as previously discussed), and it ranges from consuming power during no-load operation to contributing to the load power at rated loading. However, the circulating current can always be seen as the unbalance in the branch currents, and as shown by the no-load case, the circulating currents may also be visible in the non-faulted phases, depending specific design of the machine. Even though the fault current becomes reduced during

generator operation compared to no-load operation (the stator reaction creates a flux which opposes the magnet flux, resulting in a reduction of the induced voltage in the fault loop), it will still be several times larger than the rated current and a continued operation without any form of protective action is therefore not recommended.

If only the three phase load currents are measured and not all branch currents, then it is not possible to measure the circulating currents, and the circulating current can therefore not be used for fault detection purposes. However, as these simulations show, not all branch currents need to be measured: one single measurement is sufficient for detecting a circulating current. Hence, if the current in one of the branches (for each phase) is measured in addition to the total phase current, changes in circulating current can be detected and may be used as an indication that a turn-to-turn fault has occurred.

If it is not possible add additional current sensors, it is still theoretically possible to monitor the current harmonics, as presented in Section 5.3. However, in a PMSM with parallel windings the harmonic content in the back-EMF is likely to be even smaller than the one presented in Section 5.3, see Figure 5.22 which presents the results of the Fourier analysis performed on the load currents in the rotating reference frame for the large generator during rated operation. As can be seen, the amplitude of harmonics are very small, making a detection method based on harmonic variation not feasible in practice.

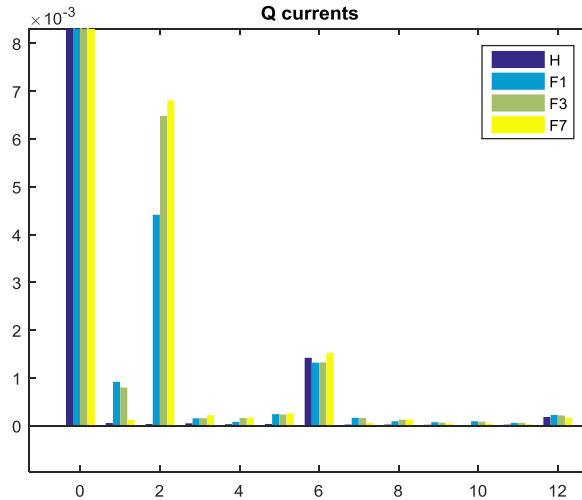


Figure 5.22 Fourier analysis of phase currents for the large generator with parallel windings during rated operation for non-faulted operation and when 1, 3 and 7 turns are short-circuited. The values are normalized with respect to the non-faulted Q-current amplitude.

5.6 Chapter summary

In this chapter, the different analytical models for the PMSM have been verified against FEM. It has been shown that very good agreement has been achieved between the two models, both in terms of the electrical quantities and torque. For the latter, it

has been shown that the cogging torque should be included in the mechanical model as a position dependent component for a correct representation. Using the presented models, it was shown that it can be very difficult to detect a turn-to-turn fault in a selective way by simply using electrical quantities, unless the machine of interest has a parallel winding configuration and there is a possibility to monitor the branch currents. For this reason, the coming chapter presents how the electromagnetic forces in a PMSM become affected in the event of a turn-to-turn fault.

Chapter 6

Electromagnetic forces in a PMSM with turn-to-turn fault

This chapter presents how a turn-to-turn fault affects the electromagnetic forces in the modeled PMSMs. To better understand impact of a fault condition, the forces for both the non-faulted and faulted model are presented and compared.

6.1 Summary of Maxwell stress tensor

The previously presented analytical models can be successfully used to model electrical quantities of the machine. However, as the analytical model is derived to be generic in order to be applicable to any PMSM design, it lacks the means to model the air-gap flux density, as this is heavily dependent on the machine's mechanical design. The air-gap flux density can be used to investigate not only the machine torque, but also the normal force density through the Maxwell stress tensors. The normal force density of the machine can be used to estimate attraction forces between rotor and stator, and the potential vibrations that may occur in the case of a not perfectly symmetrical normal force. Here, since any analytical modeling the mechanical structure of the machine is out of scope for this thesis, the FEM models (which includes the mechanical design of the machine) are used to investigate the fault's impact on the air-gap flux density, and by thereby the electromagnetic forces.

Since the Maxwell stress tensors describe the interaction between electromagnetic forces and mechanical momentum, the aim of this section is to provide an overview of the Maxwell stress tensors and its application. More thorough analysis is available in the literature, for example in [39]. For electrical machines, a simplified versions of the Maxwell stress tensors equations can be used, since the electromagnetic field can be assumed to be purely magnetic the regions where the machine torque is produced; in the air-gap and in the rotor and stator steel. The Maxwell stress tensors can be used to both calculate the machine torque as well as to calculate the attraction forces between the different machine parts. The attraction forces can be used as an input to a mechanical model of the machine frame, in order to estimate the steel deformation of both stator and rotor. Observe that deformation estimations of the machine frame is out of scope for this thesis and for this reason will not be treated in the following.

To further simplify the calculation of the stress tensors, the modeled air-gap flux density is represented using a set of sub-vectors. For a given cross section, a set of two perpendicular vectors can be used: a normal component and a tangential component. For radial flux machines, a natural orientation of the normal component is in the radial direction; this orientation is used in this thesis. Using this reference, the normal force density in the air-gap represents the attraction force between the

rotor and stator steel. The tangential force density is the origin of the machine torque, i.e. it is the force density that provides motion to the machine. The analytical expressions of the normal- and tangential force densities are

$$f_n = \frac{1}{2\mu_0}(B_n^2 - B_t^2) \quad (6.1)$$

$$f_t = \frac{1}{\mu_0}B_nB_t \quad (6.2)$$

where f is force density, B is flux density and indices n and t indicate normal and tangential quantities, respectively. For machines, the total air-gap flux is the sum of the rotor and stator flux, i.e.

$$B_{airgap} = B_{rotor} + B_{stator} \quad (6.3)$$

In order to achieve a rotating motion of the machine rotor, the machine stator winding (which is fixed in space) must be able to generate a flux vector that rotates in space only using a time varying electrical excitations as input. However, the normal component of the air-gap flux for a single spatial point does not rotate: being characterized by a fixed direction and an amplitude that varies with time, it pulsates. Similarly, for a given time instance, the amplitude of the normal component varies with the spatial position within the air-gap. Hence, the normal component of the air-gap flux density is both time dependent and dependent on the spatial position in the air-gap. If it is assumed that the air-gap flux density has a pure sinusoidal shape in both time and space, then the normal component of the flux density can be described as

$$B_n \propto \cos(\omega t - \theta) \quad (6.4)$$

where θ represents the spatial position within the air-gap and ωt represent the time dependence created by the electrically excited rotational field. As an example, a graphical representation of the normal flux density component for a two pole pair machine with a pure sinusoidal air-gap flux density is shown in Figure 6.1. The transformation into the synchronously rotating reference frame is the equivalent of moving diagonally in the figure, in order to keep the amplitude in the z -direction constant, i.e. moving in space with the appropriate speed to synchronize with the time varying field.

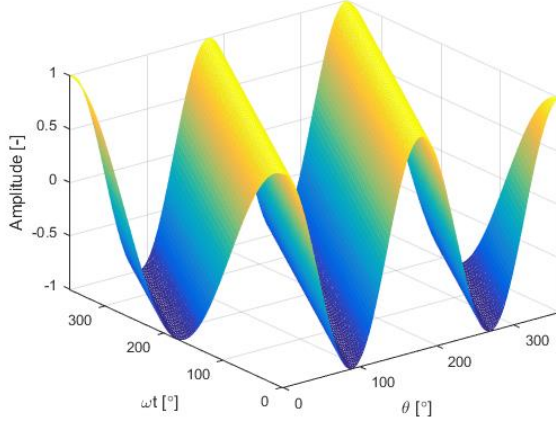


Figure 6.1 Graphical representation of the amplitude of the normal component of the air-gap flux density in both time and space.

To visualize the impact that the shape of the air-gap flux density has on the resulting electromagnetic forces, a simple example is presented: here, the normal force is calculated while neglecting the tangential flux density, which is relatively small as compared with the normal flux density. To keep the example general, the flux contribution from the rotor and the stator are kept as separate quantities; indices r and s represent rotor and stator quantities, respectively. Under these assumptions, the normal force density is then described as

$$\begin{aligned}
 f_n &= \frac{1}{2\mu_0} (B_{nr} + B_{ns})^2 = \frac{1}{2\mu_0} (B_{nr}^2 + B_{ns}^2 + 2B_{nr}B_{ns}) = \\
 &= \{B_{nr} = R \cos(\omega_r t - \theta), B_{ns} = S \cos(\omega_s t - \theta)\} = \\
 &\frac{1}{2\mu_0} (R^2 \cos^2(\omega_r t - \theta) + S^2 \cos^2(\omega_s t - \theta) + 2RS \cos(\omega_r t - \theta) \cos(\omega_s t - \theta))
 \end{aligned} \tag{6.5}$$

Since the modeled machine is of synchronous type, then $\omega_r = \omega_s = \omega$, yielding

$$\begin{aligned}
 f_n &= \frac{1}{2\mu_0} (R^2 + S^2 + 2RS) \cos^2(\omega t - \theta) \\
 &= \frac{1}{2\mu_0} (R^2 + S^2 + 2RS) \left(\frac{1 + \cos(2\omega t - 2\theta)}{2} \right)
 \end{aligned} \tag{6.6}$$

Hence, for a pure sinusoidal air-gap flux density, the resulting normal force is always positive and oscillates at two times the synchronous frequency. This is to be expected, as the attraction force between rotor and stator does not depend on the magnetic polarity. It can also be deduced from (6.6) that the normal force is identical on both sides of the machine because of the 2θ term. As a result, the resulting attraction force between the rotor and stator is zero for the entire machine, since at each position there is an opposing force with identical amplitude on the other side of the machine (i.e. 180° mechanically out of phase). However, if either the stator or rotor (or both)

contributes with a component that makes the air-gap flux density non-symmetrical, then the resulting attraction forces will no longer be zero, leading to machine noise and vibrations.

In practical implementations, it is not feasible to design the machine to have a pure, perfectly symmetric sinusoidal air-gap flux density. As a simplified example of a more realistic shape of the air-gap flux density, the stator contribution to the air-gap flux density of the small machine presented in Section 4.1 is depicted in Figure 6.2 during a single time instance. For this machine, the spatial wave contains several space harmonics components; this is due to the fact that the machine utilizes a concentrated winding design, which causes stepwise changes in the flux density. The twelve teeth and the concentrated windings of the modeled machine are clearly visible as the level of flux density changes twelve times over air-gaps circumferential. However, it should be stressed that the flux contribution presented in Figure 6.2 is a simplified version as it assumes no leakage flux and no space between stator teeth. A more realistic representation of the stator flux contribution of the small machine is presented later in Figure 6.4

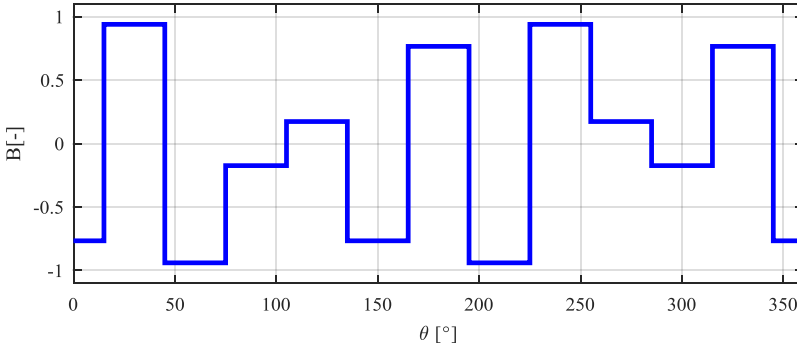


Figure 6.2 The idealized stator contribution to the air-gap flux density for the small modeled machine for one time instance.

For machines with concentrated windings, the shape of the flux density in the spatial domain is far from being a single frequency component. Hence, in order to have a more accurate representation of the normal component that is able to describe any time varying air-gap flux density, (6.4) can be extended using a Fourier series as

$$B_n \propto \sum_n^{\infty} \sum_v^{\infty} \cos(n\omega t - v\theta) \quad (6.7)$$

where harmonics in both the time and space harmonics are considered. In (6.7), the term $v\theta$ represents the decomposition modes of the spatial wave, where v represents the circumferential order of the mode. As an illustrative example of the decomposition modes of the spatial wave, Figure 6.3 presents three decomposed modes, where the selected modes have circumferential order one, two and five. The

decomposed modes of the spatial wave can be used to evaluate the normal force ability to mechanically deform the machine's frame into the shape of that specific mode. For electrical machines, it is the modes of low circumferential order that are of most interest [40], because the mechanical deflection becomes greatly reduced with increasing circumferential order. The mechanical deflection, β , depends on the circumferential order as [39].

$$\beta \propto \frac{1}{v^4} \quad (6.8)$$

i.e. doubling of the circumferential order results in 1/16 of the mechanical deflection force for an input with a given amplitude.

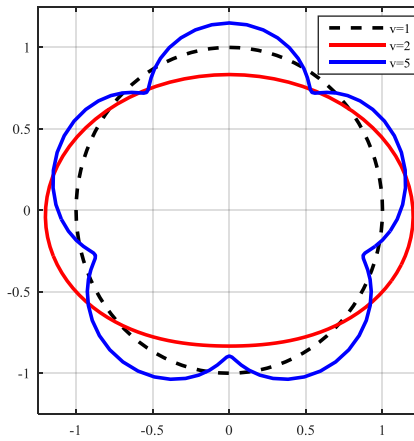


Figure 6.3 Graphical representation of three decomposed modes of the spatial wave. In this figure modes with circumferential order one, two and five are presented.

Therefore, machines with high order components of the normal force density do not necessarily produce stronger noise or vibrations during normal operation as compared to other machine designs. However, to be able to accurately estimate the vibrations that a specific machine design may generate, accurate models of both the mechanical structure and the air-gap flux density are needed.

6.2 Rotor and stator air-gap flux contribution for smaller modeled machine

As shown in the previous section, machines with a pure, symmetrical sinusoidal air-gap flux density has a no resulting attraction force between rotor and stator and it will therefore not produce vibrations. However, it is practically impossible to design and manufacture a machine that achieves a perfect sinusoidal air-gap flux density. As examples of design restrains that impact the shape of the air-gap flux density are the windings, which need to be constituted by a discrete number of turns. In addition, the

turns cannot be freely distributed within the machine, due to the slots and the teeth, which also impacts the reluctance of the flux path and thereby the flux distribution. Limitations posed on the rotor's contribution to the air-gap flux are caused by the available shape of the magnets and how these can be positioned. In order to achieve a sinusoidal air-gap shape, it might be necessary to apply an ineffective design and use of the magnet, which might lead to large leakage flux between the magnets. Therefore, during the design of commercially available machines, typically the designer has made a compromise in order to have better material utilization and machine efficiency at the expense of air-gap flux density harmonics and thereby the resulting additional mechanical stress. If the machine is not properly designed with respect to both electrical and mechanical properties, the electromagnetic forces may coincide with poorly damped modes of the mechanical structure. The worst case scenario is if one of the electromagnetic force component coincides with a resonance mode of the machine's frame. In this case, the generated machine vibrations can cause other issues and lead to a reduced lifetime of the mechanical components. However, these resonant conditions are unlikely to occur for synchronous machines; the problem is slightly more pronounced in case of variable speed drives, where a larger speed range of operation increases the probability to encounter a resonance condition.

To be able to avoid triggering the mechanical resonances of the machines, FEM softwares can be used to acquire both the mechanical modes and the air-gap flux density. Since only the electromagnetic properties are considered in this thesis, only the air-gap flux densities of the modeled machines are presented in this chapter. The individual contribution to the air-gap flux density from both the rotor and stator can be evaluated using the FEM software through appropriate selection of the simulation conditions. The stator's contribution can be found by selecting a single frequency current excitation in the stator windings while removing the rotor magnets. For the small machine presented in Section 4.1, the base speed used is 1500 rpm and with its five pole-pairs this gives a fundamental frequency of 125 Hz. As a result, in order to acquire the stator's contribution to the air-gap flux, the frequency of the excitation current is set equal to 125 Hz, while its amplitude is equal to 1 A. The simulated amplitude of the normal component of the air-gap flux density, when only the stator excitation is present, is shown in Figure 6.4, which considers both the time and position dependence. In agreement with what has been presented in Figure 6.2, due to the machine's concentrated windings the spatial wave does not present a pure sinusoidal shape. In contrast to the model presented in Figure 6.2, the FEM model includes the slot openings, which can be seen by the increase in flux level at the teeth edges (slot opening at every 30°). The increase is caused by the flux concentration due to the flux leakage between the neighboring teeth.

From a 2D-Fourier analysis (see Figure 6.4b), it can be seen that stator's contribution to the air-gap flux density only contains harmonics in the spatial domain. This is to be expected, since the system has been excited with a pure single frequency current at the fundamental frequency, i.e. there is only one excitation source in the time domain. It can also be seen that the component of negative fifth circumferential

order has the highest amplitude, which confirms that selecting a five pole pair rotor was a good choice as it utilizes this specific stator design in an optimal way.

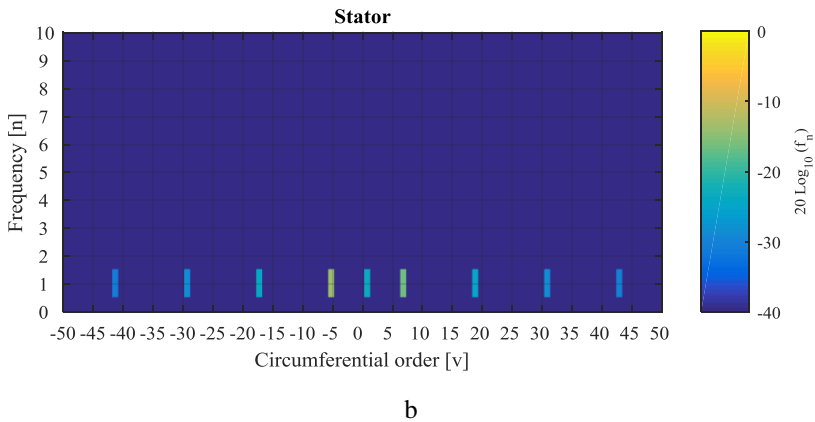
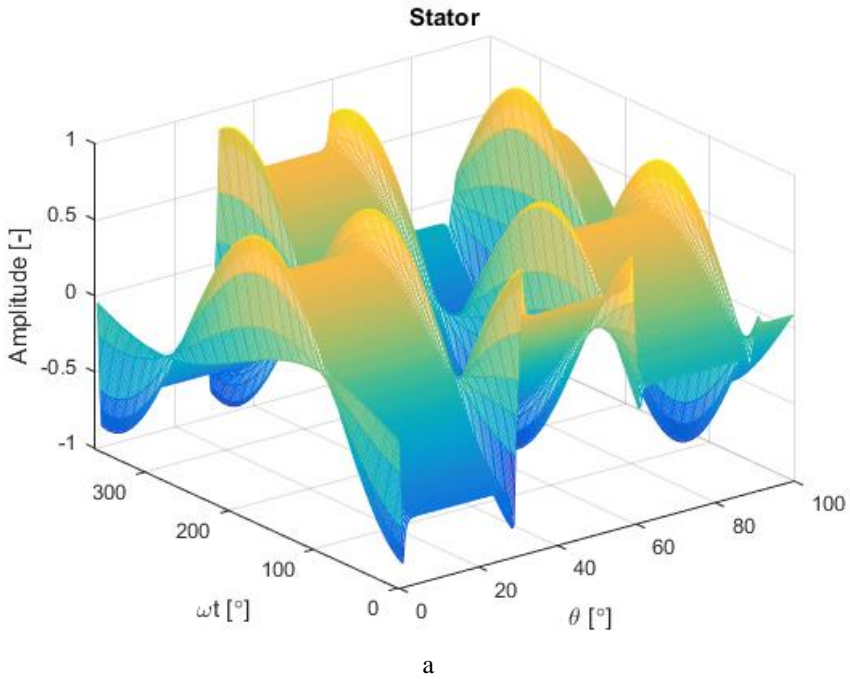


Figure 6.4 Figure a presents a graphical representation of the amplitude of the normal component of the stator's contribution to the air-gaps flux density in both time and space. Figure b presents the 2D-Fourier analysis of the data presented in figure a.

Similarly, the rotor's contribution to the air-gap flux density can be acquired from the FEM model by letting the machine to rotate at 1500 rpm while the stator currents are forced to zero, i.e. open circuit operation. The simulated rotor's contribution to

the normal component of the air-gaps flux density together with the 2D-Fourier analysis are presented in Figure 6.5. Unlike the stator's contribution, the rotor's contribution contains both time and space harmonics. This is not surprising, due to the step-like shape of the back-EMF presented in Figure 4.4.

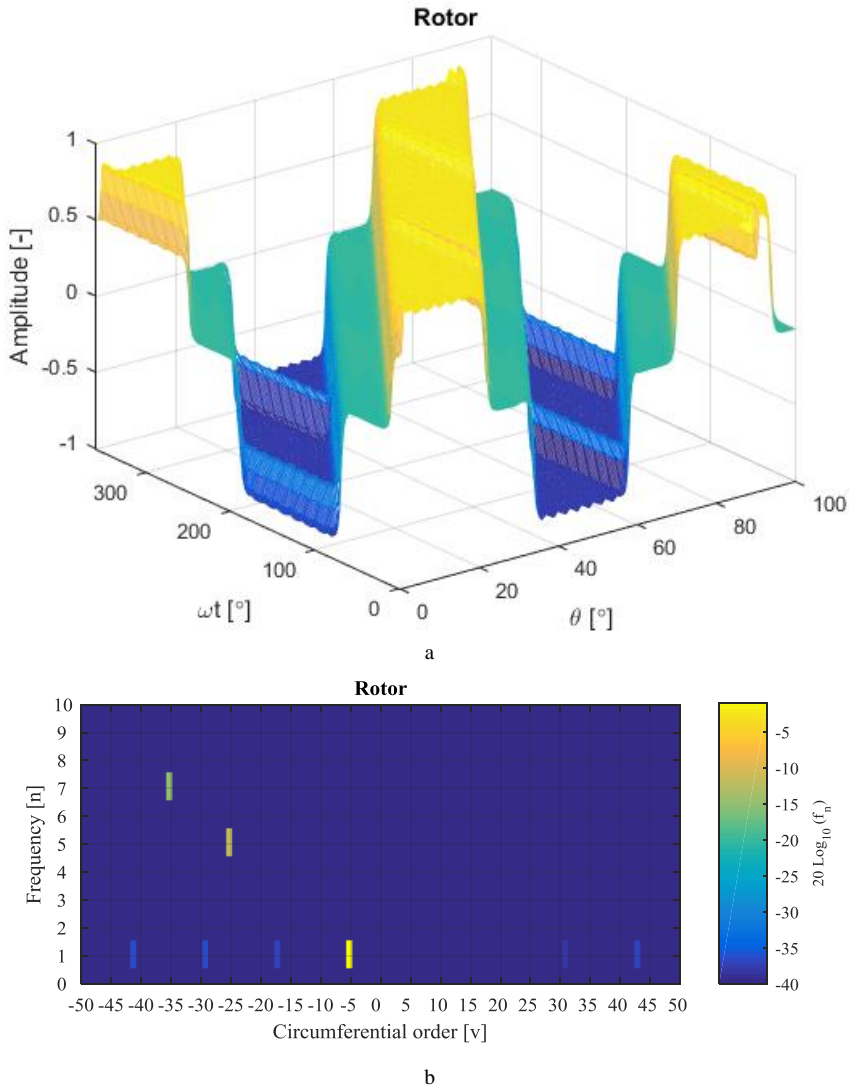
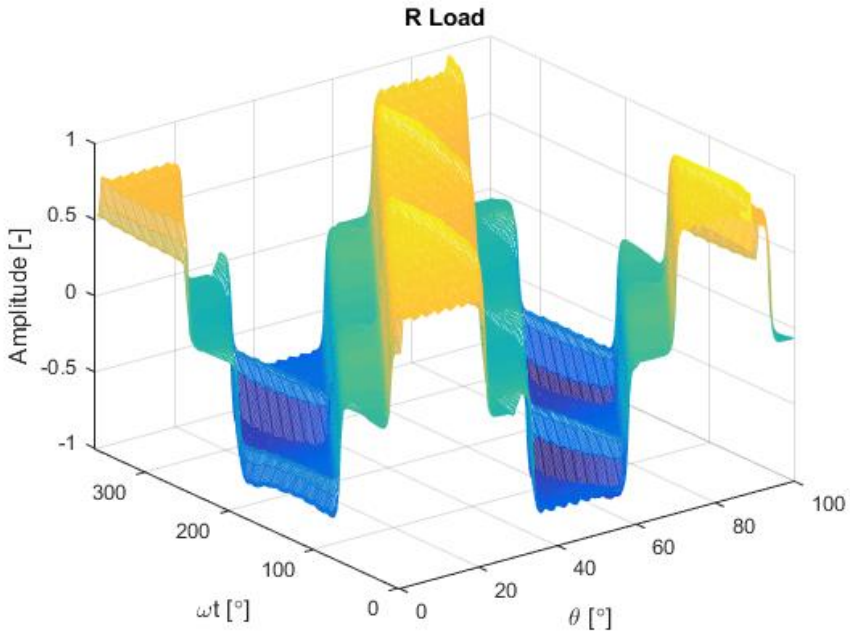


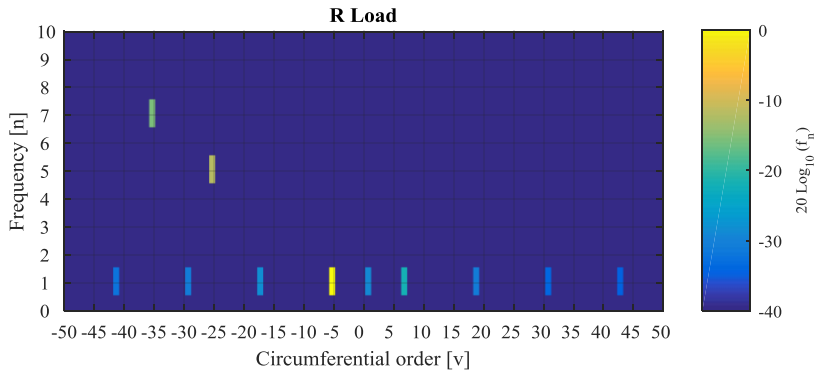
Figure 6.5 Figure a presents a graphical representation of the amplitude of the normal component of the rotor's contribution to the air-gaps flux density in both time and space. Figure b presents the 2D-Fourier analysis of the data presented in figure a.

From Figure 6.5b it can also be seen that dominating harmonic component is at the fundamental frequency in the time domain and at the negative fifth circumferential order.

However, any force or vibration is caused by the total air-gap flux, i.e. the combination of both the rotor and stator fluxes. The FEM model is therefore simulated during normal operational conditions to acquire the resulting air-gap flux density; in particular, the machine is simulated under generator operation with a pure resistive load connected to its terminals. The resulting normal component of the air-gap flux density is shown in Figure 6.6a. From the figure, it can be observed that stator reaction only has a limited impact on the air-gap flux density for this machine, as the shape of the flux density is very similar to the one presented for no-load operation. However, from the 2D-Fourier analysis of the air-gap flux density presented in Figure 6.6b the stators contribution is clearly visible as there are more components than for the no-load case. Since the FEM model assumes linear materials, it is to be expected that the resulting air-gap flux density consists of the summation of the rotor's and stator's individual contributions.



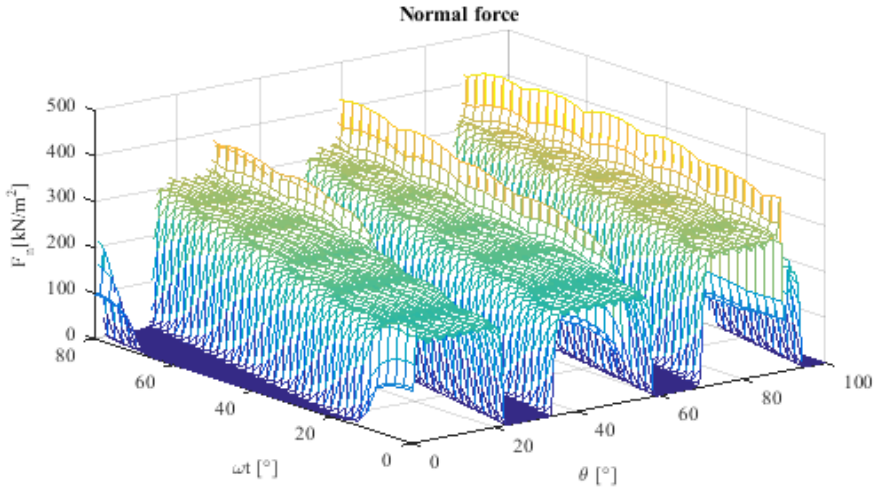
a



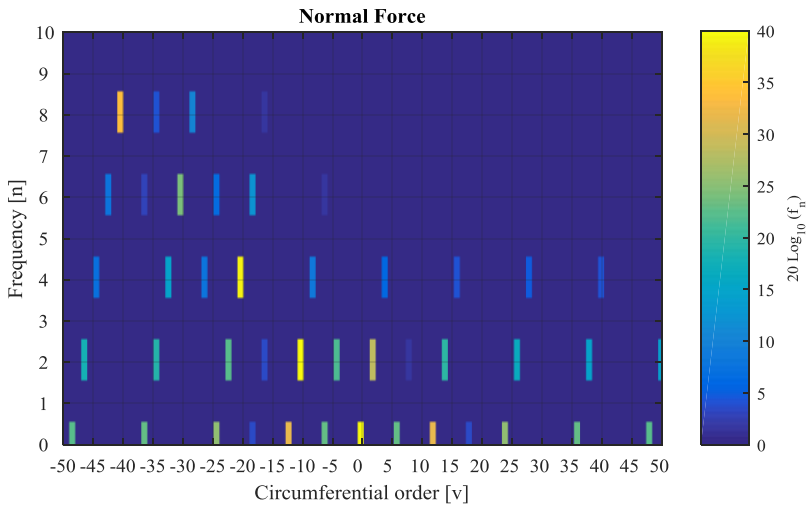
b

Figure 6.6 Figure a presents a graphical representation of the amplitude of the normal component of the air-gaps flux density in both time and space during generator operation with a pure resistive load. Figure b presents the 2D-Fourier analysis of the data presented in figure a.

With the use of the acquired air-gap flux densities, the normal force density can be calculated by using (6.1). The resulting normal force for the modeled machine under the given operating conditions is presented in Figure 6.7. Since both the resulting normal and tangential air-gap flux density components contain harmonics, it is not surprising that normal force density contains even more harmonics, as can be seen in Figure 6.7b. These additional harmonics are caused by the cross coupling indicated in the square term in (6.1). Even though the normal force density contains several components, it is the mechanical structure of the machine frame which determines which of these components results in measurable vibrations. The normal force density components of lower circumferential order are more likely to cause measurable vibrations because of the mechanical deflection, as described by (6.8). However, it is of importance to stress that which of the component that actually will result in measurable vibrations cannot be determined without information on mechanical structure of the machine frame; in general, it can be considered that high circumferential order components are unlikely to cause measurable vibrations.



a



b

Figure 6.7 Figure a presents a graphical representation of the amplitude of the normal force density in both time and space during generator operation with a pure resistive load. Figure b presents the 2D-Fourier analysis of the data presented in figure a.

Analogously, the tangential force density can be calculated using the acquired fields and (6.2). However, unlike the normal force, the tangential force does not create an opposing force on the other side of the machine (i.e. a 180° mechanical shift): the tangential force contributes to the machine torque in every position of the air-gap. The total machine’s torque can therefore be acquired by integrating the tangential

force density along the circumferential of the air-gap for every time instance. The resulting torque is presented in Figure 6.8. As already discussed in Section 5.2, the machine presents some torque ripple, due to the harmonic components in the air-gap flux density. However, since the peak-to-peak ripple is only about 10% of average torque and considering that the ripple has relatively high frequency, it is very likely that the torque ripple will be effectively damped by the mechanical drive-train and therefore will not cause any issues during normal operation.

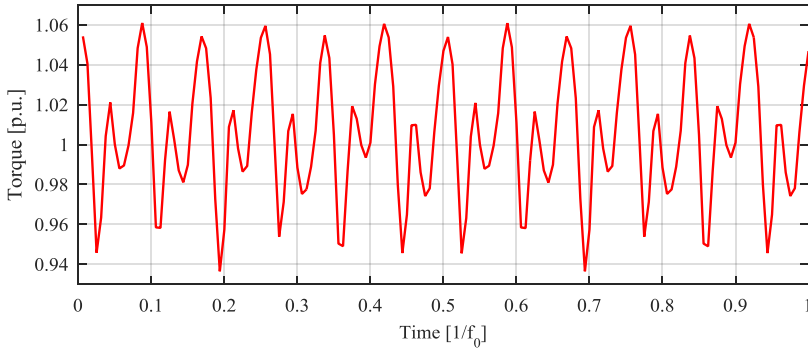


Figure 6.8 The machine's calculated torque using the air-gap flux density.

The results presented so far consider a non-faulted model of the PMSM. In the event of a turn-to-turn fault, the symmetry of the machine is lost; this is due to the fact that the air-gap flux density will be altered in the vicinity of the fault compared to the pre-fault value. Therefore, a turn-to-turn fault will have an impact both on the normal force density and on the tangential force density. The fault may therefore introduce new vibrations in the machine frame and, as seen in Section 5.2, increase the torque ripple.

6.3 Impact of a turn-to-turn fault on the electromagnetic forces

To investigate the impact that a turn-to-turn fault has on the electromagnetic forces of a PMSM, the model of the small faulted machine presented in Section 4.2 is used in this section. As in Section 4.2 and in the previous section of this chapter, the model is simulated during generator operation loaded with a pure resistive load for comparison purposes. Because of the inherent property of the induced fault current to oppose any change in flux, the flux level in the vicinity of the fault will be reduced. Figure 6.9a presents the resulting normalized normal component of the air-gap flux density during one time instance for both faulted and non-faulted models; for the faulted model, only one turn has been short circuited. As can be seen for the first 30° (the location of tooth with the faulted coil) in Figure 6.9a, the flux of the faulted model is slightly reduced as compared with the non-faulted machine. Since the normal component of the flux density is much greater than the tangential component, the normal force be approximated to be proportional to square of the normal flux density component, see (6.1). Figure 6.9b therefore presents the squared value of the

normal flux component, where the fault's impact is even more visible. From Figure 6.9b, it can clearly be seen that symmetry is lost in the vicinity of the fault. As an example, the normal forces at 10° and 190° are not equal for the faulted model. This difference leads to a non-zero resulting normal force.

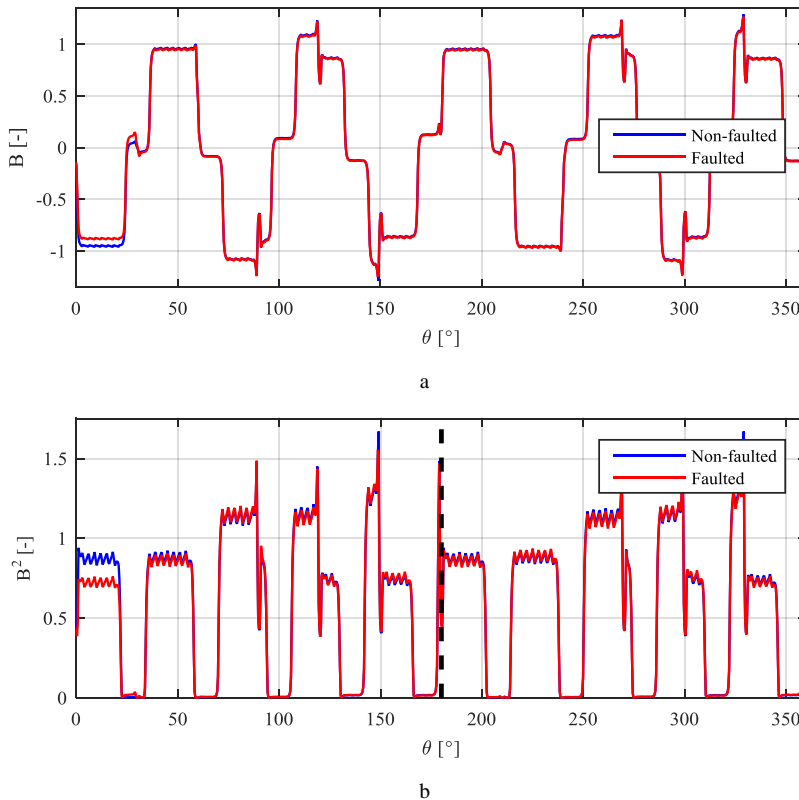
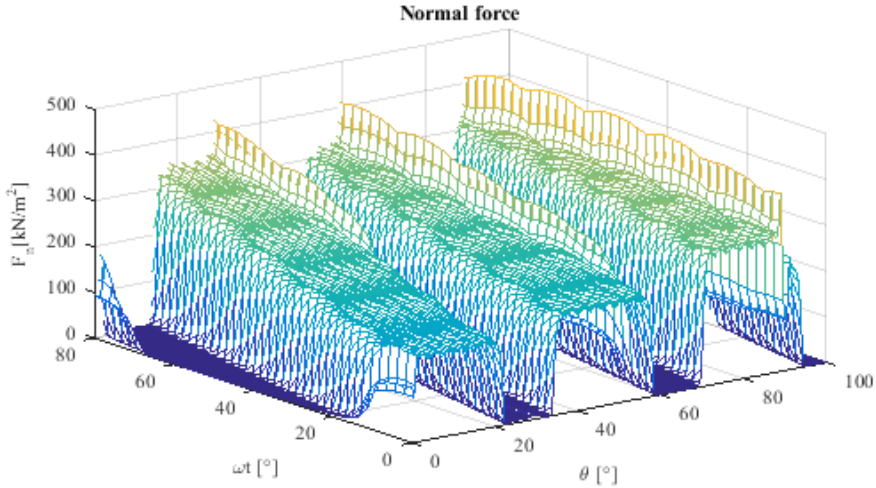


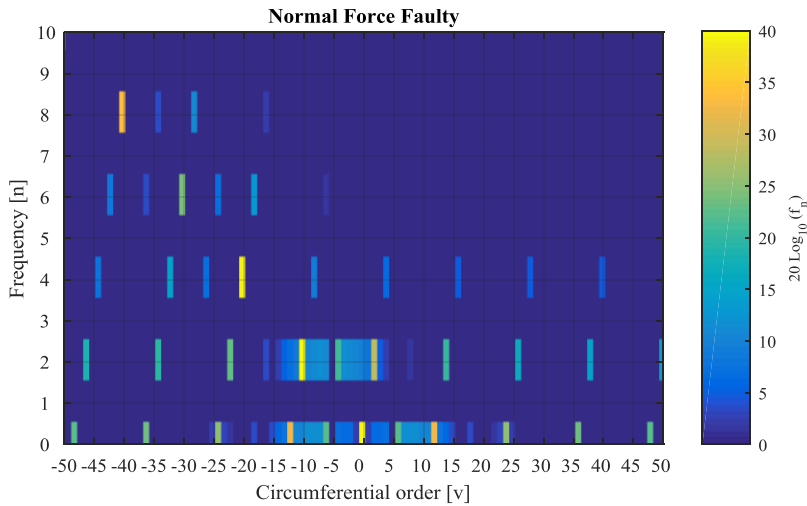
Figure 6.9 Normalized normal component of the air-gap flux density for one time instance during generator operation for faulty and non-faulted machine model. Figure b presents the square of the value presented in figure a.

Figure 6.10 presents a more complete view of the normal force density for the faulted machine model when one turn is short-circuited. Through a close comparison between Figure 6.7a and Figure 6.10a, the normal force density for the faulted machine is reduced for a portion of the air-gap (at the mechanical angles 0° - 20°), as in the case presented in Figure 6.9b. Since the fault alters the shape of the air-gap flux density, additional harmonic components are introduced by the fault, see Figure 6.10b. The components introduced by the fault for the simulated scenario are of low circumferential order at two times the fundamental frequency in the time domain. As expected from the comparison presented in Section 5.3, the fault has not introduced new time domain components, i.e. the simulated fault condition is not severe enough to cause a sufficiently large stator reaction which fundamentally alters the shape of

the air-gap flux density. However, the fault has a more substantial impact on the spatial wave and the additional components are likely to cause additional stress on the machine's mechanical structure. In addition, the presence of additional modes increases the risk for excitation of mechanical resonances.



a



b

Figure 6.10 Figure a presents a graphical representation of the amplitude of the normal force density in both time and space for the faulted machine during generator operation with a pure resistive load. Figure b presents the 2D-Fourier analysis of the data presented in figure a.

Since the fault does only introduces additional spatial harmonics, it indicates that it may be more efficient monitor the machine vibrations rather than any of the electrical quantities from a fault detection perspective. As the fault does introduce additional components, i.e. not only alters the already existing components, it will impact the amplitude of the machine vibrations.

For the non-faulted machine, the largest electromagnetic normal force components (with low circumferential order) are at two times the fundamental component with the circumferential orders -10 , -4 , 2 and 14 . The normal force of these components can be described as

$$f_{n_{nonfault}} = (f_{n-10} \cos(2\omega t - 10\theta) + f_{n-4} \cos(2\omega t - 4\theta) + f_{n2} \cos(2\omega t + 2\theta) + f_{n14} \cos(2\omega t + 14\theta)) \quad (6.9)$$

In the case of the faulted machine, there are additional components at this frequency with low circumferential order, more specifically the circumferential order of the components of faulted machine range from -13 to 3 (except for -5 , and it also includes 14 as the non-faulted machine do). The resulting normal force for the faulted machine can then be describes as

$$f_{n_{fault}} = (f_{n-10} \cos(2\omega t - 10\theta) + \dots + f_{n-6} \cos(2\omega t - 6\theta) + f_{n-4} \cos(2\omega t - 4\theta) + \dots + f_{n3} \cos(2\omega t + 3\theta) + f_{n14} \cos(2\omega t + 14\theta)) \quad (6.10)$$

which has a larger amplitude as compared to the normal force of the non-faulted case. It is therefore likely that the fault will either increase the amplitude of already existing vibrations at two times the fundamental frequency or introduce vibrations at this frequency if there were not present prior to the fault. Hence, these results indicates that machine vibrations may be used to detect a turn-to-turn fault. If vibrations are to be used as a detection method, the most effective solution would be to use several synchronized vibration sensors that are spatially distributed over the machine frame, in order to be able to acquire both the frequency of the vibration as well as the circumferential order. The knowledge of these two quantities allows not only to detect amplitude changes, but also the introduction of additional components, thus increasing the accuracy of the detection method.

Since a turn-to-turn fault does not only impact the normal force density, it is of interest to also investigate how the machine's torque production is affected. As in the previous section, the machine torque is acquired through the integration of the tangential force density along circumferential of the air-gap. The resulting machine torque for the faulted machine is presented in Figure 6.11. As previously shown in Section 5.2, the most visible change is the increase of the amplitude of the torque ripple; also, a new dominating component at two times the fundamental frequency can be observed. Therefore, a turn-to-turn fault will not only cause additional vibrations in the machine frame, but will also affect the output torque. The introduced torque ripple may excite mechanical modes in other part of the mechanical drivetrain. However, any potential impact a torque ripple introduced by a fault may have on the

mechanical drivetrain is out of scope for this thesis and will therefore not be discussed further.

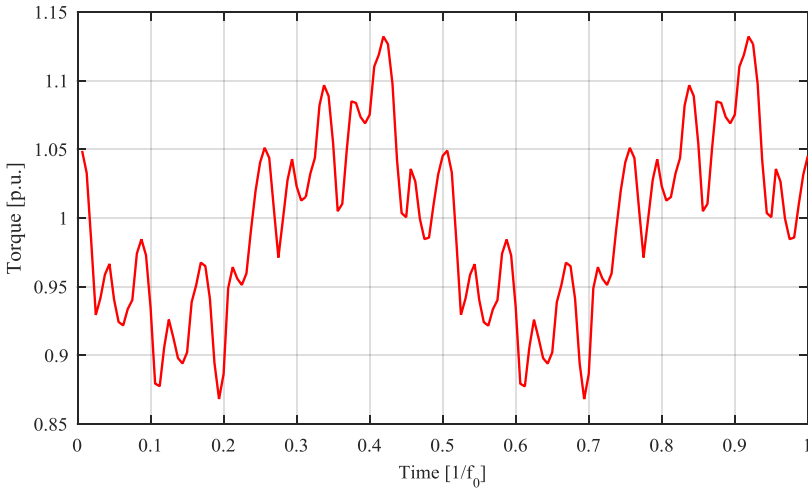
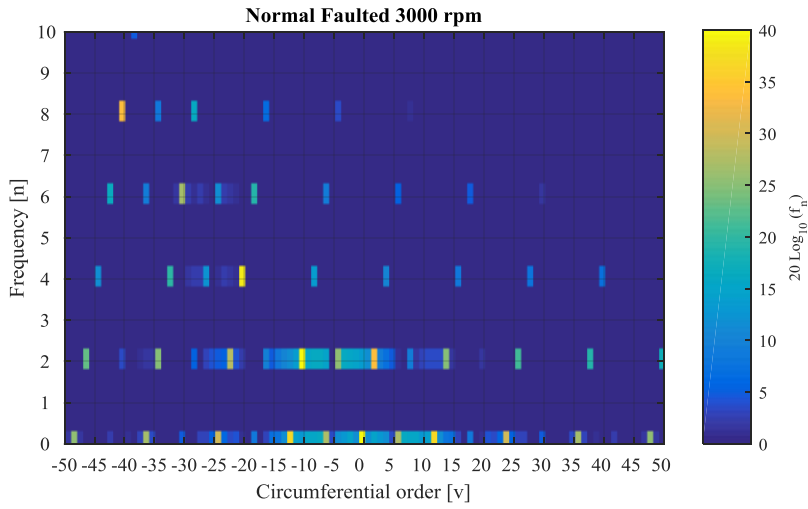
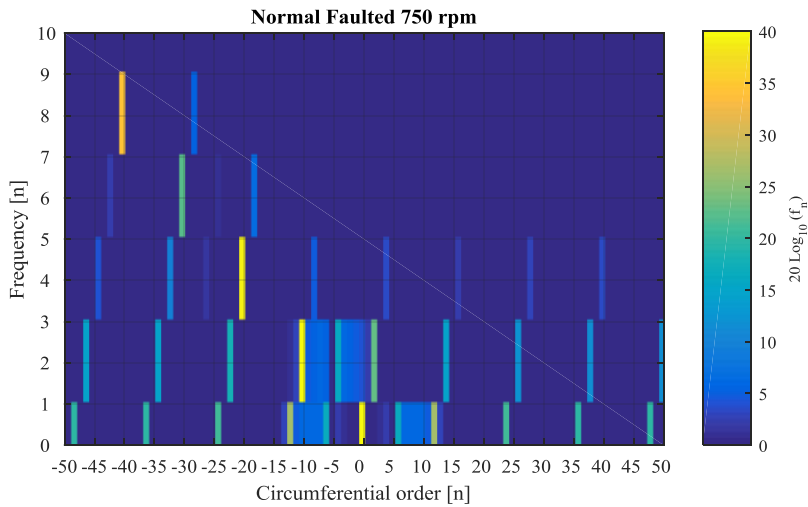


Figure 6.11 The faulted machine's calculated torque using the air-gap flux density.

In order to investigate if the different components introduced by the fault are dependent on the operational speed of the machine, the model of the faulted machine is simulated at two times the nominal speed as well as at half the nominal speed, i.e. at 3000 rpm and at 750 rpm, respectively. Figure 6.12 presents the resulting 2D-Fourier analysis for the two case studies; note that the fundamental frequency changes with the speed, i.e. for 3000 rpm it is 250 Hz and for 750 rpm it is 62.5 Hz. As can be seen, the fault introduces additional spatial components for all speeds, but the simulations shows that both the number of introduced components increases with speed and that the amplitude of the previously introduced components increase with an increase in speed. This is to be expected as an increase in speed leads to larger induced fault current, causing a greater impact on the air-gap flux density. The torque ripple does also increase with the speed, following the same trend as in the previous simulation: a new dominating ripple component at two times the fundamental frequency is introduced and its amplitude increases with the machine speed.



a



b

Figure 6.12 2D-Fourier analysis of the air-gap flux density, figure a presents the results when the machine is rotating at two times the nominal speed and figure b presents the results from half nominal speed.

Since a turn-to-turn fault of only a few short-circuited typically evolves with an increasing number of short-circuited turns due to the produced heat, it is of interest to investigate how the electromagnetic forces change when increasing the number of short-circuited turns. Figure 6.13 presents the resulting 2D-Fourier analysis of the normal force when three turns are short-circuited, i.e. 15% of the winding is short

circuited and the machine is rotating at 1500 rpm. With more faulted turns the fault current increases, but more crucially the inductance of the fault-loop greatly increases, causing the fault to have a greater impact on the air-gap flux density. The increased severity of the fault can be seen through the addition of even more harmonic components compared to when only one turn is short-circuited for this speed. In addition, the amplitude of the components introduced by the single turn fault has greatly increased with the increased number of short-circuited turns.

As a consequence of the fault's greater impact on the air-gap flux density, the additional components are no longer limited to appear at two times the fundamental frequency, even though these components are the most affected ones. New components are introduced at higher frequencies, but as for the single turn fault case, the fault only introduces additional components at new circumferential orders at previously present frequencies. Note that, even though new components at higher frequency have appeared for the more severe fault, the circumferential order of the introduced components are still high and will therefore likely be too heavily damped by the mechanical structure, meaning that they will most likely not lead to measurable vibrations.

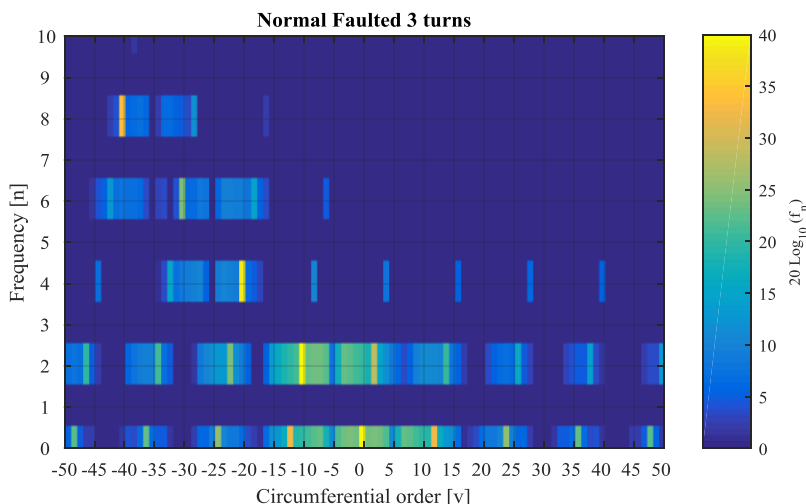


Figure 6.13 2D-Fourier analysis of the air-gap flux density then three turns are short-circuited when the machine is operating as a generator at nominal speed.

The increased fault severity also impacts the machine's torque, leading to an increase of the torque ripple up to 80% peak-to-peak of the average torque when three turns are short-circuited.

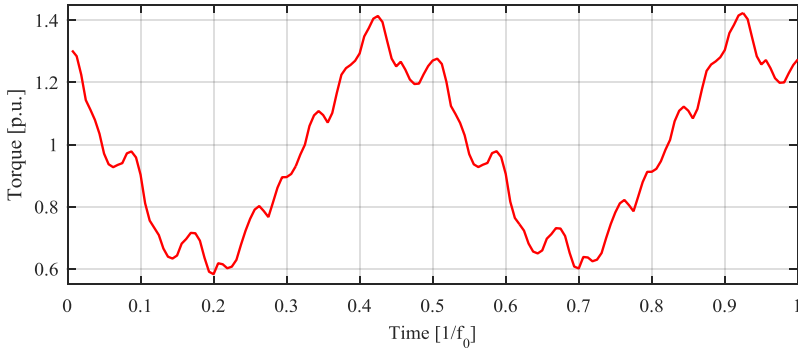


Figure 6.14 The faulted machine's calculated torque using the air-gap flux density when three turns are short-circuited.

If the severity of the fault is increased even further, the faults impact on the air-gap flux density is large enough that it is able to alter the air-gap flux shape, as new frequency component are introduced. Figure 6.15 presents the simulation results during generator operation at nominal speed when five turns are short circuited, i.e. 25% of the total winding (i.e., for the modeled machine one complete coil, of out four, is short-circuited). That the severe fault has a strong impact on the air-gap flux density is clearly visible in the normal force density, as it is almost zero in the vicinity of the fault. The flux generated by the fault-loop is close to that of the magnets, resulting in a very low flux density in the air-gap close to the fault, and by extension a low normal force density. However, analogously with the previous simulations, the new component that are most likely to cause a measureable vibrations are those at two times the fundamental frequency, as the amplitude of these components increases the most with an increasing number of short-circuited turns.

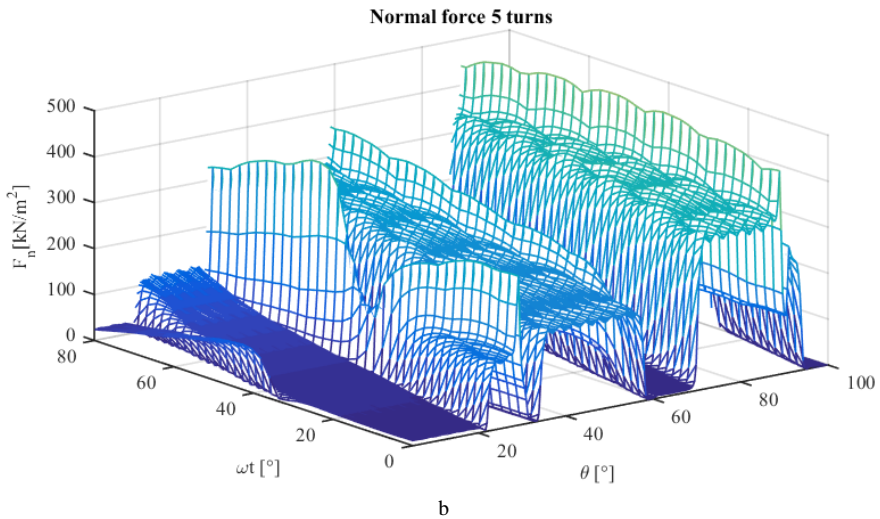
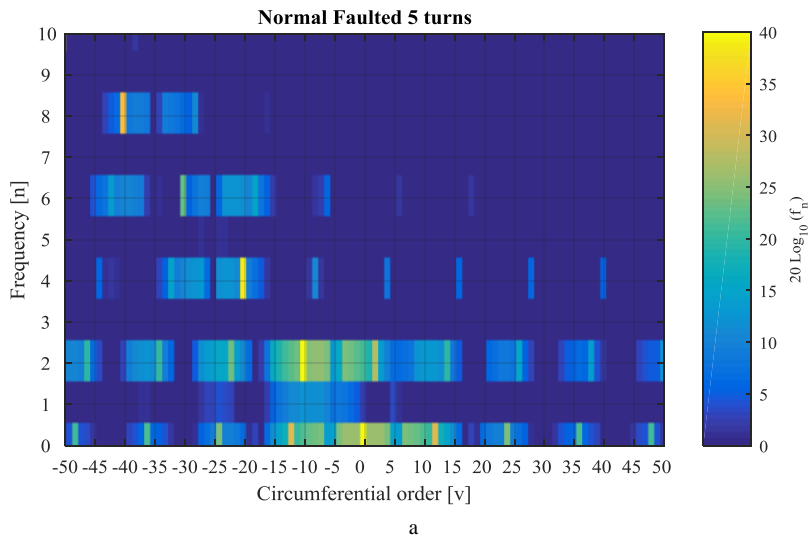


Figure 6.15 Figure a presents the 2D-Fourier analysis of the air-gap flux density then five turns are short-circuited when the machine is operating as a generator at nominal speed. Figure b presents the machine torque during this operation.

In the case of the machine torque, the torque ripple increases even further when the fault severity is increased, see Figure 6.16. However, similarly to the normal force component, an additional component at the fundamental frequency (but with low amplitude) is introduced for severe fault conditions.

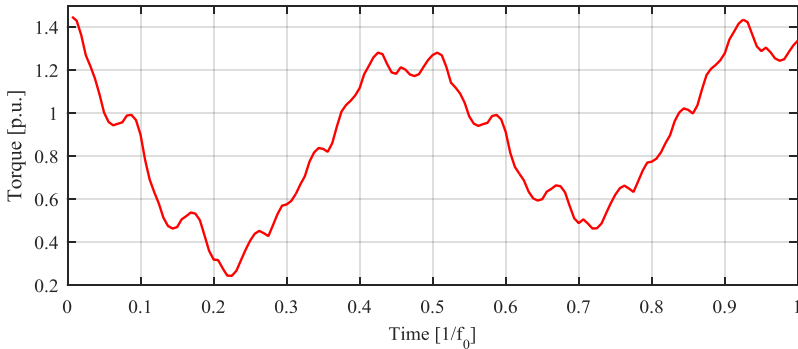


Figure 6.16 The faulted machine's calculated torque using the air-gap flux density when five turns are short-circuited.

From the simulations with increasing fault severity a trend can be identified: a turn-to-turn fault where only a few turns are short-circuited introduces additional normal force components with low circumferential order at two times the fundamental frequency with low amplitude. As the fault severity increases with more short-circuited turns, the amplitude of the introduced components increases and additional components are introduced. At a certain point, the fault will introduce new frequency components which are of low circumferential order. As more and more components of low circumferential order are introduced, it is very likely that fault causes measurable changes in the machine vibrations.

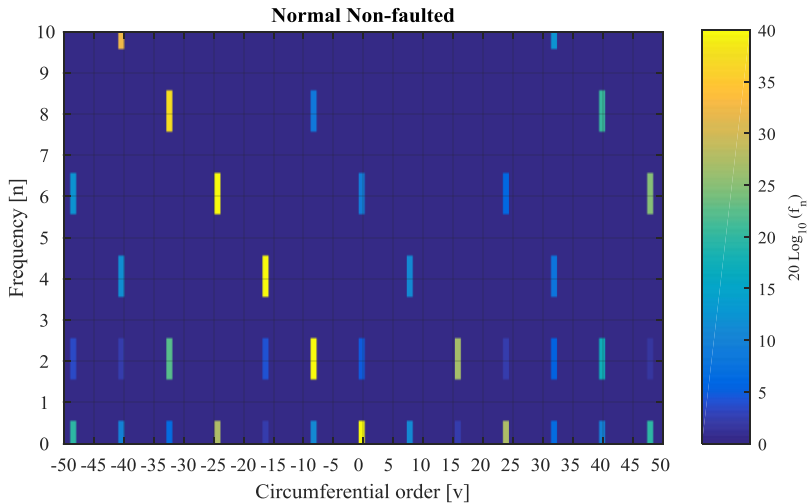
For the machine torque, an increasing number of short-circuited turns leads to a drastic increase of the torque ripple. The ripple component introduced by the fault is at two times the fundamental frequency; similarly to normal force density, for really severe fault cases an additional frequency component at the fundamental frequency will also appear but with a lower amplitude compared to the two times frequency component.

6.4 Parallel windings

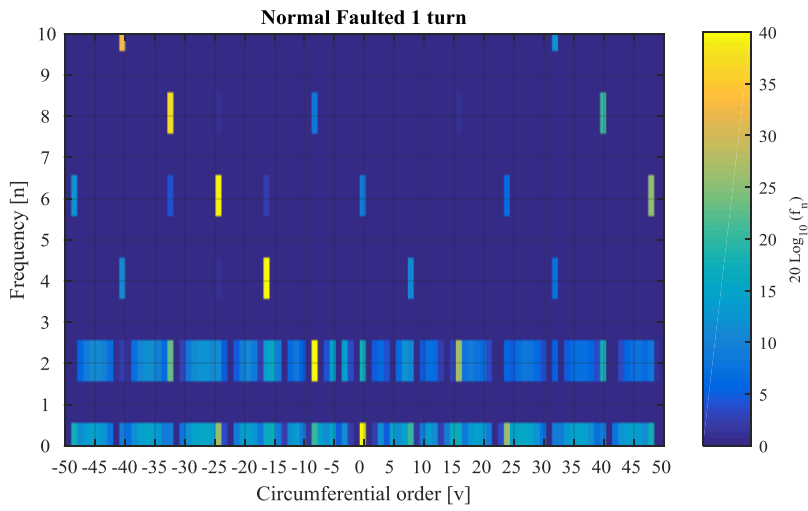
In order to verify that the impact the turn-to-turn fault has on the electromagnetic forces does not vary with machine design, the normal forces of the larger machine with parallel windings presented in Section 4.4 is here investigated. The model is selected to operate as a generator loaded with a pure resistive load operating at nominal speed (750 rpm), in order to be able to make a fair comparison with the results obtained for the small machine. The large machine has different number of pole-pairs and nominal speed compared to small one; thus, the fundamental frequency of these two machines is different: 50 Hz for the large machine and 125 Hz for the small. However, since the 2D-Fourier analyses are presented related to each respective fundamental components and circumferential size, a comparison can be easily performed. The selected cases to be investigated for the large machine

are: non-faulted conditions, one short-circuited turn and seven short-circuited turns (out of the 42 turns in one of the parallel braches). The resulting 2D-Fourier analyses for these cases are presented in Figure 6.17.

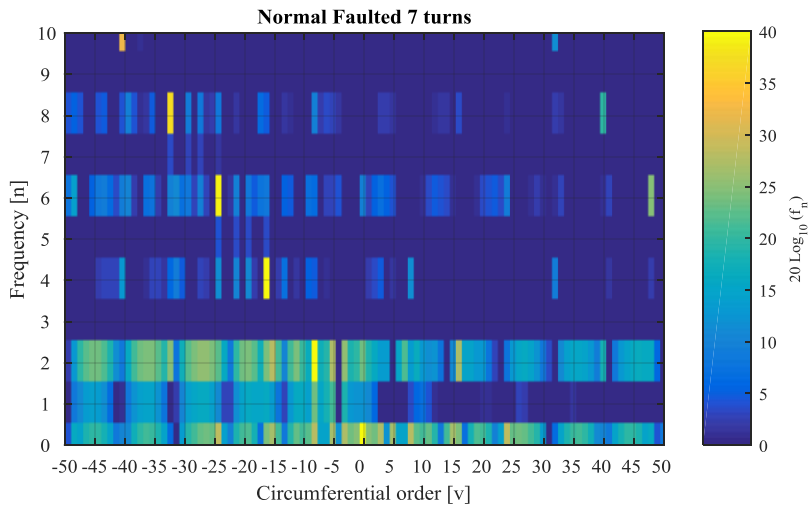
Because of the different designs of the two machines, their normal force density components during non-faulted operation are different. However, the presence of the fault results in a similar behavior for the two machines. When a single turn is short-circuited, additional components at two times the fundamental frequency are introduced. It should be stated that the large machine is designed with a strong coupling between the rotor magnet and the stator winding, in order to achieve the a desired induced voltage during normal operation. However, this design feature leads to a large fault current when a turn-to-turn fault occurs, even when only one turn is short-circuited (note that one turn represents about 2.4% of a branch for this machine). Because of the strong magnetic coupling, even a single turn fault has a considerable impact on the air-gap flux density, resulting in the introduction of several additional components at almost every circumferential order at two times the fundamental frequency. As for the small machine case, an increased number of short-circuited turns leads to more additional harmonic components, not limited to being at two times the fundamental frequency. The simulation of the large machine also shows that for severe fault cases, the components introduced by the fault can be of high frequency order while being of low circumferential order, i.e. high order frequency vibrations may be introduce by the fault.



a



b



c

Figure 6.17 2D-Fourier analysis of the normal force for the large machine during generator operation. The simulated cases are non-faulted, one and seven turns are short-circuited.

The machine torque for the large machine is affected by the fault, although to a smaller extent as compared with the small machine case. This can be seen in Figure 6.18, where the machine torque for the three simulated cases is presented. This is due to the fact that the fault has a relatively smaller impact on the complete winding. The most severe fault presented for the large machine is when seven turns are short-

circuited, which means that 16.7% of that branch is short-circuited. Since the presented machine has four parallel branches in one phase, seven short-circuited turns equates to a little more than 4% of the total phase winding being short-circuited. This is less than compared to a single turn for the small machine (where one turns equates to 5% of the winding). As a result, the ripple for the (presented) most severe fault case for the large machine is smaller than the ripple caused by the single turn fault of the small machine.

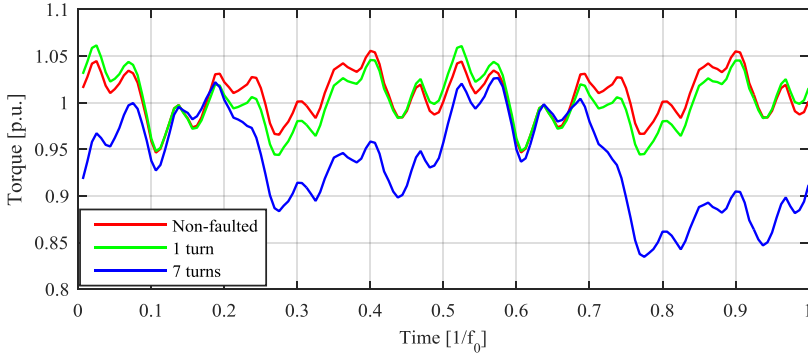


Figure 6.18 The machine torque of the large machine during generator operation for non-faulted operation and faulted operation with one and seven short-circuited turns.

To summarize, the fault introduces similar normal force density components on the larger machine as for the small machine case; also, the two machines present a similar trend as the fault severity increases. The two machines present less similarities when it comes to the impact of the fault on the machine's torque, as the impact is more closely related to the portion of the complete phase winding that is short-circuited rather than the absolute number of short-circuited turns.

6.5 Chapter summary

This chapter has been dedicated to the investigation of the impact of turn-to-turn faults on the electromagnetic forces of the machine. It has been shown that a fault consisting of only a few number of turns introduces additional normal force density components at two times the fundamental frequency but at low circumferential order. These components will likely result in an increase in the amplitude of the machine vibrations at this frequency, or introduce vibration at this frequency. The fault will also introduce a torque ripple component at twice the fundamental frequency. With an increasing number of short-circuited turns, the amplitude of the introduced normal force density component increases and additional components are identified. For severe cases, the fault introduces normal force density components at new frequencies. The torque ripple also increases with the fault severity. Similar trend can be identified also for the larger machine with parallel windings.

Chapter 7

Experimental setup of a PMSM with turn-to-turn fault

This chapter presents the experimental results attained from the laboratory setup in order to verify the results presented in the previous chapter. The experimental setup is constituted by a PMSM that has been modified in order to allow internal access to the phase windings.

7.1 The experimental setup

The machine used in the experimental setup is a prototype “in-wheel” machine, where the wheel is the machine rotor with neodymium magnets mounted on the inside of the rim. The stator is located at the wheel hub, as shown in Figure 7.1 that presents the in-wheel machine connected to the driving motor through the rubber damped shaft coupling. The in-wheel machine has been selected because for this validation due to its availability at the Chalmers laboratories and its data availability. Furthermore, its special design that does not present a traditional machine housing leaves the stator end-windings exposed and therefore more accessible.

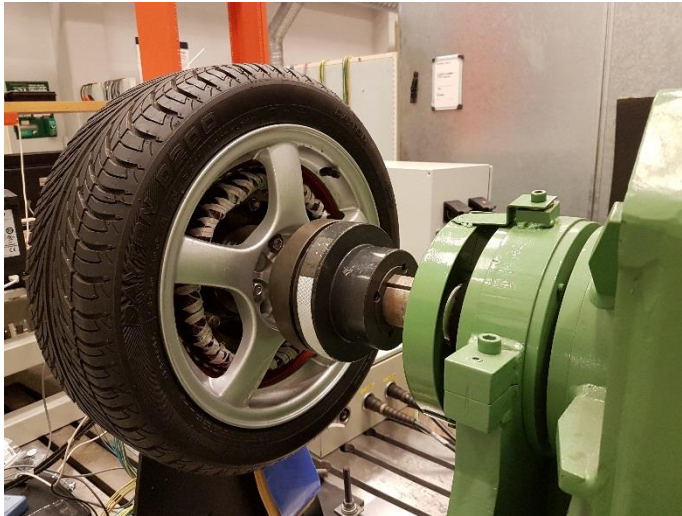


Figure 7.1 Picture of the “in-wheel” motor used in the experimental setup.

The continuous power rating of the in-wheel machine is 20 kW with a rated voltage of 400 V . It has 16 poles and the stator has 48 slots in which the three phases are

arranged in a double layer layout, similarly to the one for the large machine model presented in Section 4.4. Each phase is constituted by 16 series-connected coils, where each coils is constituted by 11 turns, resulting in a total of 176 series-connected turns per phase. Due to the high machine currents, the machine is wound with stranded wire consisting of five strands. In order to gain access to individual turns in a controlled order, the machine has been rewound in order to allow additional connection points soldered onto one of the winding strands of the winding while keeping the presented specifications. Figure 7.2 presents a schematic view of the added connections together with a picture of the actual connection. Due to space constrains, the rewinding could only provide access to five consecutive turns of the winding. As a result, up to four turns can remotely be short-circuited in a controlled way.

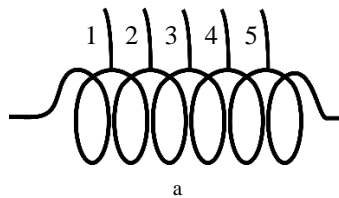


Figure 7.2 Figure a presents a schematic representation of the additional conductors and figure b presents a photo of the additional conductors added to the winding.

In order to be able switch from faulted and non-faulted operation in an easy and safe way, a small short-circuit device has been constructed. The device consists of two anti-parallel transistors together with their drive circuit. The device has been designed so that the fault could be activated either using a remote triggering signal or manually through a mechanical switch. A picture of the short-circuit device is presented in Figure 7.3.

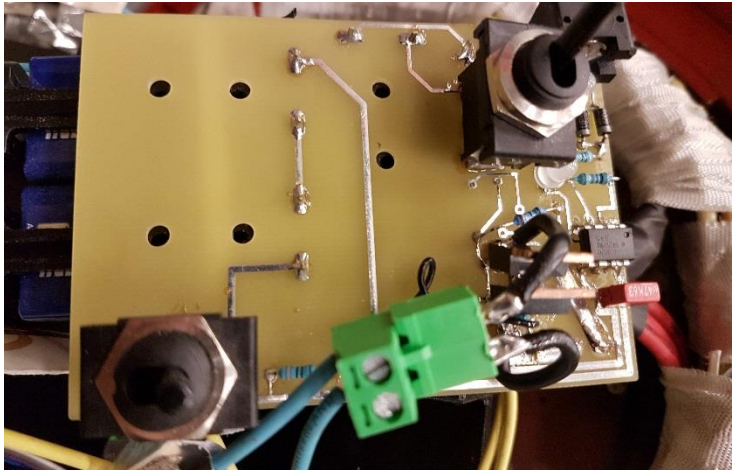


Figure 7.3 Photo of the short-circuit devise.

The in-wheel motor is set to operate as a generator with a pure resistive load for a fair comparison with the simulations results presented in Chapter 6. The mechanical input power is provided by speed controlled DC-machine, whose reference speed is manually selected by an analog control panel. The power rating of the DC-machine is several times larger than the power rating of the in-wheel motor, allowing to consider it as an infinite mechanical power source.

To measure the machine vibrations, the breakout board of the accelerometer BOSCH BMA180 [41] has been used. Even though the selected accelerometer is capable of measuring the acceleration in three axis, due of the limited data transfer rate of the measurement system data from only one axis is retrieved in order to speed up the sampling rate. The sampling rate limit is imposed by the data transfer rate between the measurement system and the computer where the data is stored. An additional limit imposed by the limited data rate is that the number of accelerometers that can be used simultaneously is only one, as the sampling rate for sensor would become too low otherwise. As a result, the circumferential order of the measured vibrations cannot be determined in this experimental setup.

As a result, the sampling frequency used during the vibration measurements is just below 900 Hz . As shown in Section 6.3, the fault has the largest impact on the electromagnetic forces at two times the electrical frequency of the machine. For the in-wheel machine used in the experimental setup (which has 8 pole-pairs), this means that the rotational speed of the machine should not exceed 1680 rpm in order to keep the two times fundamental electrical frequency below the 450 Hz limit imposed by the sampling frequency. However, in order to limit the induced fault current, the speed needs to be limited to a maximum of 500 rpm. As a result, vibrations up to six times the fundamental electrical frequency are included in the vibrational measurements.

In order to obtain a stiff connection between the accelerometer and the stator frame, the accelerometer is glued directly onto the machine frame using epoxy. The accelerometer is placed so that the direction of the axis used for vibration measurements is aligned with the radial direction of the machine. In order to minimize the impact of the gravity force on the measurement, the selected radial direction is in parallel with the laboratory floor. Figure 7.4 presents a picture of the accelerometer installed on the machine frame and the radial direction in which the acceleration is measured.

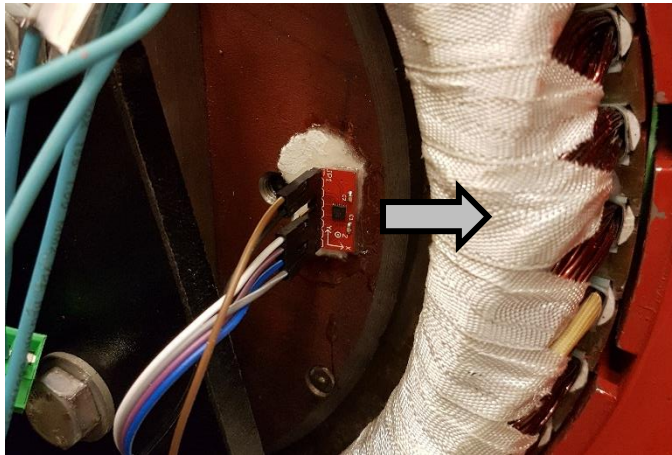


Figure 7.4 Picture of the accelerometer's glued position on the machine frame and the arrow presents the radial direction in which the acceleration is measured.

7.2 Experimental results

As mentioned earlier, the implemented laboratory setup allows to short circuit up to four turn of one strand. Since one phase of the machine is constituted by 176 turns in each parallel strand, the maximum fault that can be achieved is 2.3% of one branch, i.e. less than 0.5% of the total phase winding. Due to this low fraction, the fault has a non-measurable impact on the machine currents for the operational conditions that can be tested without damaging the experimental setup. The impact of the faults on the machine's currents is therefore not presented. However, this motivates that there is a need for a detection method which does not rely on the impact on the electrical quantities.

The experimental setup is therefore utilized to measure if the fault causes a measurable change in the amplitude of the vibrations of the in-wheel machine's frame. In order to verify the effectiveness of using vibrations as a detection method, the measurements are performed under different system's operational conditions: different number of short-circuited turns, open-circuit operation and generator operation, and different machine speeds. Figure 7.5 presents the components with greatest amplitude from the Fourier analysis of the measured vibrations while the

machine is rotating at 500 rpm. For this set of results, the machine is operated in open-circuit (no electrical load connected to the stator of the machine). From the obtained experimental result, when no faults are applied the dominating vibration for the in-wheel machine is at about six times the fundamental electrical frequency. This is no longer true once the turn-to-turn fault is introduced. As it can be observed, the fault introduces vibrations at the two times the fundamental frequency and does not significantly impact the higher order components, in agreement with the analysis conducted in Section 6.3.

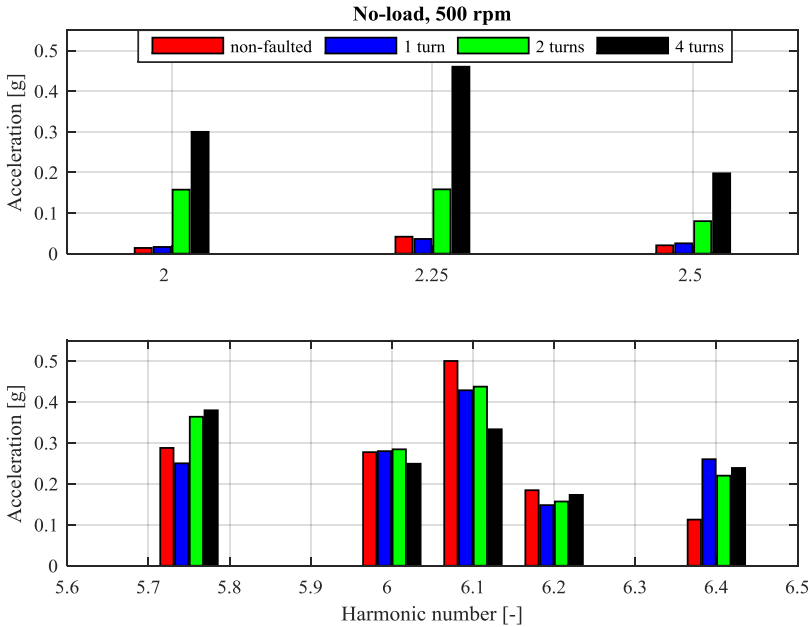


Figure 7.5 Measured stator vibrations during no-load operation while the machine is rotating with 500 rpm.

Note however that non-integer harmonics (such as 2.25 times the fundamental component) are now present; these harmonics were not presented in the obtained simulation results presented in Section 6.3. This discrepancy is due to the fact that the models presented in the previous chapters assume that the machines have a perfectly circular shaped stator and rotor, leading to a homogeneous air gap. This is not true for the in-wheel motor used in this experimental setup, as the rotor presents a slightly oval shape that causes the air-gap to be non-symmetrical. This non-homogenous air-gap distance has been verified using a feeler gauge. To verify that the non-integer harmonics are caused by the non-constant air-gap length, the small FEM model of the faulted machine presented in Section 4.2 has been altered to in order to present an oval shaped rotor, where the small model was selected because it is less computational demanding and re-shaping of the rotor simpler because of its smaller size. Figure 7.6 presents the results from the 2D-Fourier analysis of normal force for the FEM model with an oval rotor when one turn has been short circuited.

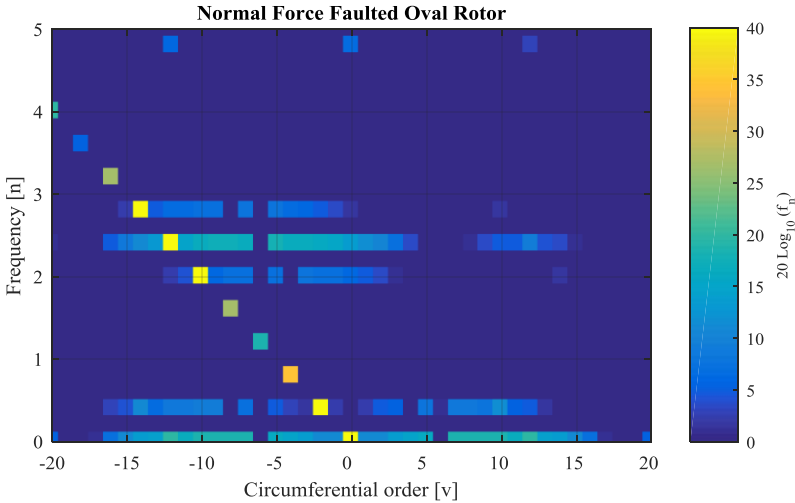


Figure 7.6 Results from a 2D-Fourier analysis of normal force for the small FEM model with an oval shaped rotor.

The obtained simulation results clearly show that a machines with an oval shaped rotors presents normal force density components at non-integer harmonics at various circumferential orders. In addition, a turn-to-turn fault (as for the case of the perfectly circular rotor) introduces additional components with new circumferential orders at frequencies that are present also in the non-faulted machine. From the figure, is can be seen that the non-integer harmonics for the non-faulted case can be of high circumferential order, and are therefore not likely to cause any measurable vibrations; vibrations will be experienced when the fault is applied, due to the introduction of new components with lower circumferential order. This agrees well with the obtained laboratory results under open-circuit conditions. Note anyway that the additional vibrations introduced by the fault in the experimental setup do not perfectly match with the frequency content obtained through the FEM simulation; this is most probably due to the fact that the rotor of the in-wheel machine is not perfectly oval as in the case of the simulation.

In order to verify that the fault leads to a noticeable impact on the machine vibrations during loaded conditions, the machine is loaded with a pure resistive load while rotating at the same speed. The resulting Fourier analysis of the measured vibrations is presented in Figure 7.7. For the loaded case, vibrations at two times the electrical frequency are present even for the non-faulted condition; however, the amplitude of these vibrations clearly increases when the fault is applied. This agrees well with the simulations results and the example presented in (6.10), where more normal force components (presumably of low circumferential order) are introduced at this specific frequency. The non-integer harmonics are still present under loaded operation; this is

not surprising, since the geometry of the machine is not affected by its electrical loading.

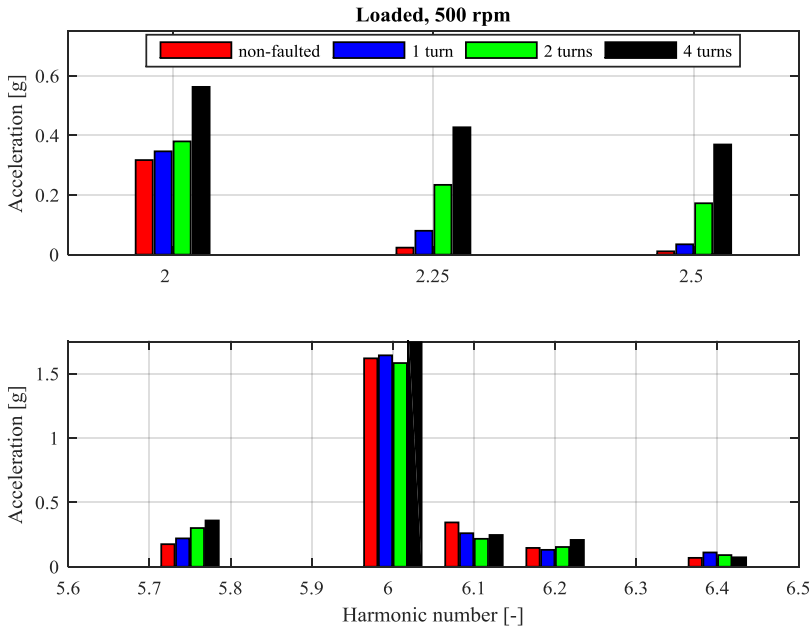


Figure 7.7 Fourier analysis of the measured stator vibrations while the machine is rotating with 500 rpm during generator operation with a pure resistive load.

In order to verify that the vibrations introduced by fault at two times the fundamental frequency are not dependent on the machine's speed, another set of experiments has been performed while the machine is rotating at 300 rpm. The reduction of the machine speed results in a lower induced fault current, which should lead to a reduction of the normal force density. On the other hand, a reduced speed also means that the actual frequencies of the vibrations in the time domain are altered, which may lead to a different reaction from the machine's mechanical frame. It is therefore possible that the amplitude of a vibration at a certain frequency increases even though the speed and the normal force density are reduced. Figure 7.8 presents the results from the Fourier analysis of the vibrations while the machine is rotating at 300 rpm.

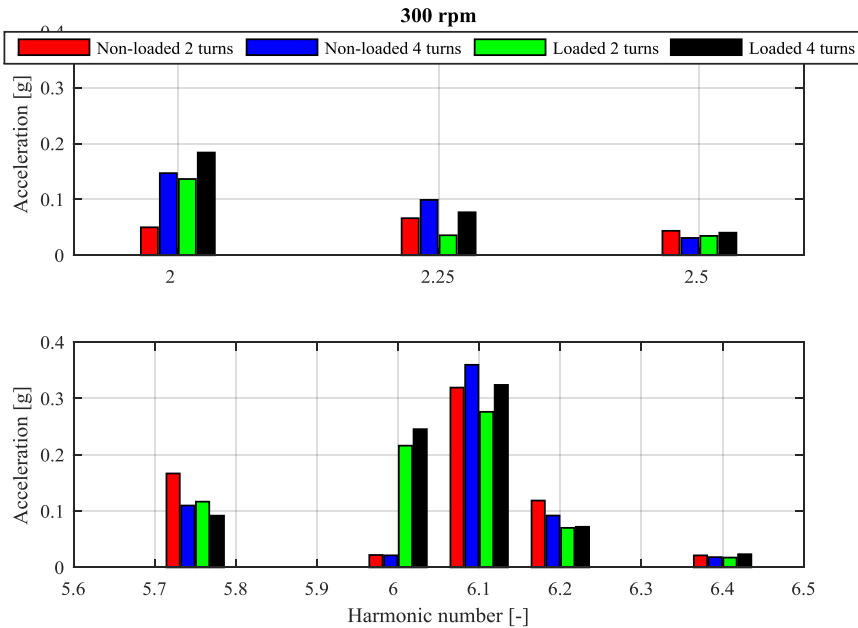


Figure 7.8 Measured stator vibrations at 300 rpm, during both no-load operation and during generator operation with a pure resistive load.

The amplitude of the vibrations are overall reduced when the speed is decreased, and the loading of the machine has a noticeable impact on the vibrations at two times the fundamental component and at six times the fundamental. Note that also for this speed the fault has a noticeable impact on the amplitude of the vibrations at two times the fundamental frequency, as the amplitude of the vibrations increases with the number of short-circuited turns for both loaded and non-loaded operation. The vibrations at six times the fundamental seem to mainly depend on load current and are not affected by the fault. This trend is also observable during higher speed operation. In addition, this trend agrees with the simulation results as only a very small portion of the in-wheel machine is short-circuited and it is operating at a low speed (compared to rated), making the likelihood of the fault introducing new measurable component at higher frequencies very low.

To summarize, the obtained laboratory results present are comparable, with the given limitations, to the simulation results presented in Section 6.3; the amplitude of the vibrations at two times the fundamental component increases in the event of a turn-to-turn fault and the amplitude of the vibrations increases with the number of short-circuited turns. However, the measurements shows that the amplitude of the vibrations also depends on the machine's electrical loading. It is therefore necessary to acquire knowledge of the amplitude of the vibrations for the non-faulted machine to be able use vibrational measurements as a detection method for turn-to-turn faults, especially if early detection (i.e., only a low number of turns are short-circuited) is

desired. The laboratory results presented in this section also indicate that it can be worth to monitor a wider range of harmonics, in order to take advantage of any vibration introduced by manufacturing imperfections of the machine.

7.3 Chapter summery

This chapter presented the experimental setup which included a purposely rewound PMSM, where the machine was rewound in order to provide access to some of the turns in order to short-circuit up to four turns in controlled manner. The measurement results acquired using the experimental setup agreed with the results presented in Section 6.3. However, because the rotor of the machine used in the experimental setup does not have a perfect circular shape as the machines modeled in previous chapters, vibrations at non-integer multiples of the fundamental electrical component are present in the experimental step but not in the simulations results presented in Section 6.3. But in essence, the simulation results and the measured results agrees and machine vibration can therefore be effectively be used as a detection method for turn-to-turn faults, even when only a small fraction of a phase is short-circuited.

The following chapter will conclude this thesis and presents some possible suggestions for future work.

Chapter 8

Conclusion and future work

This chapter summarizes and concludes this thesis and suggests some possible future research topics within the presented subject.

8.1 Conclusion

In this thesis, an analytical model of a PMSM with a turn-to-turn fault has been derived from a generic analytical PMSM model. The presented analytical models have been successfully verified using FEM models, showing very good agreement between the two models. The purpose of the presented analytical model has been to obtain a proper procedure for the derivation of a PMSM that could accurately represent the electrical behavior of the machine with turn-to-turn fault, in order for the model to be applicable for various applications. The benefit of having an analytical model is that it requires considerable less computational time as compared with FEM models. In particular, here the model of the faulted machine has been used to investigate if the turn-to-turn fault causes any characteristic change in the machine behavior that could be exploited for fault detection purposes. It has been observed that the harmonic content of the current is affected by the fault, and by monitoring the current in the rotating reference frame the fault could be detected by analyzing variations in the current's harmonic spectra. However, the variations observed in the current harmonics are fairly small, especially if only a few turns are short-circuited. Therefore, it can be concluded that the monitoring of the harmonic currents might not be a practical way to detect this kind of fault conditions, especially if early fault detection is desired.

As PMSMs require converters to be able to operate (other than uncontrolled generator mode), the analytical model has been simulated to operate with an ideal converter, in order to investigate the converters controller's reaction to the fault. Through the implemented cascade controller, it has been shown that the presence of a converter connected to the machine's terminals has an impact on the monitored signals, leading to more noticeable differences between the non-faulted and the faulted machine characteristics. This difference is particularly evident in the machine's power. Therefore, the presence of the converter allows to more effectively detect a fault condition. Furthermore, it allows for a wider range of signals and estimates to be adopted for monitoring purpose, such as the shift in the voltage phase angles. However, it has been shown that monitoring of electrical quantities might not be effective when aiming at an early detection of a turn-to-turn fault. This difficulty, mainly due to the small amplitude difference in the measured signals, would be even more evident if the machine is operated in a noisy environment.

In order to understand if the mechanical vibrations of the machine could be a more effective fault indicator, the FEM models has been used to investigate the impact of the fault on the air-gap flux density and the resulting forces. Simulation results show that even a single turn fault introduces additional space harmonics at two times the fundamental frequency with low circumferential order, which are likely to cause a measurable impact on the machine vibrations, and the machine's vibrations will increase with the number of faulted turns.

The increase in machine vibrations in the event of a turn-to-turn fault has been verified in an experimental setup. Due to practical limitations in the experimental setup, severe fault conditions could not be tested. However, for the tested operational conditions a measureable increase in the machine vibration at two times the fundamental frequency has been observed, in agreement with the result obtained through the simulation model.

Because of the limited resources in the experimental setup, the presence of new circumferential order components in the event of a turn-to-turn fault could not be verified. If the circumferential order of the vibrations where to be measured, it will require several synchronized sensors, and because of the amount of sensors the system can more easily be affected by disturbances, such as sensor misalignment, delays or measurement noise. Any of these disturbances is likely to reduce the accuracy and reliability of the detection method.

8.2 Future work

Below are some suggestions of possible future works that have not been included in the work presented in this thesis:

- Derive a model that is able to dynamically describe the transition between non-faulted and faulted state.
- Couple the model of the faulted machine to a thermal model, in order to be able to estimate the heat produced by the fault. This information can be used as a feedback to the faulted model, in order to update the resistive quantities and thereby acquire information for better estimation of the remaining time before the insulation of neighboring turns fails.
- Use the proposed analytical model to further investigate how different control strategies impact the behavior of the machine under fault condition.
- Improve the laboratory setup utilized in this work to further verify the obtained simulation results. In particular, it can be of high interest to include more sensors to verify the circumferential order of the vibrations. In addition, the simulated converter operation results and the effects of the circulating currents for machines with parallel windings can be verified.

Other possible future work, less closely related to the work presented in this thesis, can be to analyze how a turn-to-turn fault impacts other machine types, such as a reluctance machine, which does not have a rotor excitation.

The focus of this thesis has been on the development of a method that is able to detect the occurrence of a turn-to-turn fault, but what actions should be taken once a fault has been detected has not been addressed. Different strategies to be taken after the faults detection should be investigated and compared, also based on the specific application. For example, if continued operation is possible (though at reduced capacity), a proper strategy might provide an effective scheduling of the intervention for repair, thus reducing the possible economical loss. This might be of particular importance for wind turbines located in remote areas or for offshore applications.

A proper fault detection method should, ideally, be selective and allow the operators to identify without doubt the specific kind of fault. It would therefore be interesting to understand if other type of faults might lead to similar machine vibrations and if still there are characteristics in the monitored signals that allow the differentiating of the different fault conditions.

References

- [1] B. Lu, Y. Li, X. Wu, and Z. Yang, "A review of recent advances in wind turbine condition monitoring and fault diagnosis," 2009
- [2] J. K. Kaldellis and D. Zafirakis, "The wind energy (r)evolution: A short review of a long history," *Renewable Energy*, vol. 36, pp. 1887-1901, 2011.
- [3] D. Bang, H. Polinder, G. Shrestha, and J. A. Ferreira, "Review of generator systems for direct-drive wind turbines", presented at the EWEC conference, Brussels, 2008.
- [4] E. Hau, *Wind turbines: Fundamentals, Technologies, Application, Economics*, 2nd ed. Berlin:Springer, 2006
- [5] Windmeasurementinternational, "Operational and Maintenance Costs for Wind Turbines" Online, Available: <http://www.windmeasurementinternational.com/wind-turbines/om-turbines.php> Accessable:2016-11-11
- [6] S. Grubic, J. M. Aller, B. Lu, and T. G. Habetler, "A survey on testing and monitoring methods for stator insulation systems of low-voltage induction machines focusing on turn insulation problems," *IEEE Transactions on Industrial Electronics*, vol. 55, pp. 4127-4136, 2008.
- [7] A. D. Hansen, N. A. Cutululis, H. Markou, and P. E. Sørensen, "Impact of fault ride-through requirements on fixed-speed wind turbine structural loads," *Wind Energy*, vol. 14, pp. 1-11, 2011.
- [8] Global Wind Energy Consil, "GWEC-Global-Wind-2015-Report", 2016
- [9] G. M. Joselin Herbert, S. Iniyar, E. Sreevalsan, and S. Rajapandian, "A review of wind energy technologies," *Renewable and Sustainable Energy Reviews*, vol. 11, pp. 1117-1145, 2007.
- [10] MHI Vestas Offshore Wind, "V164-8.0 MW breaks world record for wind energy production"
- [11] F. Spinato, P. J. Tavner, G. J. W. Van Bussel, and E. Koutoulakos, "Reliability of wind turbine subassemblies," *IET Renewable Power Generation*, vol. 3, pp. 387-401, 2009.
- [12] F. Besnard, K. Fischer, and L. Bertling, "Reliability-Centred Asset Maintenance - A step towards enhanced reliability, availability, and profitability of wind power plants," 2010.

- [13] B.F. Sørensen, E. Jørgensen, C. P. Debel, F. M. Jensen, H. M. Jensen, T. K. Jacobsen, and K. M. Halling, "Improved design of large wind turbine blade of fibre composites based on studies of scale effects (Phase 1)," Risø-R-1390(EN) September 2004
- [14] C. C. Ciang, J. R. Lee, and H. J. Bang, "Structural health monitoring for a wind turbine system: A review of damage detection methods," *Measurement Science and Technology*, vol. 19, 2008
- [15] G. J. W. v. B. P J Tavner, F Spinato "Machine and Converter Reliabilities in Wind Turbines " presented at the IEE 2nd International Conference on Power Electronics, Machine & Drives, Dublin, 2006.
- [16] S. Yang, D. Xiang, A. Bryant, P. Mawby, L. Ran, and P. Tavner, "Condition monitoring for device reliability in power electronic converters: A review," *IEEE Transactions on Power Electronics*, vol. 25, pp. 2734-2752, 2010
- [17] M. Held, P. Jacob, G. Nicoletti, P. Scacco, and M. H. Pöech, "Fast power cycling test for IGBT modules in traction application," 1997, pp. 425-430.
- [18] B. Lu and S. K. Sharma, "A literature review of IGBT fault diagnostic and protection methods for power inverters," *IEEE Transactions on Industry Applications*, vol. 45, pp. 1770-1777, 2009.
- [19] T. B. Hammarström, Tord; Blenow, Jörgen; Gubanski, Stanislaw, "PARTIAL DISCHARGES IN A STATOR UNDER SYNTHESIZED VOLTAGE WAVEFORMS," presented at the Proceedings of the 18th International Symposium on High Voltage Engineering 2013, 2013.
- [20] K. Alewine and W. Chen, "A review of electrical winding failures in wind turbine generators," 2011, pp. 392-397.
- [21] J. A. Farooq, T. Raminosoa, A. Djerdir and A. Miraoui "Modelling and simulation of stator winding inter-turn faults in permanent magnet synchronous motors", *COMPEL: The International Journal for Computation and Mathematics in Electrical and Electronic Engineering*, Vol. 27 No. 4, 2008, pp. 887-896
- [22] B. Vaseghi, N. Takorabet, F. Meibody-Tabar, A. Djerdir, J. Farooq, and A. Miraoui, "Modeling and characterizing the inter-turn short circuit fault in PMSM", *Electric Machines & Drives Conference (IEMDC)*, 2011 IEEE International, 2011, pp. 551-556
- [23] H. Saavedra, J.-R. Riba and L. Romeral "Detection of interturn faults in PMSMs with different winding configurations" *Energy Conversion and Management*, March 2014

- [24] F. Wu, P. Zheng, T.M. Jahns “Analytical modeling of inter-turn short circuit for multiphase fault-tolerant PM machines with fractional-slot concentrated windings”, *Energy Conversion Congress and Exposition (ECCE)*, September 2015 IEEE
- [25] J. Dusek, P. Arumugam, C. Brunson, E. K. Amankwah, T. Hamiti, and C. Gerada “Impact of Slot/Pole Combination on Inter-Turn Short-Circuit Current in Fault-Tolerant Permanent Magnet Machines” *IEEE transactions on magnetics*, vol. 52, no. 4, april 2016
- [26] B-G. Gu, J-H. Choi and I-S. Jung, “Development and Analysis of Interturn Short Fault Model of PMSMs With Series and Parallel Winding Connection”, *IEEE Transactions On Power Electronics*, vol. 29, no. 4, April 2014
- [27] L. Belguerras, J. Arellano-Padilla, P. Arumugam, T. Hamiti, S. Mezani and C Gerada “ Non-linear circuit based model of permanent magnet synchronous machine under interturn fault: a simple approach based on healthy machine data” *IET Electr. Power Appl.*, 2016, Vol. 10, Iss. 6, pp. 560–570
- [28] M. Taghipour-GorjiKolaie, S. M. Razavi, M. A. Shamsi-Nejad, and A. Darzi, "Inter-turn stator winding fault detection in PMSM using magnitude of reactive power," in *Computer Applications and Industrial Electronics (ICCAIE)*, 2011 IEEE International Conference on, 2011, pp. 256-261
- [29] J. Rosero, A. G. Espinosa, J. Cusido, J. A. Ortega, and L. Romeral, "Simulation and Fault Detection of Short Circuit Winding in a Permanent Magnet Synchronous Machine (PMSM) by means of Fourier and Wavelet Transform," in *Instrumentation and Measurement Technology Conference Proceedings, 2008. IMTC 2008. IEEE*, 2008, pp. 411-416
- [30] G. Bon-Gwan, C. Jun-Hyuk, and J. In-Soung, "A dynamic modeling and a fault detection scheme of a PMSM under an inter turn short," in *Vehicle Power and Propulsion Conference (VPPC), 2012 IEEE*, 2012,
- [31] L. Harnefors, *Control of Power Electronic Converters and Variable-Speed Drives*.
- [32] A. Rahideh, M. Mardaneh and T. Korakianitis, "Analytical 2-D Calculations of Torque, Inductance, and Back-EMF for Brushless Slotless Machines With Surface Inset Magnets," in *IEEE Transactions on Magnetics*, vol. 49, no. 8, pp. 4873-4884, Aug. 2013.

- [33] T. D. Strous, H. Polinder and J. A. Ferreira, "Inductance calculations for PM machines with concentrated windings," *2011 IEEE International Electric Machines & Drives Conference (IEMDC)*, Niagara Falls, ON, 2011, pp. 447-452.
- [34] ANSYS Inc, Online, Available:
<http://www.ansys.com/Products/Electronics/ANSYS-Maxwell>
- [35] ANSYS Inc, Online, Available:
<http://www.ansys.com/products/Systems/ANSYS-Simplorer>
- [36] P. Roshanfekr "Design and assessment of HVDC off-shore wind turbine generator" *Department of Energy and Environment, Chalmers University of Technology*, ISBN 978-91-7597-271-8
- [37] M. Bongiorno, J. Svensson, and A. Sannino, "Effect of sampling frequency and harmonics on delay-based phase-sequence estimation method," *IEEE Transactions on Power Delivery*, vol. 23, pp. 1664-1672, 2008.
- [38] L. Ängquist, M. Bongiorno, "Auto-normalizing Phase-Locked Loop for grid-connected converters", *Energy Conversion Congress and Exposition, 2009. ECCE 2009. IEEE*, Sept. 2009
- [39] C. W. Jacek F . Gieras and J. C. Lai, *Noise of Polyphase Electric Motors*. CRC Press, 2005.
- [40] M. Islam, R. Islam, and T. Sebastian, "Noise and vibration characteristics of permanent magnet synchronous motors using electromagnetic and structural analyses", *Energy Conversion Congress and Exposition (ECCE)*, Sept 2011, pp. 3399–3405.
- [41] BMA180 Digital, triaxial acceleration sensor, Bosch Sensortec Online, Available: http://www.geeetech.com/wiki/index.php/BMA180_Triple_Axis_Accelerometer_Breakout

Appendix A

Moving from stationary to rotating reference frame

A widely used mathematical transformation in the electrical engineering discipline is the transformation from the stationary to the rotating reference frame. This makes an oscillating quantity at the transformation frequency appear as a DC quantity. The mathematical transformation matrix for a three phase system is

$$T_1(\theta) = K \frac{2}{3} \begin{bmatrix} \cos \theta & \cos\left(\theta - \frac{2\pi}{3}\right) & \cos\left(\theta + \frac{2\pi}{3}\right) \\ -\sin \theta & -\sin\left(\theta - \frac{2\pi}{3}\right) & -\sin\left(\theta + \frac{2\pi}{3}\right) \\ \frac{1}{3} & \frac{1}{3} & \frac{1}{3} \end{bmatrix} \quad (\text{A.1})$$

where θ is the transformation angle related to the rotational speed of the rotating reference frame and K is a scaling constant. By selecting K to 1 the transformation becomes amplitude invariant.

The inverse of the transformation matrix is

$$T_1^{-1}(\theta) = K \begin{bmatrix} \cos \theta & -\sin \theta & 1 \\ \cos\left(\theta - \frac{2\pi}{3}\right) & -\sin\left(\theta - \frac{2\pi}{3}\right) & 1 \\ \cos\left(\theta + \frac{2\pi}{3}\right) & -\sin\left(\theta + \frac{2\pi}{3}\right) & 1 \end{bmatrix} \quad (\text{A.2})$$

If the zero sequence component is neglected the transformation matrix becomes

$$T(\theta) = K \frac{2}{3} \begin{bmatrix} \cos \theta & \cos\left(\theta - \frac{2\pi}{3}\right) & \cos\left(\theta + \frac{2\pi}{3}\right) \\ \sin \theta & \sin\left(\theta - \frac{2\pi}{3}\right) & \sin\left(\theta + \frac{2\pi}{3}\right) \end{bmatrix} \quad (\text{A.3})$$

with the inverse

$$T^{-1}(\theta) = K \begin{bmatrix} \cos \theta & \sin \theta \\ \cos\left(\theta - \frac{2\pi}{3}\right) & \sin\left(\theta - \frac{2\pi}{3}\right) \\ \cos\left(\theta + \frac{2\pi}{3}\right) & \sin\left(\theta + \frac{2\pi}{3}\right) \end{bmatrix} \quad (\text{A.4})$$

For a balanced frequency component with equal speed as the rotating reference frame the transformed components becomes

$$\begin{aligned}
& K \frac{2}{3} \begin{bmatrix} \cos \theta & \cos\left(\theta - \frac{2\pi}{3}\right) & \cos\left(\theta + \frac{2\pi}{3}\right) \\ \sin \theta & \sin\left(\theta - \frac{2\pi}{3}\right) & \sin\left(\theta + \frac{2\pi}{3}\right) \end{bmatrix} \begin{bmatrix} A_a \cos \theta \\ A_b \cos\left(\theta - \frac{2\pi}{3}\right) \\ A_c \cos\left(\theta + \frac{2\pi}{3}\right) \end{bmatrix} = \\
& K \frac{1}{3} \begin{bmatrix} A_a + A_b + A_c + A_a \cos 2\theta + A_b \cos\left(2\theta - \frac{4\pi}{3}\right) + A_c \cos\left(2\theta + \frac{4\pi}{3}\right) \\ A_a \sin 2\theta + A_b \sin\left(2\theta - \frac{4\pi}{3}\right) + A_c \sin\left(2\theta + \frac{4\pi}{3}\right) \end{bmatrix} \quad (\text{A.5})
\end{aligned}$$

If $A_a = A_b = A_c = A$ then (A.5) become $\begin{bmatrix} AK \\ 0 \end{bmatrix}$ since the double frequency component is perfectly symmetric. Similar calculations can be done for the harmonics. If they are balanced they will only appear at one frequency where the other will be canceled due to symmetry.

Vector representation of three phase quantities

A three-phase positive system constituted by the three quantities $x_1(t)$, $x_2(t)$ and $x_3(t)$ can be transformed into a vector in a complex reference frame, usually called $\alpha\beta$ -frame, by applying the transformation defined by:

$$\underline{x} = x_\alpha(t) + jx_\beta(t) = K \cdot \left[x_1(t) + x_2(t) \cdot e^{j\frac{2}{3}\pi} + x_3(t) \cdot e^{j\frac{4}{3}\pi} \right] \quad (\text{A.6})$$

where the factor K is usually taken equal to $\sqrt{\frac{3}{2}}$ for ensuring power invariance between the two systems. Equation (A.1) can be expressed as a matrix equation:

$$\begin{bmatrix} x_\alpha(t) \\ x_\beta(t) \end{bmatrix} = \mathbf{C}_{23} \begin{bmatrix} x_1(t) \\ x_2(t) \\ x_3(t) \end{bmatrix} \quad (\text{A.7})$$

where:

$$\mathbf{C}_{23} = \begin{bmatrix} \sqrt{\frac{2}{3}} & -\frac{1}{\sqrt{6}} & -\frac{1}{\sqrt{6}} \\ 0 & \frac{1}{\sqrt{2}} & -\frac{1}{\sqrt{2}} \end{bmatrix} \quad (\text{A.8})$$

The inverse transformation is given by:

$$\begin{bmatrix} x_1(t) \\ x_2(t) \\ x_3(t) \end{bmatrix} = \mathbf{C}_{32} \begin{bmatrix} x_\alpha(t) \\ x_\beta(t) \end{bmatrix} \quad (\text{A.9})$$

where:

$$\mathbf{C}_{32} = \begin{bmatrix} \sqrt{\frac{2}{3}} & 0 \\ -\frac{1}{\sqrt{6}} & \frac{1}{\sqrt{2}} \\ -\frac{1}{\sqrt{6}} & -\frac{1}{\sqrt{2}} \end{bmatrix} \quad (\text{A.10})$$

This holds under the assumption that the sum of the three quantities is zero. Otherwise, there will also be a constant (zero-sequence) component. In the latter case, Eqs.(A.7) and (A.9) become:

$$\begin{bmatrix} x_\alpha(t) \\ x_\beta(t) \\ x_o(t) \end{bmatrix} = \mathbf{C}_{23o} \begin{bmatrix} x_1(t) \\ x_2(t) \\ x_3(t) \end{bmatrix} \quad (\text{A.11})$$

and for the inverse transformation:

$$\begin{bmatrix} x_1(t) \\ x_2(t) \\ x_3(t) \end{bmatrix} = \mathbf{C}_{32o} \begin{bmatrix} x_\alpha(t) \\ x_\beta(t) \\ x_o(t) \end{bmatrix} \quad (\text{A.12})$$

with the two matrixes given by:

$$\mathbf{C}_{23o} = \begin{bmatrix} \sqrt{\frac{2}{3}} & -\frac{1}{\sqrt{6}} & -\frac{1}{\sqrt{6}} \\ 0 & \frac{1}{\sqrt{2}} & -\frac{1}{\sqrt{2}} \\ \frac{1}{\sqrt{6}} & \frac{1}{\sqrt{6}} & \frac{1}{\sqrt{6}} \end{bmatrix} \quad (\text{A.13})$$

and

$$\mathbf{C}_{32o} = \begin{bmatrix} \sqrt{\frac{2}{3}} & 0 & \frac{1}{\sqrt{6}} \\ -\frac{1}{\sqrt{6}} & \frac{1}{\sqrt{2}} & \frac{1}{\sqrt{6}} \\ -\frac{1}{\sqrt{6}} & -\frac{1}{\sqrt{2}} & \frac{1}{\sqrt{6}} \end{bmatrix} \quad (\text{A.14})$$

Voltage vectors for unsymmetrical three-phase systems

The phase voltages for a three-phase system can be written as:

$$\begin{aligned}
 e_a(t) &= \hat{e}_a(t) \cdot \cos(\omega t - \varphi_a) \\
 e_b(t) &= \hat{e}_b(t) \cdot \cos(\omega t - \frac{2}{3}\pi - \varphi_b) \\
 e_c(t) &= \hat{e}_c(t) \cdot \cos(\omega t - \frac{4}{3}\pi - \varphi_c)
 \end{aligned}
 \tag{A.15}$$

where $\hat{e}_a(t)$, $\hat{e}_b(t)$ and $\hat{e}_c(t)$ are the amplitudes of the three-phase voltages, φ_a , φ_b and φ_c are the phase angles of the three-phase voltages, and ω is the angular frequency of the system.

If the amplitudes $\hat{e}_a(t)$, $\hat{e}_b(t)$ and $\hat{e}_c(t)$ are unequal, the voltage vector can be written as the sum of two vectors rotating in opposite directions and interpreted as positive- and negative-sequence vectors:

$$\underline{e}^{(\alpha\beta)}(t) = E_p e^{j(\omega t + \varphi_p)} + E_n e^{-j(\omega t + \varphi_n)}
 \tag{A.16}$$

where E_p and E_n are the amplitudes of positive- and negative-sequence vectors, respectively, and the corresponding phase angles are denoted by φ_p and φ_n . To determine amplitudes and phase angles of positive- and negative-sequence vectors in Eq. (A.19), a two-step solving technique can be used. First, the phase shifts are set to zero, so that the amplitudes E_p and E_n can easily be detected. In the next step, the phase shifts φ_p and φ_n are determined.

Appendix B

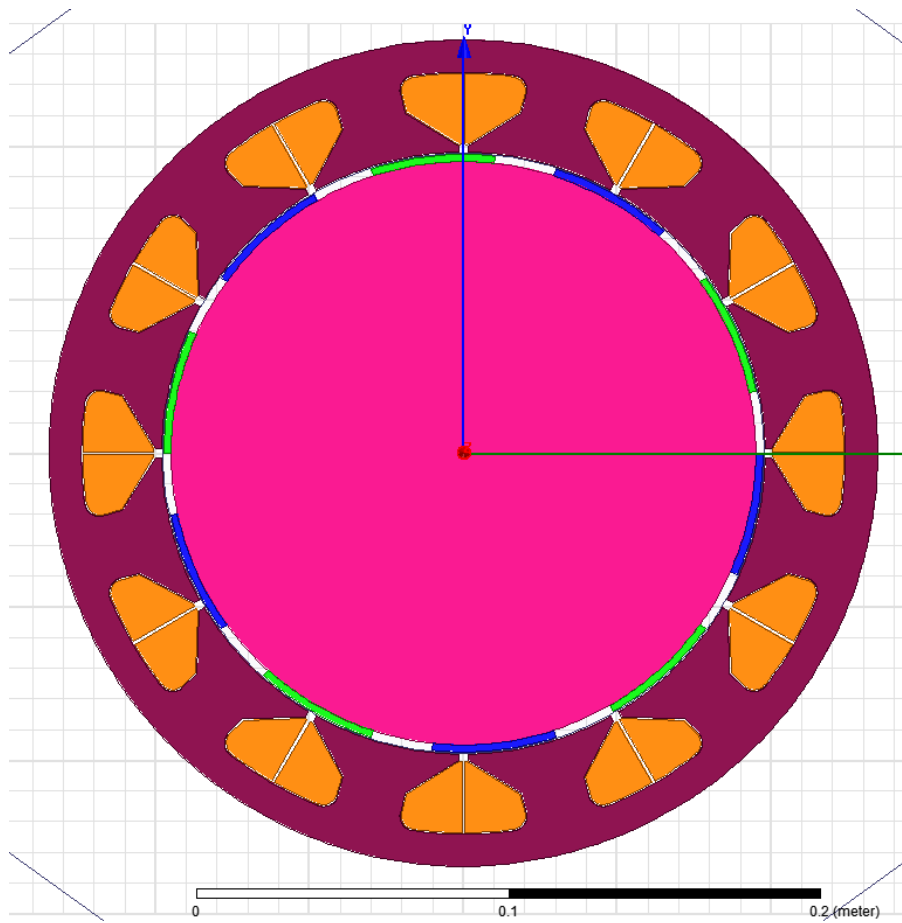
Small FEM Machine Parameters

Machine parameters

R_s	1.6 m Ω
R_f	20 m Ω
L	292 μ H
M	-12 μ
M_{af}	12.6 μ H
M_{bf}	0.12 μ H
M_{cf}	-1.35 μ H
L_f	2.75 μ H
Ψ_{pm}	0.068
Pole-pairs	5
f_0	125 Hz

Machine geometry

Stator diameter	270 mm
Rotor diameter	190 mm
Airgap	3.1 mm
Magnet height	2.3 mm
Magnet length	80 mm
Stator back	10.5 mm
Shoe height	2 mm
Tooth width	21 mm
Slot width	38 mm
Stack length	109 mm



Appendix C

Parameter values of the A matrix in (3.77) and the B matrix in (3.78)

$$A[1,1] = \frac{\text{Lf}(-L + M)\text{Rs} + \text{K1K9}(L - M)\text{Cos}[\text{K10} - \text{thetaR}]\text{Cos}[\text{K2} - \text{thetaR}] + \text{K1K5}\text{Cos}[\text{K4} - \text{thetaR}]((-L + M)\text{wr}\text{Cos}[\text{K2} - \text{thetaR}] + \text{Rs}\text{Cos}[\text{K4} - \text{thetaR}])}{(L - M)(\text{Lf}(L - M) - \text{K1K5}(\text{Cos}[\text{K2} - \text{thetaR}]^2 + \text{Cos}[\text{K4} - \text{thetaR}]^2))}$$

$$A[1,2] = -\frac{2\text{K1K9}(L - M)\text{Cos}[\text{K12} - \text{thetaR}]\text{Cos}[\text{K2} - \text{thetaR}] + 2\text{K1K5}\text{Rs}\text{Cos}[\text{K2} - \text{thetaR}]\text{Cos}[\text{K4} - \text{thetaR}] + (L - M)\text{wr}(\text{K1K5} - 2\text{LLf} + 2\text{LFM} + \text{K1K5}\text{Cos}[2(\text{K4} - \text{thetaR})])}{2(L - M)(\text{Lf}(L - M) - \text{K1K5}(\text{Cos}[\text{K2} - \text{thetaR}]^2 + \text{Cos}[\text{K4} - \text{thetaR}]^2))}$$

$$A[1,3] = \frac{2\text{Rssigma}(\text{Lf}(L - M) - \text{K1K5}\text{Cos}[\text{K4} - \text{thetaR}]^2)\text{Cos}[\text{thetaR}] + \text{K1}\text{Cos}[\text{K2} - \text{thetaR}](3(L - M)(\text{Rf} + \text{Rssigma}) - 2\text{K5}\text{Rssigma}\text{Cos}[\text{K4} - \text{thetaR}])\text{Sin}[\text{thetaR}]}{3(L - M)(\text{Lf}(L - M) - \text{K1K5}(\text{Cos}[\text{K2} - \text{thetaR}]^2 + \text{Cos}[\text{K4} - \text{thetaR}]^2))}$$

$$A[2,1] = \frac{-\text{Lf}(L - M)^2\text{wr} + \text{K1K5}(L - M)\text{wr}\text{Cos}[\text{K2} - \text{thetaR}]^2 + \text{K1}(\text{K9}(L - M)\text{Cos}[\text{K10} - \text{thetaR}] - \text{K5}\text{Rs}\text{Cos}[\text{K2} - \text{thetaR}])\text{Cos}[\text{K4} - \text{thetaR}]}{(L - M)(\text{Lf}(L - M) - \text{K1K5}(\text{Cos}[\text{K2} - \text{thetaR}]^2 + \text{Cos}[\text{K4} - \text{thetaR}]^2))}$$

$$A[2,2] = \frac{\text{Lf}(-L + M)\text{Rs} + \text{K1K5}\text{Rs}\text{Cos}[\text{K2} - \text{thetaR}]^2 - \text{K1}(L - M)(\text{K9}\text{Cos}[\text{K12} - \text{thetaR}] - \text{K5}\text{wr}\text{Cos}[\text{K2} - \text{thetaR}])\text{Cos}[\text{K4} - \text{thetaR}]}{(L - M)(\text{Lf}(L - M) - \text{K1K5}(\text{Cos}[\text{K2} - \text{thetaR}]^2 + \text{Cos}[\text{K4} - \text{thetaR}]^2))}$$

$$A[2,3] = \frac{\text{K1}\text{Cos}[\text{K4} - \text{thetaR}](3(L - M)(\text{Rf} + \text{Rssigma}) + 2\text{K5}\text{Rssigma}\text{Cos}[\text{K2} - \text{thetaR}]\text{Cos}[\text{thetaR}]) + 2\text{Rssigma}(\text{Lf}(-L + M) + \text{K1K5}\text{Cos}[\text{K2} - \text{thetaR}]^2)\text{Sin}[\text{thetaR}]}{3(L - M)(\text{Lf}(L - M) - \text{K1K5}(\text{Cos}[\text{K2} - \text{thetaR}]^2 + \text{Cos}[\text{K4} - \text{thetaR}]^2))}$$

$$A[3,1] = \frac{\text{K9}(-L + M)\text{Cos}[\text{K10} - \text{thetaR}] + \text{K5}\text{Rs}\text{Cos}[\text{K2} - \text{thetaR}] + \text{K5}(L - M)\text{wr}\text{Cos}[\text{K4} - \text{thetaR}]}{\text{Lf}(L - M) - \text{K1K5}(\text{Cos}[\text{K2} - \text{thetaR}]^2 + \text{Cos}[\text{K4} - \text{thetaR}]^2)}$$

$$A[3,2] = \frac{(L - M)(\text{K9}\text{Cos}[\text{K12} - \text{thetaR}] - \text{K5}\text{wr}\text{Cos}[\text{K2} - \text{thetaR}]) + \text{K5}\text{Rs}\text{Cos}[\text{K4} - \text{thetaR}]}{\text{Lf}(L - M) - \text{K1K5}(\text{Cos}[\text{K2} - \text{thetaR}]^2 + \text{Cos}[\text{K4} - \text{thetaR}]^2)}$$

$$A[3,3] = \frac{3(L - M)(\text{Rf} + \text{Rssigma}) + \text{K5}\text{Rssigma}(\text{Cos}[\text{K2}] + \text{Cos}[\text{K2} - 2\text{thetaR}] - 2\text{Cos}[\text{K4} - \text{thetaR}])\text{Sin}[\text{thetaR}]}{3(\text{K1K5} + \text{Lf}(-L + M) + \text{K1K5}\text{Cos}[\text{K2} - \text{K4}]\text{Cos}[\text{K2} + \text{K4} - 2\text{thetaR}])}$$

$$B[1,1] = \frac{Lf(-L + M) + K1K5Cos[K4 - \text{thetaR}]^2}{Lf(-L + M) + K1K5Cos[K4 - \text{thetaR}]^2(L - M) + K1K5(L - M)Cos[K2 - \text{thetaR}]^2}$$

$$B[1,2] = \frac{K1K5Cos[K2 - \text{thetaR}]Cos[K4 - \text{thetaR}]}{(L - M)(Lf(L - M) - K1K5(Cos[K2 - \text{thetaR}]^2 + Cos[K4 - \text{thetaR}]^2))}$$

$$B[1,3] = -\frac{K1PsiPMCos[K2 - \text{thetaR}](K5Cos[K4 - \text{thetaR}] + (-L + M)sigmaSin[\text{shift} + \text{thetaR}])}{(L - M)(Lf(L - M) - K1K5(Cos[K2 - \text{thetaR}]^2 + Cos[K4 - \text{thetaR}]^2))}$$

$$B[2,1] = \frac{K1K5Cos[K2 - \text{thetaR}]Cos[K4 - \text{thetaR}]}{(L - M)(Lf(L - M) - K1K5(Cos[K2 - \text{thetaR}]^2 + Cos[K4 - \text{thetaR}]^2))}$$

$$B[2,2] = \frac{Lf(-L + M) + K1K5Cos[K2 - \text{thetaR}]^2}{(L - M)(Lf(-L + M) + K1K5Cos[K2 - \text{thetaR}]^2) + K1K5(L - M)Cos[K4 - \text{thetaR}]^2}$$

$$B[2,3] = \frac{PsiPM(K1K5Cos[K2 - \text{thetaR}]^2 - (L - M)(Lf - K1sigmaCos[K4 - \text{thetaR}]Sin[\text{shift} + \text{thetaR}]))}{(L - M)(Lf(L - M) - K1K5(Cos[K2 - \text{thetaR}]^2 + Cos[K4 - \text{thetaR}]^2))}$$

$$B[3,1] = \frac{K5Cos[K2 - \text{thetaR}]}{Lf(-L + M) + K1K5(Cos[K2 - \text{thetaR}]^2 + Cos[K4 - \text{thetaR}]^2)}$$

$$B[3,2] = \frac{K5Cos[K4 - \text{thetaR}]}{Lf(-L + M) + K1K5(Cos[K2 - \text{thetaR}]^2 + Cos[K4 - \text{thetaR}]^2)}$$

$$B[3,3] = \frac{K5PsiPMCos[K4 - \text{thetaR}] + (-L + M)PsiPMsigmaSin[\text{shift} + \text{thetaR}]}{Lf(L - M) - K1K5(Cos[K2 - \text{thetaR}]^2 + Cos[K4 - \text{thetaR}]^2)}$$

